FUNCTIONALIZED ZIRCONIUM PHOSPHATE NANO PLATELETS - FROM SURFACE DESIGN TO DRUG DELIVERY

A Dissertation

by

ATASHI MUKHERJEE

Submitted to the Office of Graduate and Professional Studies of
Texas A&M University
in partial fulfillment of the requirements for the degree of

DOCTOR OF PHILOSOPHY

Chair of Committee, Abraham Clearfield
Committee Members, Robert Lucchese
Gyula Vigh
Robert Burghardt
Head of Department, David Russell

May 2014

Major Subject: Chemistry

ABSTRACT

The chemical characterization of nanomaterials in the realm of drug delivery and surface modification is on the current frontiers of analytical chemistry. A drug delivery vehicle must be able to carry therapeutic cargo and be able to reach the intended target or compartment. This dissertation will focus on the analytical characterization of zirconium phosphate (ZrP) in both alpha and theta phases as a drug delivery matrix utilizing multiple unique and novel analytical techniques.

In the first area we present for the first time, a methodology for the characterization of individual drug loaded 150 nm ZrP nanoparticles (NPs) by obtaining molecular information from single massive cluster impacts. The clusters used in this secondary ion mass spectrometry (SIMS) technique are Au_{400}^{4+} and $C_{60}^{+}/^{2+}$. The ionized ejecta from each impact are recorded individually which identifies ions emitted from a surface volume of ~10 nm in diameter and 5-10 nm in depth. The mode of analyzing ejecta individually from each single cluster impact gives insight into chemical homogeneity within nanodomains.

The *in vitro* biological release profile was investigated in simulated biological environment for the drug-ZrP nanocomposites. The release profiles reveal a direct dependency with the pH of the medium for the release of the complexes indicating targeting opportunities. Additionally the NP matrix breaks down in the artificial lysosomal fluid medium at pH – 4.5 indicating good bio-clearance possibilities, a major issue that plagues several alternative drug delivery carriers. This project is expected to

give rise to a facile drug delivery matrix that is highly biocompatible and leads to greater targeted gentoxicity for cancerous cells.

The second area of research presented in this dissertation investigates the surface modification of 150 nm α-ZrP NPs utilizing a host of different organo modifiers. α-ZrP was surface modified by reacting surface P-OH groups with 3-(triethoxysilyl)propyl isocyanate(TEPI), dichloromethyl(phenyl)silane(DCMPS) and lauryl methacrylate(LMA). SIMS in the event-by-event bombardment detection mode was utilized to calculate the degree of surface coverage for a brand new platform in conjunction with TGA, FTIR and XRPD to detail the surface confinement of the molecular assemblies. New discoveries continue to be made by creative scientists' everyday pushing what we know about inorganic layered materials and the analytical chemistry that drives this field.

DEDICATION

To

My Father & Mother,

My Brother,

The Mukherjee's & Bell's

My Mentors

And most of all

To Kenneth

There is no medicine like hope, no incentive so great, and no tonic so powerful as expectation of something better tomorrow.

Orison Swett Marden

ACKNOWLEDGEMENTS

I would like to take this opportunity to thank the many people who have been part of my support system during my years as a graduate student at Texas A&M University. First and foremost I want to thank Dr. Clearfield for being my mentor and my looking glass for what a real scientist should truly be. Curious, sincere, knowledgeable and always willing to provide inspiration and coaching. Thank you for the many anecdotes and interesting discussions. You have truly molded me into the scientist I am today. I would also like to thank my committee members, Dr. Lucchese, Dr. Vigh, and Dr. Burghardt for their guidance and support throughout the course of this research.

To Dr. Agustin Diaz, thank you for always being so enthusiastic about the chemistry that we do and the loud music on slow days. Your positivity always helped me see the brighter side of things. To Dr. Verkhoturov, thank you for your infinite wisdom and helping keep me afloat at a time when I was flailing. Your constant willingness to talk science or art or any other topic under the sun always kept graduate school interesting. The last few years wouldn't be the same without Rita, we may have moments when we doubt our abilities as scientists but know that in the end I have no doubt you will be both a successful scientist and entrepreneur. I wish you all the best in your future endeavors and in you I have found a true lifelong friend. To all the Clearfield group members past and present, thank you for being both friends and mentors during my graduate education.

To my family, the Mukherjee's and the Bell's thank you for all your advice and wisdom. I owe so much of who I am and who I will be to your love, support and encouragement. This thesis wouldn't be possible without you. To my dad who I affectionately call bubba, it would be impossible to thank you adequately for everything you've done. I couldn't have asked for a better role model. I know I can test your patience but thank you for always loving me unconditionally. You will forever be the yardstick I measure myself by. To mumma, you are the funniest and most positive person I know, don't ever loose that. You are the glue that holds us together and I only hope that I will be half the woman you are. Thank you for being my rock. To Raja, you are the smartest person I know. Thank you for always being a willing listener. You will always be my original "partner in crime".

And finally, to the love of my life, my husband, Kenneth. Thank you for being the umbrella that has gotten me through many a graduate school storms. Your constant encouragement, perspective and faith in me have helped give me the strength I've needed to accomplish this goal. I couldn't have done this without you – I love you.

TABLE OF CONTENTS

LIST OF FIGURES

FIGURE Page

FIGURE Page

FIGURE Page

FIGURE Page

LIST OF TABLES

CHAPTER I

INTRODUCTION

The word ‘nano’ is derived from the Greek word ‘nanos’ meaning ‘dwarf’. The prophetic talk entitled, “There’s plenty of room at the bottom”, by physicist Richard Feynman in 1959 marked the advent of nanotechnology. Over five decades later, nanotechnology has come a long way since its inception. One of those influential areas of nanotechnology is in the research and development of inorganic nanomaterials.[1] The versatility in applicability makes these materials highly attractive for a wide gamut of utilities.

Inorganic layered materials are one such area of innovative research. Their unique properties have given rise to a wide range of applications that has shown promise as high performance materials. From surface tethered molecular components that can serve a multitude of scopes, including coupling biomaterials,[2] to electron transfer reactions,[3-5] sensors and biochips,[6, 7] drug delivery,[8-11] photovoltaic,[12, 13] fuel cell,[14] and molecular electronics,[2, 12, 15] to controlling reactions at surfaces,[5] and tailoring surface properties. In addition, inorganic layered materials allow for greater exploitation potential through a wide range of intercalation chemistries. With modifications in synthetic parameters such as temperature, pressure, reaction time, concentration of reactants and the use of complexing agents it is possible to control particle size, morphology, crystallinity and aspect ratio.

This dissertation is centered on the synthetic modifications of a model system, zirconium phosphate (ZrP) of composition $Zr(O_2POH)_2.H_2O$, an inorganic layered nanomaterial and their subsequent use in developing new and unique analytical methodologies for nanodomain characterization. The ZrP material modifications proposed in the first half of this thesis are selectively sequestered onto the surface to establish a fundamental understanding of the surface chemistries. The lack of selectivity and sufficient delivery of the current anticancer agents in use is a major cause of severe side effects and treatment failures today. The second half of this thesis focuses on studies exploiting the intercalation chemistry of ZrP for the targeted delivery of anticancer drug therapeutics to cancerous cells and the controlled release of the drugs in-vitro. This assertion is illustrated by placing varied levels of anticancer drugs doxorubicin and cisplatin within the layers and using a host of analytical techniques to interrogate the resultant materials.

When it comes to the characterization of morphologies in the nanometric scale there is a general consensus that more needs to be done to improve their characterization.[16,17] During the course of this dissertation another focus will be using the novel analytical technique of secondary ion mass spectrometry (SIMS), a highly surface sensitive technique which provides a wide range of chemical and molecular information. Two main topics are investigated and discussed using this technique 1) characterizing the extent of surface modification onto the ZrP platforms with a variety of functionalities 2) investigating and discussing the application of cluster time of flight secondary ion mass spectrometry (ToF-SIMS) in the analysis of homogeneity

characterization for drug distribution within the ZrP matrix. The goals of both these studies were twofold: a) to devise new and unique methodology for inorganic layered material sample preparation for analysis in vacuum environments independent of modification, b) to interrogate and establish a protocol for quantifying the extent of surface coverage for the surface modified samples and the degree of material homogeneity for the intercalated samples. The analysis in both studies was performed in the negative ion mode using a custom built ToF-SIMS instrument which I will introduce in detail in the following chapter. Prior to the presentation of each individual study and sample preparation methodology it is useful to recall the scope of relevant advances in ZrP material design.

Zirconium Phosphates

Stemming from the need to exert higher control on surface and intercalation chemistries, zirconium phosphate (ZrP), $Zr(HPO_4)_2 . nH_2O$ a synthetic layered compound with a very well ordered structure was chosen to be the model material during the course of discussions in this thesis. It was first discovered in 1964 by Clearfield and Stynes via refluxing amorphous ZrP with phosphoric acid.[18] This layered material, ZrP is not unlike montmorillonite clays. With a high ion exchange capacity of 6.64 meq/g the material consists of Zr, P and O atoms. The structure consists of an octahedral sheet of Zr atoms linked by tetrahedrally oriented phosphate groups. Hydroxy groups orient into the interlayer planes. These –OH groups lend ZrP its, acidic character allowing for ease of ion exchange by a variety of cationic species. They have high thermal and chemical

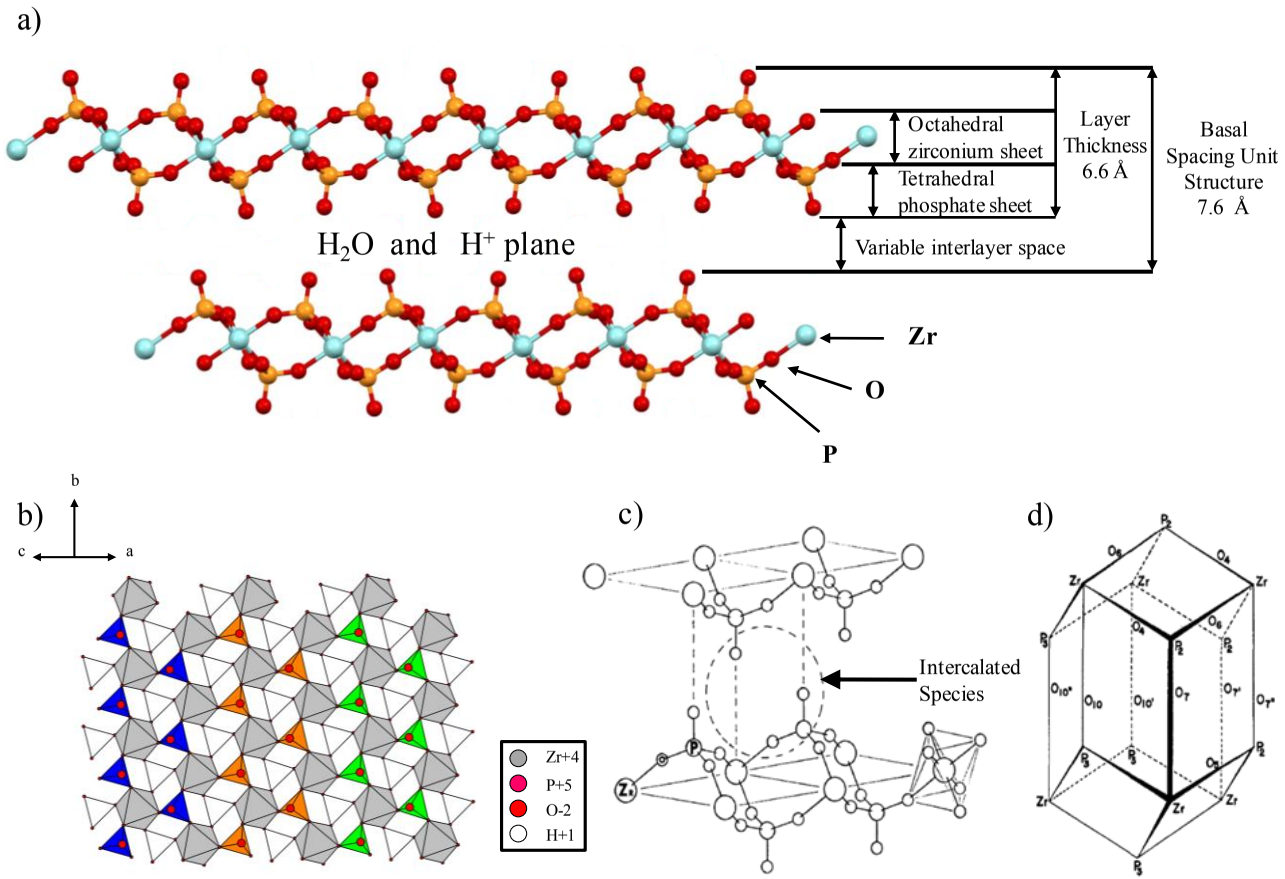

Figure I-1: Idealized structures of alpha zirconium phosphate: a) α-ZrP showing a dissection of the layer structure with dimensions and spatial arrangements of the layer assembly. b) Top view of the α-ZrP unit cell c) Zeolitic cavity into which intercalated species are sequestered. d) Dimensions of the zeolitic cavity.

stability, solid state ion conductivity, resistance to ionizing radiation, and the capacity to incorporate different types of molecules with different sizes between their layers.[8-11, 19-21] While there are several phases of ZrP the phases that my dissertation will concentrate on include the alpha phase ($Zr(HPO_4)_2 \cdot H_2O$) which has an interlayer space of about 7.6 Å and the hydrated theta phase ($Zr(HPO_4)_2 \cdot 6H_2O$) with an interlayer spacing of about 10.4Å.[22]

Figure (I-1a&b) shows the alpha phases of zirconium phosphate in its idealized structures. The crystal structure for the alpha phase was first elucidated by Clearfield and coworkers in 1968 utilizing the single crystal-methodology.[23, 24] In the alpha phase the material layer thickness is about 6.6Å with the remaining 1Å being occupied by the interstitial water molecule. [23, 24] The adjacent orthophosphate groups on the ab plane are 5.3Å apart allowing for two phosphate groups on the mentioned plane. [23] The associated area for each phosphate group is thus, $24Å^2$. The interstitial water molecule resides in the zeolite-like cavity forming a hydrogen bond with the P-O-H oxygen groups located perpendicularly (Figure I-1c). Van der Waals forces hold the layers together giving it its characteristic lamellar structure. [23]

The theta phase of zirconium phosphate is the hydrated phase with six moles of water in contrast to the one mole in the alpha phase. The crystal structure for this material still remains unresolved. First reported in 1969 by Alberti and Torracca[25] and separately by Clearfield et al.[26] The wide usage of the material didn't take off until 1982 when Kijima[22] first investigated the effects of temperature and Zr concentrations in solution to obtain pure θ-zirconium phosphate (θ-ZrP) at different levels of crystallinity.

Dilute solutions (0.05M) of $ZrOC1_2.8H_2O$ in 6M H_3P0_4 heated at 60-94°C for 48 h or longer yields only θ-ZrP, which reverts to α-ZrP on drying (Figure I-2).[27] Fujita and Hasegawa in 1985 were the first research group to report the pronounced ability of θ-ZrP to sequester large cations when they ion exchanged hexaaminecobalt (III) into the θ-ZrP. Since then, this unique increased layer spacing has allowed the theta phase the ability to entrap several relatively large cations compared to its alpha counter-part.[8-10, 20, 28, 29] In addition, the chemical structure and hexagonal nano-platelet like shape of each ZrP layer remains relatively unchanged from the original alpha phase.

In the quest for new and improved synthetic techniques to allow for greater control in particle size, morphology and crystallinity significant strides have been made since the inception of the ZrP materials. In 2007, Sun and coworkers produced a host of different α-ZrPs with a wide variation in aspect ratios by controlling the concentration of reactants, temperature, pressure and the use of complexing agents.[30] The resultant materials ranged from nano to micro dimension sizes and varied crystallinity. Figure I-3 shows SEM images of six of those materials synthesized displaying an assortment of particle sizes. More recently, Pica and coworkers report a new synthetic route for ZrP synthesis using aliphatic alcohols to produce even smaller particle sizes than previously known.[31] The planar sizes varied from 90-200 nm and thickness from 20 to 85nm depending on the solvent.[31] Figure I-3 shows the TEM images for these new compounds. In this next section I will discuss some of the different mechanisms that are generally employed in the intercalation and subsequent encapsulation of a variety of species within the ZrP layers will be discussed.

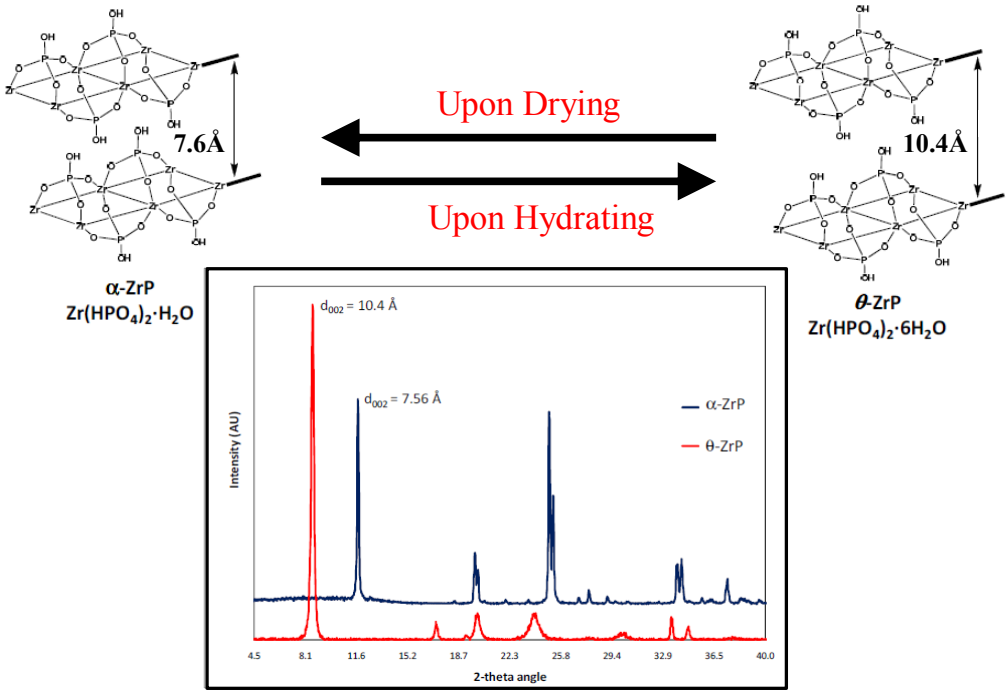

Figure I-2: Top: Idealized structure of α-ZrP and θ-ZrP. Bottom: XRPD pattern of θ-ZrP(red) and α-ZrP(blue). Modified from references (9 and 25)

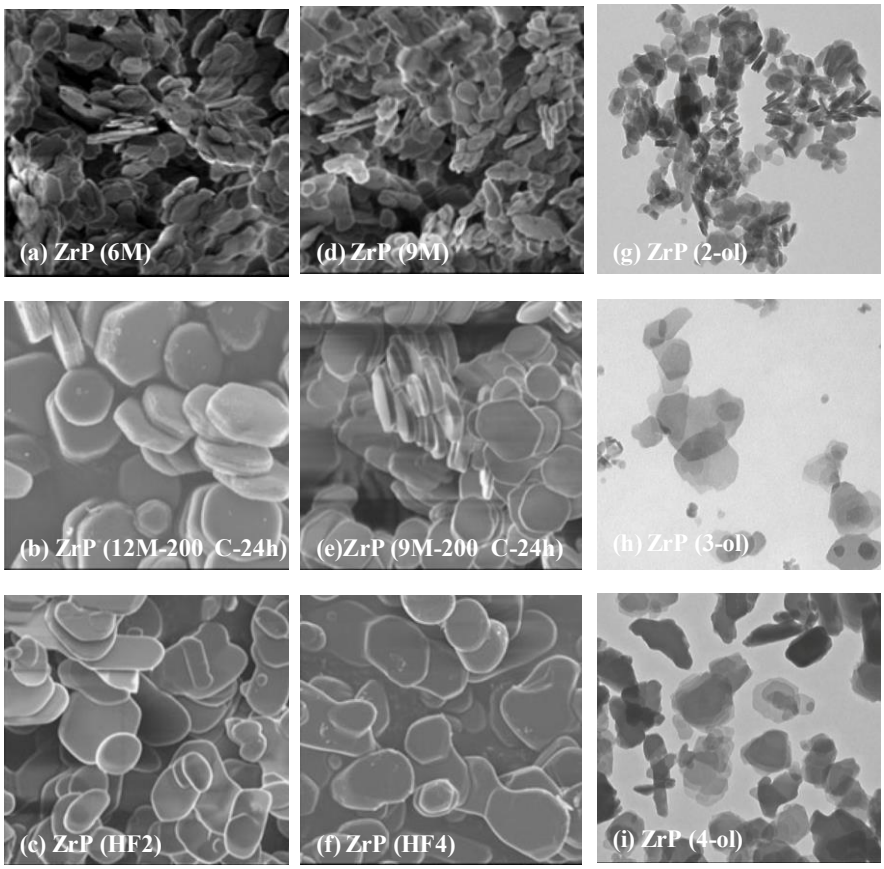

Figure I-3. SEM (a-f) and TEM (g-i) images of α-zirconium phosphate nanoplatelets synthesized under different conditions producing a wide range of particles varying in size and crystallinity. (Adapted from references 29 & 30)

Zirconium Phosphate Intercalation Chemistry

According to the Merriam Webster dictionary, intercalation is simply the act of inserting between or among existing elements or layers. Layered materials by virtue of their inherent physiology possess the ability to entrap a variety of species. The process by which a guest molecule or ion maybe sequestered within a host matrix is intercalation. The structure of the guest-host or intercalation compound is only slightly perturbed from its original host structure and in most cases, this reaction is reversible.[32] The relationships responsible for the sequestration of the guest molecule are varied and the levels of loading are determined by a variety of interactions. In the case of zirconium phosphate chemistry, intercalation occurs through three predominant mechanisms: ion-exchange, acid-base reaction or through charge-transfer (Figure I-4).[33] These reactions are known to be topotactic, i.e. they displace pre-existing layers to make room for new species.[34] Therefore, the first diffraction peak at the lowest 2θ angle in the X-ray powder diffractograms corresponds to the interlayer distance.[35] By monitoring newly formed phases using the Rietveld refinement method and XRPD pattern it is possible to gauge intercalations. This was confirmed by Clearfield and coworkers via the elucidation of the crystal structure of the two phases of pre and post intercalated α-ZrP with guest molecules.[36, 37] Each of these mechanisms may work independently or in combination to allow for guest molecule encapsulation.

Ion Exchange

In the case of the ion exchange reactions, the protons present in the inner lattice attributed to the phosphate groups are easily exchanged to incorporate the charged guest species. The direct ion exchange of small ions (diameter < 2.61 Å) such as Na^+ is a very well established ZrP intercalation reaction, involving the direct suspension of the material in a solution containing sodium chloride and sodium hydroxide.[38] In addition, several cations such as Li^+, Ag^+, Tl^+, Cu^+, Ca^{2+} among many others can easily be sequestered in the interlayer phosphate.[39] These newly formed intercalated materials show the appearance of a newly formed phase in each case which is directly related to the size of each individual species and the electrostatic forces between the guest ion ad interlamellar regions.[39] While direct ion-exchange works relatively well for the smaller cations, in the case of the larger cations such as Rb^+, Cs^+, Ba^{2+} and NH_4^+ diffusion into α-ZrP is poor.[33] Research indicates cations larger than 2.63 Å in diameter don't tend to directly ion exchange into α-ZrP.[38] In 2002, Colón and coworkers reported the direct ion exchange of luminescent metal complexes such as tris(2,2′-bipyridine)ruthenium(II), $Ru(bpy)_3^{2+}$ using θ-ZrP.[40] The high ion exchange capacity of ZrP makes it an exceptional candidate for a variety of material encapsulation type reactions.

Acid-Base

The acidity of the inner lattice of ZrP allows for easy acid-base intercalations. An acid−base reaction occurs, when a proton is transferred from the −POH group to the basic species by deprotonation. The intercalation is driven by the presence of this

medium strong P-OH Bronsted acid group in the inner layer. The incoming guest species would act as a base reacting with the inner lattice phosphate groups permeating the inner galleries resulting in a positively charged guest species being neutralized by the deprotonated phosphate groups. Compounds with proton accepting functionalities such as amines are a very good example for the acid-base driven intercalation reactions.[41] Several ammonium salts and alkylamines have been successfully incorporated into the ZrP layers utilizing this mechanism.[42] Clearfield and coworkers estimated the potential molecular arrangement of n-butylamine intercalated into ZrP by accounting for the guest molecule elemental composition and potential change in interlayer distance attributed to the guest molecule's dimensions.[43] The appearance of a new phase at 18.6 Å helped identify the n-butylamine addition within the ZrP layers via the acid-base reaction mechanism.[43] Additionally by changing the concentration of the guest molecule, n-butylamine additional new phases were identified.[43]

Redox

Oxidation-reduction reactions, although a bit uncommon, have also been known to drive intercalation reactions for guest molecules. The oxidizing effect of the acidic inter layers may cause the oxidation of the intercalating guest species in the process driving the redox reaction. In 1980 Johnson reports the intercalation of organometallic guest species, such as cobaltocene.[44] The cobaltocene is intercalated into γ-ZrP as cobaltocenium cation.[44] θ-ZrP has been employed to intercalate ferrocene to produce a ferrocenium ion loaded material.[45] Any of these individual mechanisms or any

combination of them can be used to expand the possibilities of encapsulated species for a large variety of applications.

The intercalation of large species into α-ZrP isn't very favorable due to the intercalation energy barrier posed by larger guest species. In order to overcome challenges posed and allow for facile access of the inner layers the γ-ZrP and θ-ZrP with their enhanced layer spacings are used to incorporate larger molecules. Additionally the use of preswelling agents such as sodium ion exchanged ZrP also allows to expand inner layers can also be used to overcome the intercalation energy barrier.[39] Therefore it is possible to exploit additional chemistries to open up additional possibilities in the realm of intercalation.

Drug Delivery Rationale

In our daily lives, the word 'deliver' has several meanings. Arguably, it is most commonly used in the sense 'to send to an intended target or destination'. Nanomedicine is a fast evolving field involving the use of nanostructures for medical applications. The need to maximize therapeutic activity while minimizing negative side effects is driving current drug delivery attempts. With nanomedicine for the first time we have the possibility of designing specialized systems to meet specific requirements of targeted cargo delivery, higher drug bioavailability and most importantly reduced genotoxicity. In this fast evolving field inorganic layered nanomaterials (ILN) have received a great deal of attention of late.

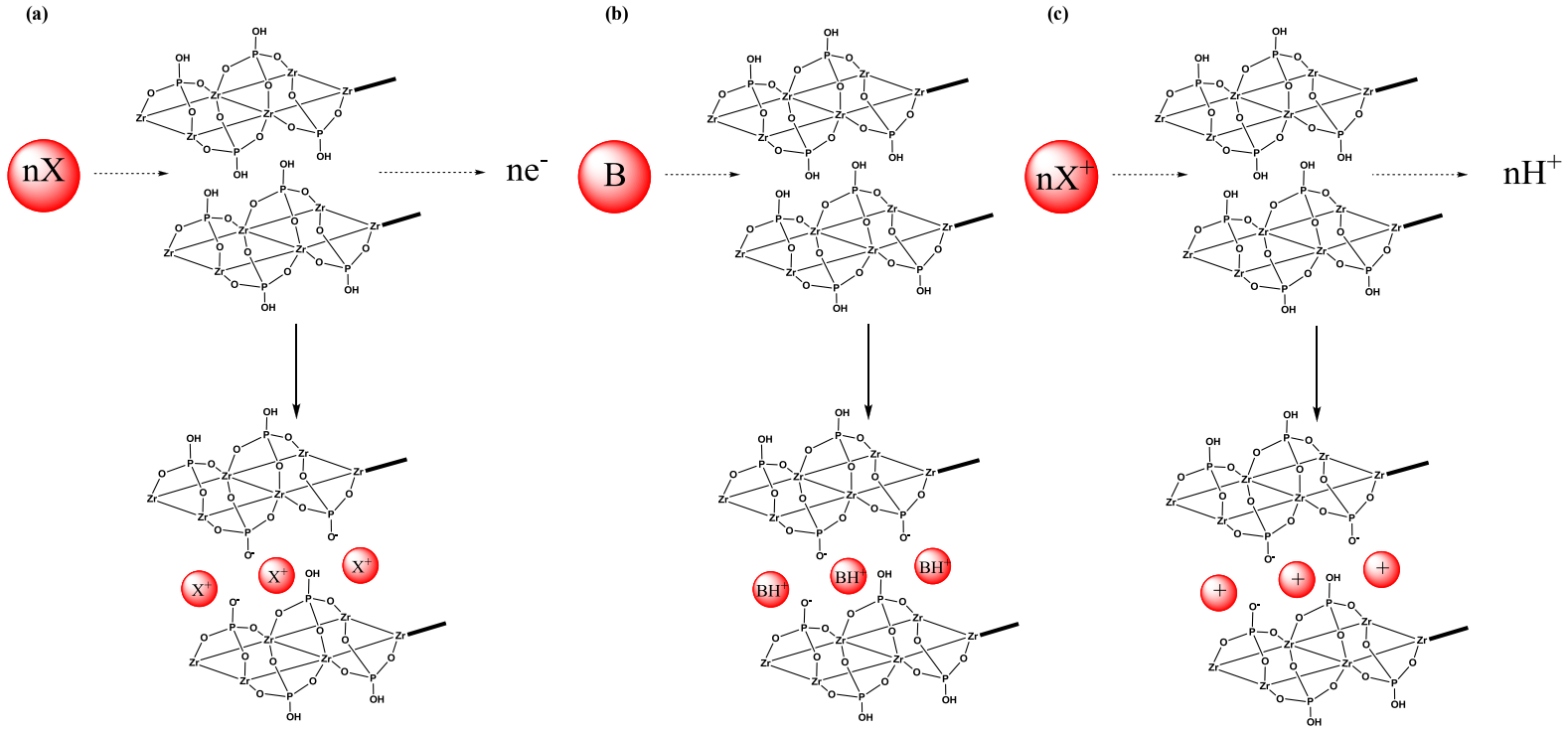

Figure I-4: Proposed mechanism of intercalation (a) Ion – exchange (b) Acid-base (c) Redox

In 1997 Danjo and coworkers reported the intercalation of anticancer agent cytarabine into γ-titanium phosphate.[46] Layered double hydroxides another class of ILN consisting of cationic brucite-like layers with anion exchangeable inner lamella that have been used to encapsulate a variety of drugs such as fenbufen,[47] naproxen,[48] salicylate[48] along with a large host of other non-steroidal anti-inflammatory drugs (NSAIDs) pain relievers.[49] In addition, Choy and coworkers have reported biomolecular–inorganic hybrids using cationic LDHs to encapsulate anionic biomolecules (such as DNA fragments, ATP, or an antisense oligonucleotide).[50] Thus, the central idea behind the use of laminar nanostructures is to allow for a variety of drugs and biomolecules to be easily encapsulated within the interlayer galleries while being protected. The size tunability of these materials makes them particularly attractive vehicles since the ideal size required for incorporation of nanodevices is predominantly in the 100-300nm range. This allow for delivery in tissues that have a fenestrated vasculature and a reduced lymphatic drainage as is the case with typical neoplastic tissues.[51] Additionally the flexibility in surface modifying these materials with a host of different surfactants also allows for greater targeting specificity.

The rationale behind the design of nanocarriers for cancer therapy was eloquently described by Peer and coworkers. They outline, nanocarriers offer several advantages over free drugs: (1) they protect the drug from premature degradation; (2) prevent extraneous interactions; (3) increase effective dosage through enhanced absorption by target tissues through effective distribution (4) control pharmacokinetic and drug tissue distribution profile; (5) improve intracellular penetration.[52] Some of the essential

characteristics that make up an effective nanocarrier include: (1) being made from biocompatible materials, well characterized, and easily functionalized; (2) exhibiting high uptake efficiency at target cells over normal (healthy) tissue; (3) be soluble or colloidal under aqueous conditions for increased effectiveness; (4) have an enhanced permeability and retention along with an extended circulating half-life, a low rate of aggregation and a long shelf life.[52, 53]

Zirconium Phosphate in Drug Delivery

ZrP has been used in biological applications, ranging from its use as a dialyzer[54] to its applications in drug delivery.[8-11] In humans, Zr is not considered an industrial health hazard.[55] Zr based compounds have been used in dental implants and other restorative practices,[56-59] total knee[60] and hip replacements,[61, 62] and ossicular chain reconstructions.[63] Zr-containing sorbents such as ZrP have been used extensively and for several years successfully and without complications in hemofiltration,[64-66] hemodialysis,[67] peritoneal dialysis,[68] and in the design and construction of artificial kidneys.[69-71] Additionally, other Zr based compounds have been used extensively in deodorants and antiperspirants for decades. Experimental and clinical studies support the general consensus that Zr compounds are biocompatible and exhibit low toxicity. Reports of Zr toxicity in medical literature are few and far between, despite the increasing use of Zr based compounds in biological applications.[72] All the evidence from the medical and chemical community seems to suggest that ZrP materials have all the ideal characteristics to be successfully used as a carrier in a biological system. The

high ion-exchange capacity and known activity towards bioactive materials make it an attractive target for biological applications, especially in the realm of drug delivery. Among the wide variety of species that could possibly be intercalated into the variety of ZrP phases are drugs, dyes, MRI contrasts agents, proteins, enzymes, genes, etc. Reports of Zr toxicity in medical literature are few and far between, despite the increasing use of Zr based compounds in biological applications.[72] All the evidence from the medical and chemical community seems to suggest that ZrP materials have all the ideal characteristics to be successfully used as a carrier in a biological system. The high ion-exchange capacity and known activity towards bioactive materials make it an attractive target for biological applications, especially in the realm of drug delivery. Among the wide variety of species that could possibly be intercalated into the variety of ZrP phases are drugs, dyes, MRI contrasts agents, proteins, enzymes, genes, etc.

Improving Drug Efficacy through Delivery

Improving drug efficacy in hard to fight malignancies can help turn the tide in treatment effects. While new drug discovery is essential, improving the delivery efficacy of existing therapies can only help the bottom line. By changing the loading levels (LDL) of the bioactive species within the layers of inorganic layered materials, such as ZrP it is possible to control their concentration allowing for a greater control in potential pharmacological release. Additionally by synthesizing the ZrP, based on custom size needs the LDLs can be further influenced.

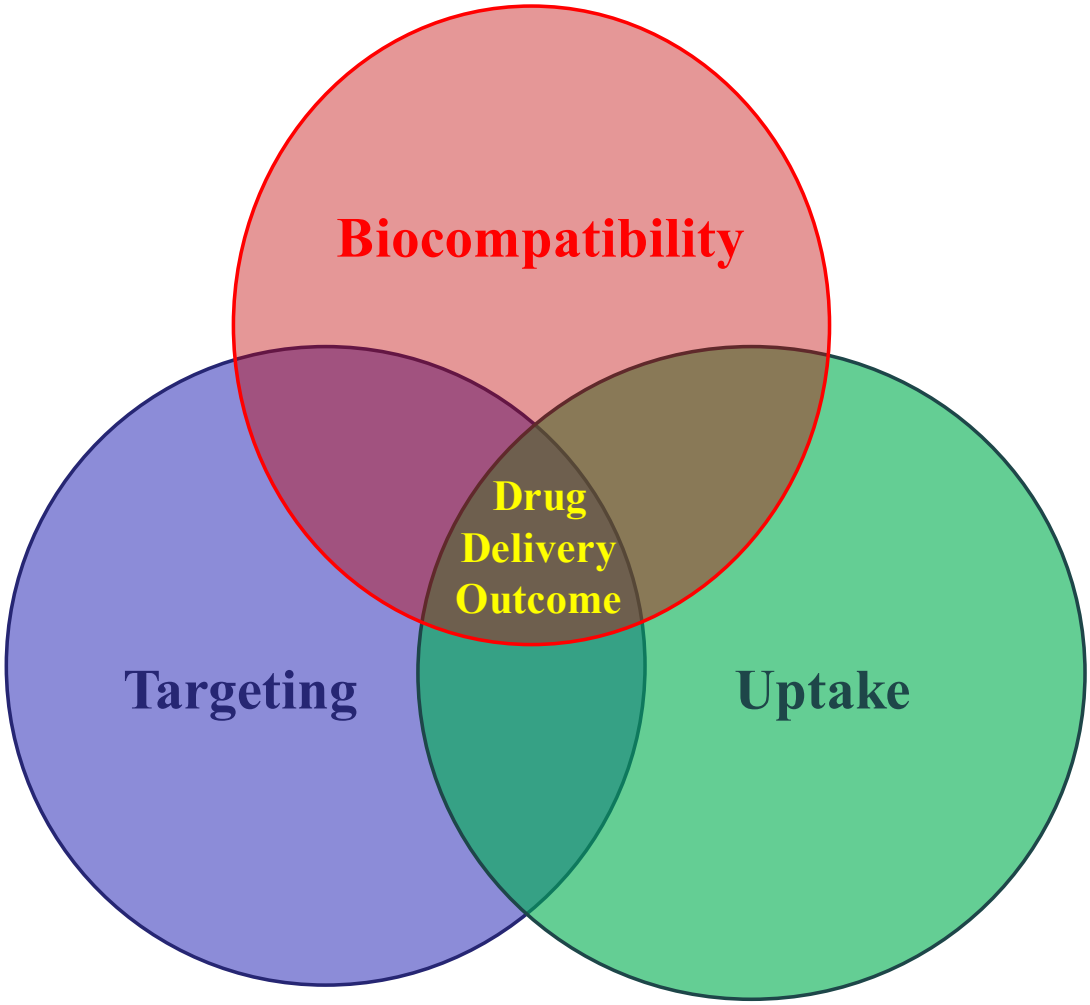

Figure I-5: Cartoon representation of the three most basic and important characteristics involved in the successful design of a drug delivery system that influences potential outcomes.

Characteristically the release profile for most inorganic layered materials depends on or may be negotiated via a chemical switch, concentration gradient, pH change and/or biological stimuli.[73] By employing surface functionalization and grafting biologically relevant targeting moieties onto the surface of the ZrP platelets it is possible to further enable effective targeting and increased biocompatibility and cellular retention, all crucial factors in successful drug delivery agents (Figure I-5). The unique platelet-like shape, presented by the ZrP particles, provides additional surface area of interaction compared to their spherical counterparts. In comparison with polymer drug delivery agents, ILN like ZrP allow for much more effective characterization by exploiting their well-studied crystal structure. By employing standard analytical techniques it is possible to gauge the bioactive species LDL with relative ease. Moreover, ZrP is pH sensitive making it an ideal candidate for drug delivery via oral uptake and tumor site release, since the material is relatively robust. Ferrari and coworkers, discuss in length the downfalls of spherical drug delivery agents. They allege that spherical particles exhibit the poorest margination properties, penetration through vascular fenestration (a crucial factor in uptake through tumor sites) and adherence to the endothelial walls - hampering effective cellular uptake. [74-77]

Challenges in Drug Delivery

With a clearer idea of what makes a superlative drug delivery vehicle it becomes even more crucial to know what factors directly hamper its transport. Figure I-6 highlights several of the obstacles that a nanoparticle drug delivery system needs to

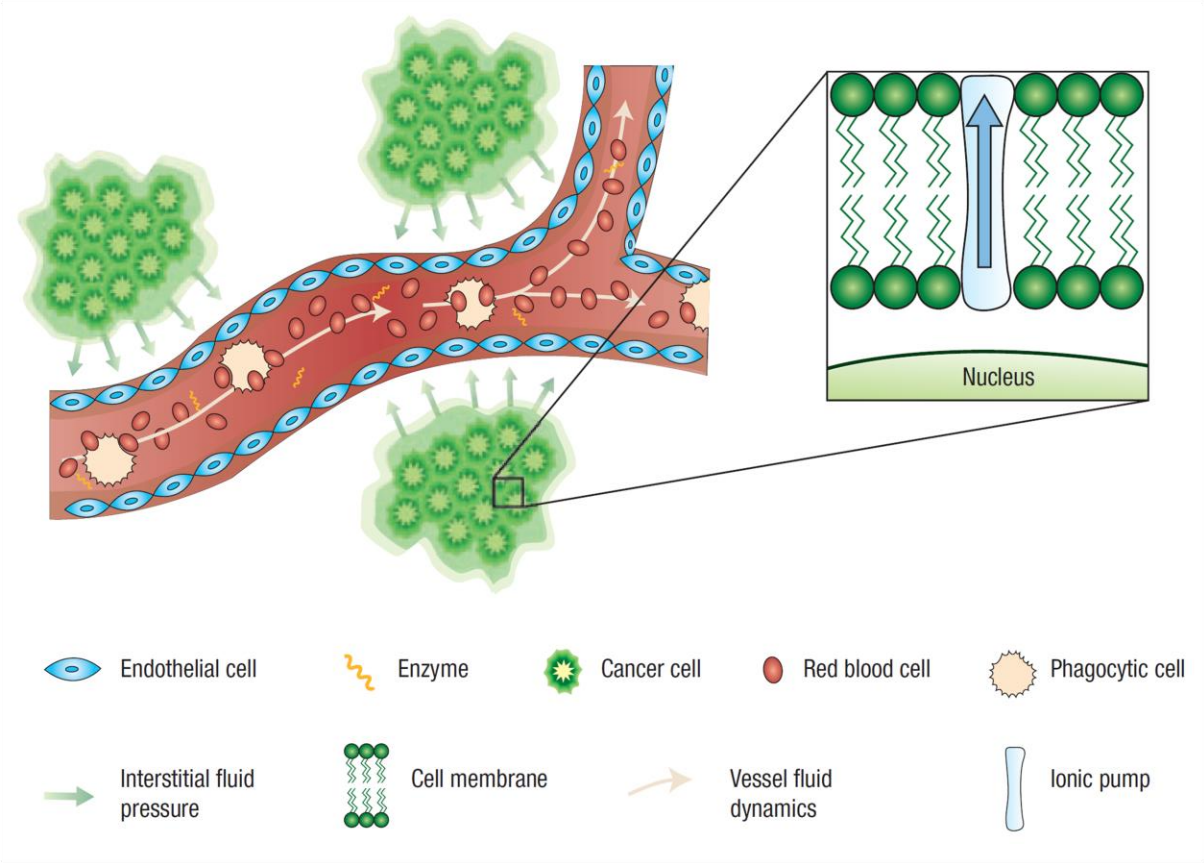

Figure I-6: Animated representation of the several biological barriers faced by a nanocarrier drug delivery system. (Reference 77)

overcome in order to reach its intended target. These biological barriers largely prevent any injected nanocarriers from actively interacting with their destination. These barriers include but aren't limited to: (a) the reticulo-endothelial system, (b)endothelial/epithelial membranes, (c) complex networks of blood vessels (d) abnormal flow of blood and (e) interstitial pressure gradients.[77]

In order to overcome several of these challenges overtime it has become crucial to invent new and innovative design ideas to exploit pre-existing tumor physiology and motivate innovative drug delivery design. The pre –existing vascularization of tumor cells allows for greater nanoparticle penetration (Figure I-7). Nanoparticles designed to be large enough to access these cancerous tissues but small enough to avoid incorporation into healthy tissues exploit one such aspect of tumor physiology. Additionally, once a nanoparticle has successfully reached a tumor site, another interesting stimulus that a tumor site affords is a lower more acidic pH microenvironment compared to normal tissues. This is attributed to major mechanisms including the production of lactic acid and hydrolysis of ATP in hypoxic regions.[78] It has also been hypothesized that the pH of solid tumors is acidic due to increased fermentative metabolism and poor perfusion.[79] While the absorption of calcium, magnesium, sodium and oxygen is hampered, making a tumor microenvironment anaerobic; glucose transport remains unaffected. This kind of activity leads to fermentation, causing a lactic acid buildup, leading to a low pH environment. Inefficient energy production and usage propels tumor tissues into the starvation mode causing incoherent cellular assembly. This allows tumor cells to uptake larger particles than

healthy normal cells under usual conditions due to the enhanced permeability of the cancerous cells. Additionally, the epithelial walls around cancerous tissue sites are highly capillarized and vascularized allowing for much greater permeability. Hyper-permeable tumor vasculature allows preferential extravasation of the circulating drug carriers due to enhanced permeability and retention (EPR) effect.[80] If the drug delivery vehicle cannot deliver its cargo to the interior of the cell where it can be active, the benefits of using a drug delivery vehicle are greatly diminished. Developing a drug delivery vehicle that is simultaneously able to maintain a long circulation half-life while also being able to deliver its cargo to the interior of the cell remains a key challenge in systemic delivery.

Another very important feature of an effective drug delivery agent is the release profile exhibited by the subjective delivery agent in different biological media. Different drugs have different concentration dependent therapeutic windows. When the drug loading concentration falls below its critical level of effectiveness, the drug stops being efficient. Conversely, if too much of the drug is loaded into the NP delivery system then it will start exhibiting all the treatment effects of the pristine drug, as is the case in many chemotherapeutics.

Designing a drug delivery system that can release its cargo in a controlled release fashion over a period of time can serve as an internal safe house. This helps maintain active drug concentration in the blood stream during the required therapeutic window of effectiveness preventing unwanted side effects. The drug release profile remains one of the key parameters tuned by researchers in order to maximize the benefits of using a

drug delivery vehicle. Layered materials such as ZrP allow for step-wise drug release and that is one of the characteristics of ZrP that will be uncovered and discussed in the course of this dissertation. This dissertation will also discuss several of these outlined key challenges when pursuing ZrP in drug delivery strategies.

Characterization of Nanoparticles

In addition to the challenges posed in designing a drug delivery carrier additional challenges arise on the analytical front. Despite the use of nanoparticles in a wide range of applications, only a limited number of analytical techniques exist for their characterization. In order to design effective carriers for delivery and/or for surface functionalization a real need exists for effective and efficient characterization to verify material quality from one synthetic batch to the next. As the field of nanotechnology grows, it becomes increasingly important not only to explicitly identify the chemical composition of NPs themselves, but also of the functionalization or surface modification of the NPs.[81] A comparison of the spatial resolutions and sensitivities for several analytical techniques currently used in nanoparticle characterization is shown in Figure I-8and a comparison of their analytical depths is shown in Figure I-9.[82]
Techniques such as transmission emission microscopy (TEM) and scanning electron microscopy (SEM) are sensitive to surface morphology of NPs. However, due to the high fluence of electrons in both techniques; their applicability in imaging biomolecules is relatively limited.[83] This leads to the need for dyes and fluorescent biomarkers in order to tag and follow relevant molecules of interest. These often involve complicated sample

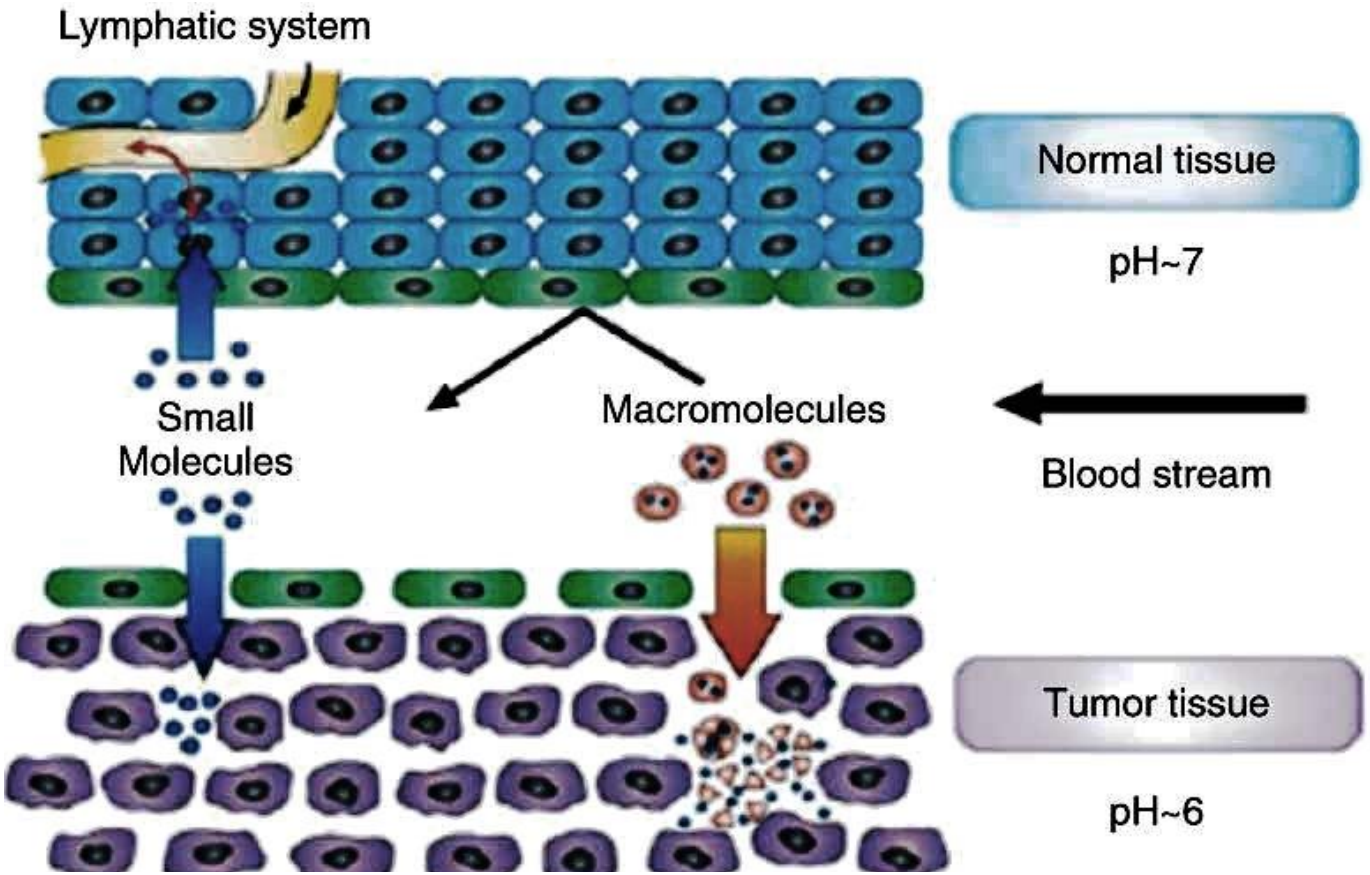

Figure I-7: Schematic representation of anatomical differences between normal and tumor tissues. Tumor cells exhibit lower pH, enhances vascularization, and cellular aggregation. Permeable vasculature presents enhanced permeability and retention (EPR) effect. (Reference 80)

preparation and pretreatment. Additionally complications also often rise from overlap of different labels reducing specificity and accuracy of measurement. In order to circumvent challenges posed by enhanced electron fluence, low acceleration beam energies (< 2 Kev) are often used. This however diminishes image resolution and quality. SEM resolution limits its use for the characterization of nanoparticles with sizes smaller than 5 nm for a cellular environment.

Optical imaging (OI) can be used to image NPs > 20 nm in the phase contrast mode or differential interference contrast mode; fluorescence microscopy can detect particles at the singular entity level;[84] Several of the techniques listed in Figure I-8 offer isotopic information but no molecular information. Other techniques provide chemical information like in the case of derivatized AFM tips, infrared (IR) and Raman spectroscopy and are nondestructive. XPS has been utilized to characterize surface coverage of DNA/alkylthiol monolayers by the Castner group.[85, 86] It is known to provide information of the outermost ~10 nm of surface modified material. The use of an x-ray probe limits XPS imaging to a submicron-scale lateral resolution due to challenges arising from focusing.

Mass spectrometry is well suited for the analysis of NPs to yield chemically relevant information. The use of mass spectrometry in nanotechnology studies have focused on mass determinations of various sizes and types of NPs.[87-89] In the realm of drug delivery the fabrication of controlled-release systems can be technically difficult compared with conventional dosage forms, evaluation and analysis of the final product is vital. Dissolution studies have been used in the past to observe drug release; however

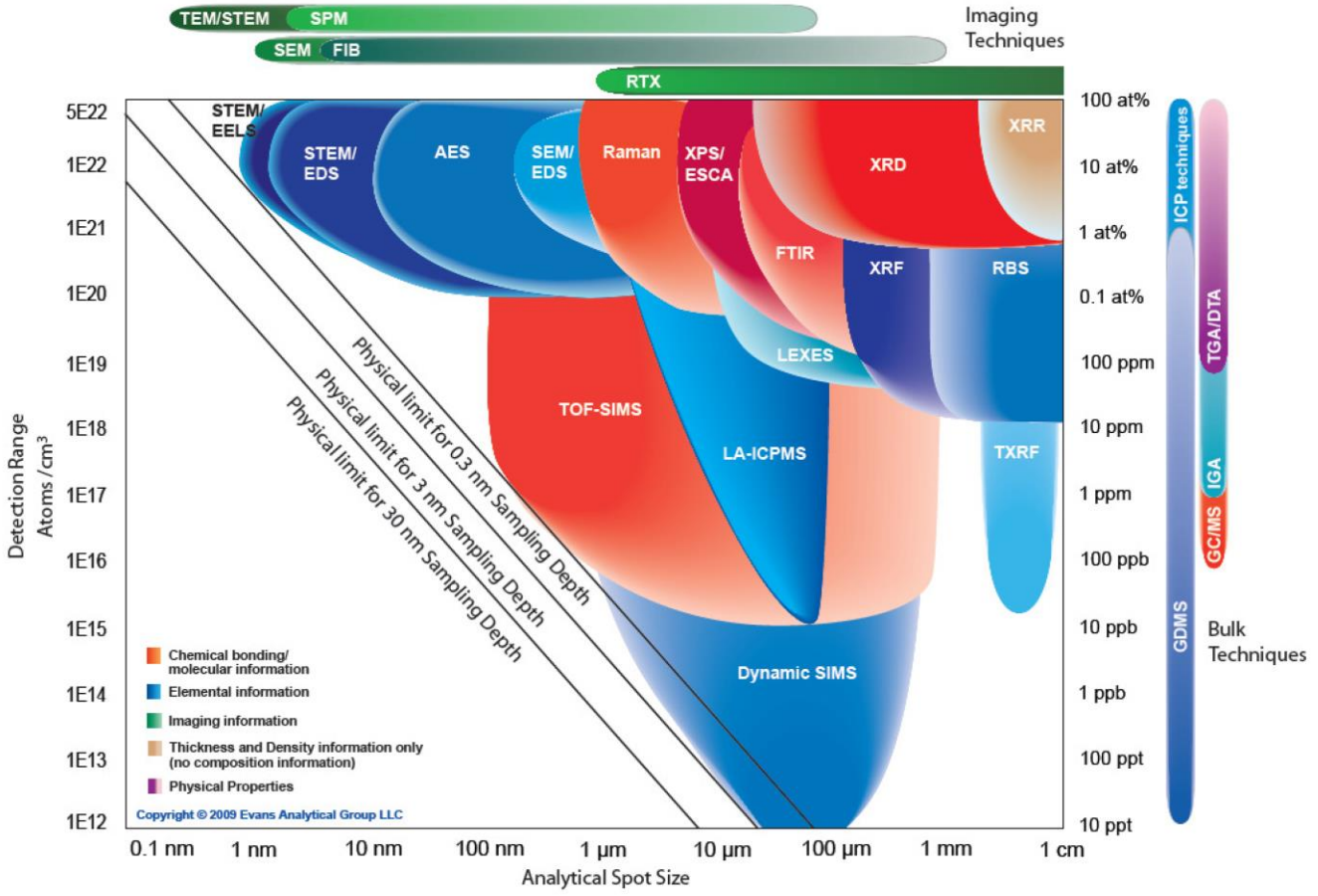

Figure I-8: Comparison of spatial resolutions and sensitivities for various analytical techniques (From reference 82)

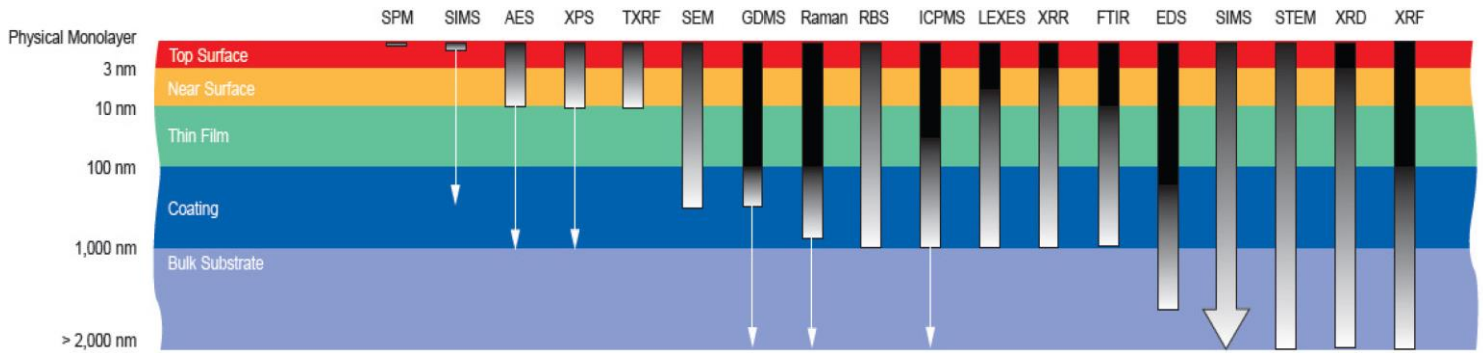

Figure I-9: Schematic profile of comparison of sampling depths of various analytical techniques (Reference 82)

any unwanted effects cannot be readily attributed to specific defects within the carrier structure and/or composition. To overcome this, mass spectrometry based techniques are used to probe cross sections of the drug-matrix composite. Mass spectrometry, specifically time of flight secondary ion mass spectrometry (ToF-SIMS) has been used extensively to characterize polymeric drug delivery systems.[90-97] TOF-SIMS has also been used extensively in the study of inorganic materials.[98-101] However, using the technique for the characterization of inorganic layered nanomaterials in drug delivery remains a relatively scarce area of analytical research as far as we are aware. In the subsequent dissertation chapters the efficacy of the technique in drug delivery analysis of ILNs will become apparent.

Secondary Ion Mass Spectrometry (SIMS)

Secondary Ion Mass Spectrometry (SIMS) is a mass spectral technique that is capable of obtaining molecular chemical information from NPs. It is a surface analysis technique where primary ions which can be atomic or polyatomic are used to sputter positively and negatively charged secondary ions. It involves the use of energetic projectiles (primary ions) to bombard analyte surfaces, which induce the sputtering of secondary species (electrons, photons, atomic and polyatomic ions, and neutrals). A general schematic for the SIMS experiment is presented in Figure I-10. The technique provides molecular, chemical and isotopic information. It can also be used in depth profiling analytes. In its early years SIMS was and to a large extent still is used heavily by the semiconductor industry.[100] Traditionally, atomic projectiles such as Ar^+, Ga^+,

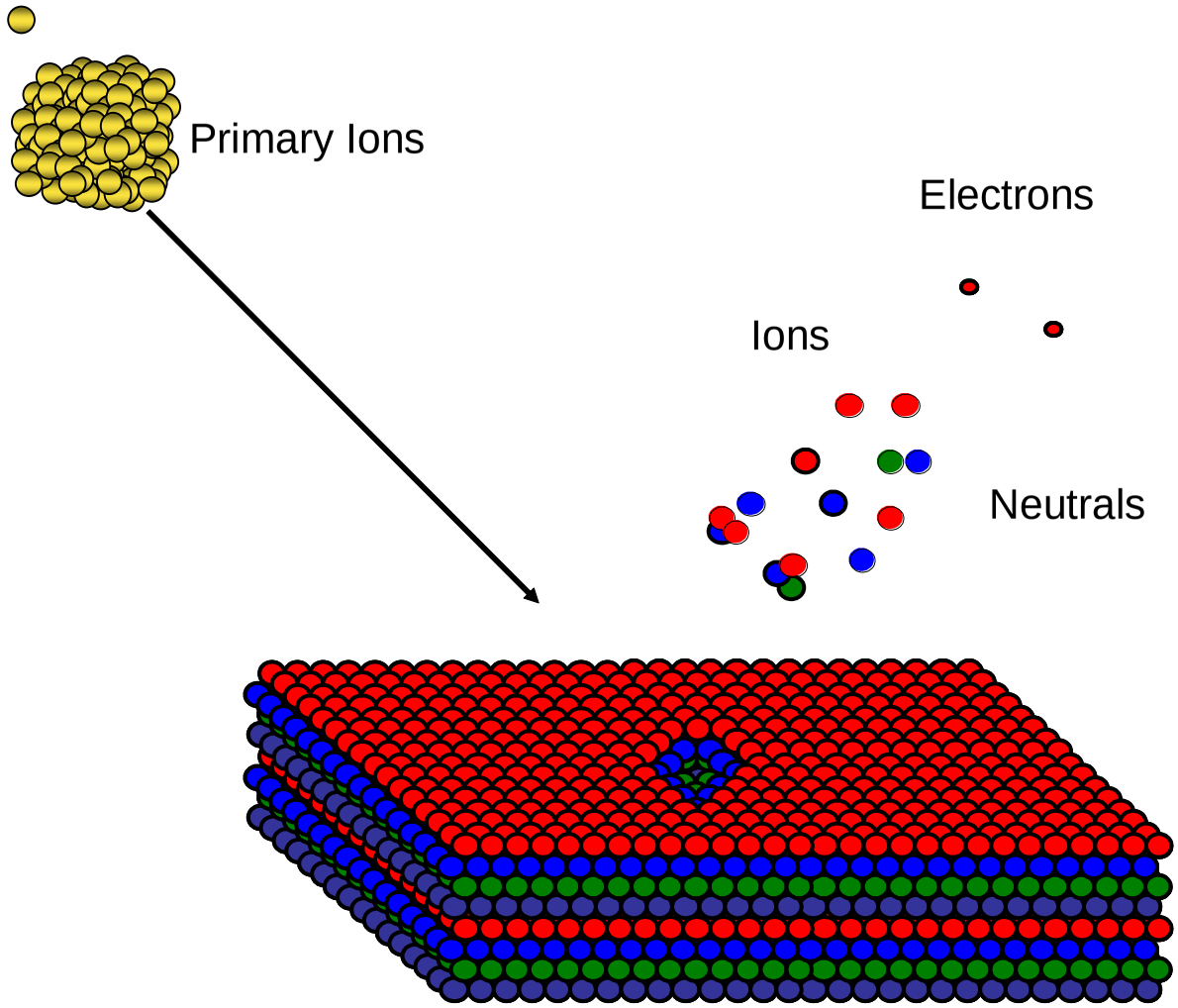

Figure I-10: General schematic of secondary ion mass spectrometry process. The primary ion maybe atomic, polyatomic or a cluster

C_{60}^{+}, or alkali metal are used as primary projectiles. SIMS does not require a matrix, fluorescent, or isotopic labeling, which eliminates sample preparation and allows direct characterization of native sample species (organic &inorganic) to be performed. With the discovery of cluster projectiles the realm of SIMS analysis has extended into applications in molecular and biological imaging. In the following sections, the principles of secondary ion mass spectrometry as it relates to this thesis will be presented.

Dynamic vs. Static Regime

Secondary ion mass spectrometry can be divided into two broad strata based on the dosage of primary ions delivery to the sample target of interest. At high doses ~10^{12} ions/cm^2 the mode of operation is considered to be "dynamic" SIMS. In this mode both elemental as well as isotopic information can be extracted from the samples of interest. The detection sensitivity of the technique is in the ppm - ppb range for all elements. In dynamic SIMS a primary ion beam is used to raster material from a small target to obtain layer-by-layer information in a well-defined sample area. This technique is generally considered destructive since secondary ions produces undergo extensive fragmentation, which limits most studies to elemental and isotopic distribution analyses. That being said, it is possible to obtain three-dimensional chemical information (depth profiles) of the targets of interest.[102]

When the primary ion fluence is at a rate of less than 10^{12} ions/cm^2 the mode of operation is considered to be "static" SIMS. By reducing the fluence, the technique

interrogates only the top most atomic or molecular layers of a target material of interest to reveal both elemental and chemical composition. The energy from the primary ions is dissipated near the surface region of a solid allowing for a minimally destructive process (<1% surface damage) with minimized beam mixing and beam damage issues. Furthermore, using static SIMS it is possible to relate information in nanovolumes by looking at the area perturbed.[103] When the fluence of primary projectiles is statistically below ~1000 ions/s each projectile impact is isolated in time and space. This is better known as the "super static regime" and allows for stochastic analysis. Stochastic sampling allows for better consistency and quality of secondary ion information collected. The secondary ions from each individual impact event are collected and stored before the subsequent projectile perturbs the target. This methodology is termed as the event-by-event bombardment detection mode. The "event-by-event bombardment/detection mode" probes nano-objects one at-a time, while collecting and storing the corresponding secondary ion information.[104] Having a lower fluence with a relatively small primary ion greatly limits the amount of information revealed due to the relative inefficiency of the projectile in the production of secondary ion signal. The challenge was to increase the emissions of intact molecular ions. This however changed with the use of cluster (polyatomic) projectiles.

Cluster SIMS

In 1960 Rol et. al. and Gronlung et al. observed that impacting metallic surfaces with a small cluster such as KI^+ lead to larger secondary ion sputter yields compared to

individual ion beams of K^+ and I^- alone.[105, 106] By using SF_6 polyatomic cluster ion an ion yield enhancement of ~10-25 folds was observed by Appelhans et al. in 1989 in comparison to the yields reported by using Cs^+ ions despite their similar atomic masses. [107] The main observations from cluster SIMS include a) nonlinear increase in secondary-ion yields with complex cluster projectiles; and b) increase of secondary ion yields proportional to the square of the projectile velocity for atomic species.[108]

In 1996 E.A. Schweikert et al. reported that 20 keV C_{60}^+ cluster projectiles produce a ~17 fold enhancement for phenylalanine molecular yield compared to Cs^+ and Ga^+ projectiles at the same impact energy.[109] Vickerman et al. developed a 10-15keV $C_{60}^{1,2+}$ effusion source that enhanced the secondary ion yields for gramicidin A among other materials when compared to Ga^+, Au^+ and Au^{3+} primary projectiles.[110, 111] The source lead to several major innovations in depth profiling[112, 113] due to decrease in the damage cross sections and was commercialized shortly after. For several of the experiments discussed in this dissertation a similar custom built $C_{60}^{1, 2+}$ effusion source built in the Schweikert lab at Texas A&M University was used to perform several of the experiments. [114, 115]In 2004, Tempez et al. report the production of massive Au cluster projectiles ranging from Au_n^{q+} where n =1-1000, q=1-10 produced using a liquid metal ion source (LMIS).[116] On bombarding a variety of peptide samples with Au_{400}^{4+} they observed a ~1000 fold yield augmentation compared with monoatomic gold projectile. Furthermore, the damage cross sections observed for Au_{400}^{4+} in comparison to Au_5^+ and Au_9^+ ions were significantly decreased. Another interesting outcome was the production of Au-analyte adducts using the Au_{400}^{4+} projectiles lead to enhanced secondary ion

information in comparison with the Au_5^+ projectiles. In order to explain the enhancements observed using cluster projectile bombardment Bitensky and Parilis proposed the shock wave mechanism. They propose there is a "clearing the way" effected observed due to the stopping power of the impact of the first atoms in the cluster projectiles.[117]

At the Insitute de Physique Nucleaire d'Orsay Della Negra coupled a Au LMIS with a time of flight mass spectrometer to produce high energy Au_{400}^{4+} projectiles. Schweikert et al further developed this source to allow for single-impact events as opposed to a focused Au_{400}^{4+} focused beam. Although this source has not yet been designed to allow for imaging experiments this type of source may have major implications for imaging in the future due to potential impact on the spatial resolution being limited solely by the lateral extent of the surface area influenced by the single impact event. It has been proven to determine the nanoscale homogeneity of poly styrene cast on alumina whiskers within single impact sites.[118] Experiments at the Schweikert lab also indicate that the interaction between the Au_{400}^{4+} projectile and substrate occur via hydrodynamic penetration which is different from the overlapping collision cascade effect. The interaction involves an extreme pressure transient at the interface of the colliding solids that lasts for a few picoseconds.[119] Several physical phenomena such as impact light flash, ejection of matter and crater formation are all involved in the process.[119] The latest addition to the Au instrument includes the incorporation of a 100 keV Pegase acceleration platform to generate Au_{400}^{4+} projectiles with impact energies of up to 130 qeV with a target negatively biased target at 10 keV(Figure I-11).[120, 121]

While cluster SIMS by and large has been widely accepted in the use of organic and polymeric material analysis, cluster sources have not been used extensively for inorganic material analysis. In some cases, there can even be disadvantages in the use of some cluster sources (e.g. C_{60} sputtering of Si).[122] In this dissertation, some novel sample depositions and preparation techniques have been discussed to overcome many of these challenges. They have been employed with some success to allow for SIMS analysis to optimistically become more main stream in the analysis of inorganic nanomaterials.

Coincidence Ion Mass Spectrometry

Coincidence counting has been an important technique in the field of nuclear science for some time now.[123] Nuclear scientists monitor coincidental emission yields from radio isotopic decays. A typical coincidence experiment involves the detection of several distinct emission events simultaneously from a specific event. The concept however is a relatively unique one for the realm of mass spectrometry. Coincidence ion mass spectrometry or CIMS provides statistical correlations of secondary ions emitted from a single primary projectile impact from a conventional SIMS analysis.[124] The secondary ion yields derive directly from the emission volumes of a single projectile (an area typically 10-20nm with a 5-10nm depth), coincidentally emitted ions must also originate from the same nanovolumes thus allowing for effective nanoscale analysis. The first reported use of CIMS in mass spectrometry was conducted by LeBeyec at al. in 1983. They introduced the concept of colocalization within a 5-10 nm diameter crater

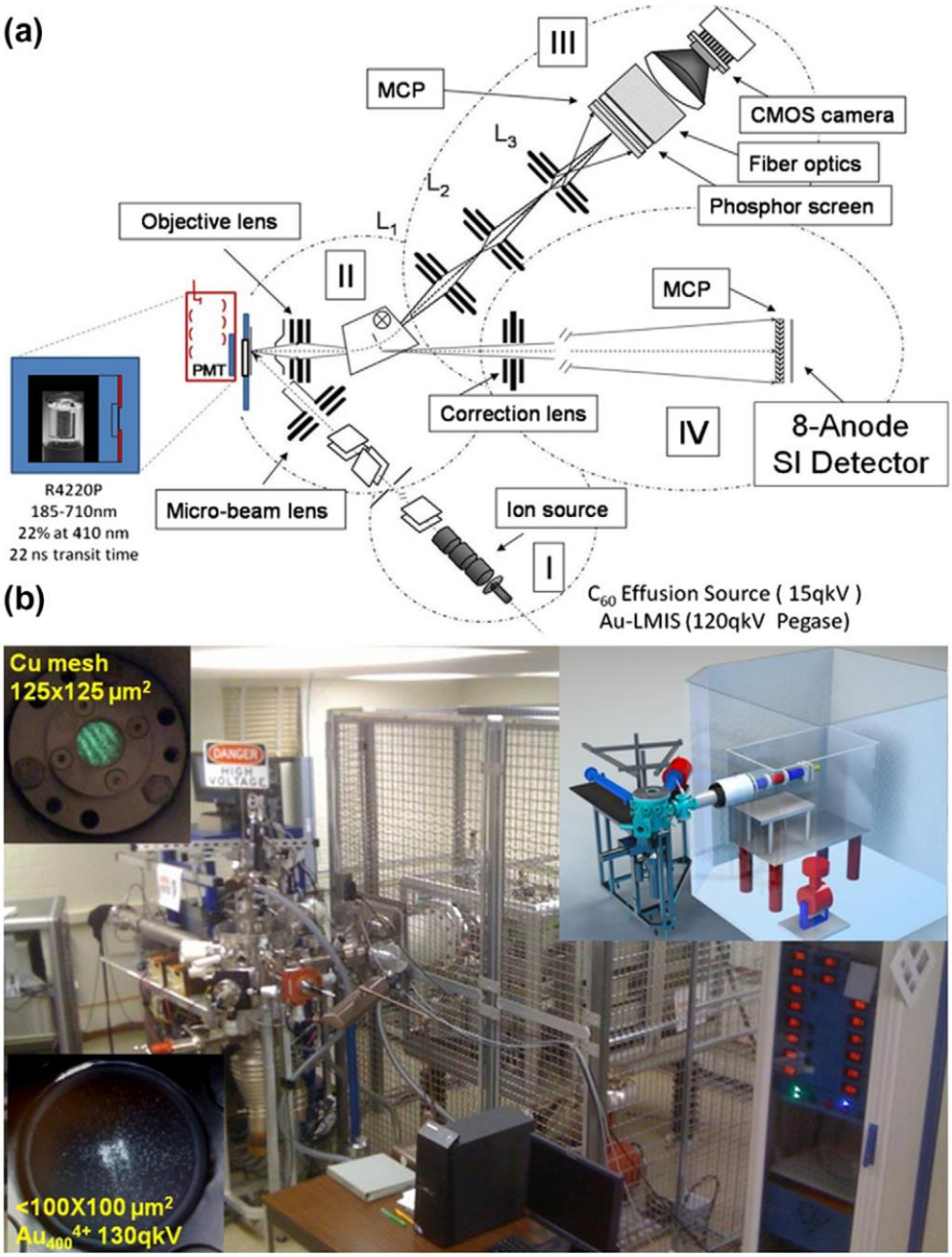

Figure I-11: (a) Schematic of the instrumental setup with both C_{60} effusion source and Au liquid metal ion source (LMIS) capable of detecting co-emitted photons, electrons and secondary ions from a single projectile impact. (b) Image of the Pegase 120 qkV platform (Au-LMIS). Top and bottom images in (b) electron images as seen in EEM phosphor screen for continuous Au_{400} beam. (Adapted from Reference 121)

with a single projectile impact and used it to study metastable secondary ion decay.[125] Schweikert and coworkers used CIMS for the first time to analyze NaF crystals and describe its chemical homogeneity.[124] However, literature on this subject still remains relatively sparse.

To better understand material morphology and chemical homogeneity of a sample by monitoring secondary ion emissions, CIMS is a very useful tool. By performing CIMS analysis in the event-by event bombardment detection mode it is possible to note colocalization between secondary ions as well as with electrons produced from each individual projectile impact. This allows for real "nanoscale" analysis. This dissertation will discuss experiments operating in the event-by-event bombardment detection mode using $C_{60}^{1,\,2+}$ (26, 43 keV) and Au_{400}^{4+} (520 keV) projectile impacts to facilitate quantitative and qualitative analysis of complex inorganic layered material systems in the realm of surface characterization and drug delivery applications. CIMS has been used most recently by the Schweikert lab to quantitatively analyze nano-objects,[104, 126-128] observe coincidental emissions of electron, photon and secondary ions[129] and for electron mapping of secondary ions.[130, 131]

Current SIMS Analysis in Drug Delivery

This section describes some of the current trends in the use of ToF-SIMS to describe and interrogate drug delivery systems. Physical and chemical characterizations are an essential part of developing dosage strategies in pharmaceutical actives. The distribution of an active pharmaceutical within a solid state matrix is of extreme value as

Imaging technique	Raman	SEM/EDX	XPS	ToF-SIMS
Spatial Resolution	> 1µm	100 Å/3-5µm	~5 µm	0.2 µm
Element Detection	Molecular information	B-U	Li-U	H-U plus molecular information
Sensitivity	> 1%	>1%	5000 ppm	ppb
Sample Limitations	Non-fluorescing	Flat and conducting	Conductors/insulator	Conductors/insulators

Table I-1: Time-of flight secondary ion mass spectrometry (ToF-SIMS) in comparison with other surface analytical methods and imaging techniques. (Adapted from reference 96)

it plays a crucial role in determining solid state stability and the drug-release profile. Raman and EDS have been applied extensively in the past to interrogate drug distribution within solid matrices; however both suffer from relatively low levels of surface specificity it (Table I-1).[96] In comparison, techniques such as XPS and ToF-SIMS offer a significant improvement in surface sensitivity. SIMS is becoming increasingly more prominent in the analysis of drug delivery systems due to three major facts: (a) low detection limits, (b) high spatial resolution and (c) high degree of surface sensitivity. It has been employed extensively especially in the past decade in the characterization of organic and polymeric materials. Several common biomedical polymers and film coatings have been studied extensively using ToF-SIMS.[132-136] In 2000 Belu and coworkers report the use of ToF-SIMS in the analysis of a multilayer drug bead assembly. They reveal the layer-by-layer polymeric matrix-drug assembly revealing specific molecular ions for each investigated drug.[89] While there has been considerable research in polymeric drug delivery matrices using ToF-SIMS, the literature on inorganic drug delivery systems such as LDHs, ZrP etc. has been scarce. In order to fill in some of those gaps, this dissertation seeks to find new and improved ways to characterizing the ILN zirconium phosphate in its applications for drug delivery. The information revealed from SIMS is used to design specific pharmacokinetic release studies and subsequent in-vitro release in a cellular environment.

It is highly desirable to correlate solid-state drug distribution within a pre-existing delivery matrix with the dissolution and pharmacokinetic drug release in order to be able to design more effective delivery matrices.

CHAPTER II

INSTRUMENTATION AND METHODOLOGY

This chapter describes in some detail the instrumentation including hardware, detection and supporting electronics utilized in performing the secondary ion mass spectrometry studies as part of the research in this dissertation. A C_{60} effusion source and Au liquid metal ion source coupled with time of flight mass spectrometry has been used to perform the previously mentioned studies. Also, the methodology developed to conduct quantitative nano-analysis of inorganic layered materials in both surface analysis and drug delivery is introduced in detail in this chapter.

C_{60} Effusion Source Mass Spectrometer

It is important to note that the instrumentation discussed is a custom built unit from the Schweikert lab at Texas A&M University. A schematic of the C_{60} source coupled to a time of flight mass spectrometer is shown in Figure II-1.[137] The instrument consists of two main ion legs. The primary and secondary ion legs are separated via a gate valve. The source operates under a vacuum pressure of ~5 $X10^{-6}$ torr with a turbo pump (60 L/s – Pfeiffer Vacuum Inc., Nashua, NH) and two-stage rotary vane mechanical pump (3.7 L/s -Varian Inc., Palo Alto, CA). The C_{60} effusion source is housed in a custom-built stainless steel chamber. The design of the source contrived in the Schweikert lab uses a design template inspired by the Vickerman group.[110, 111]

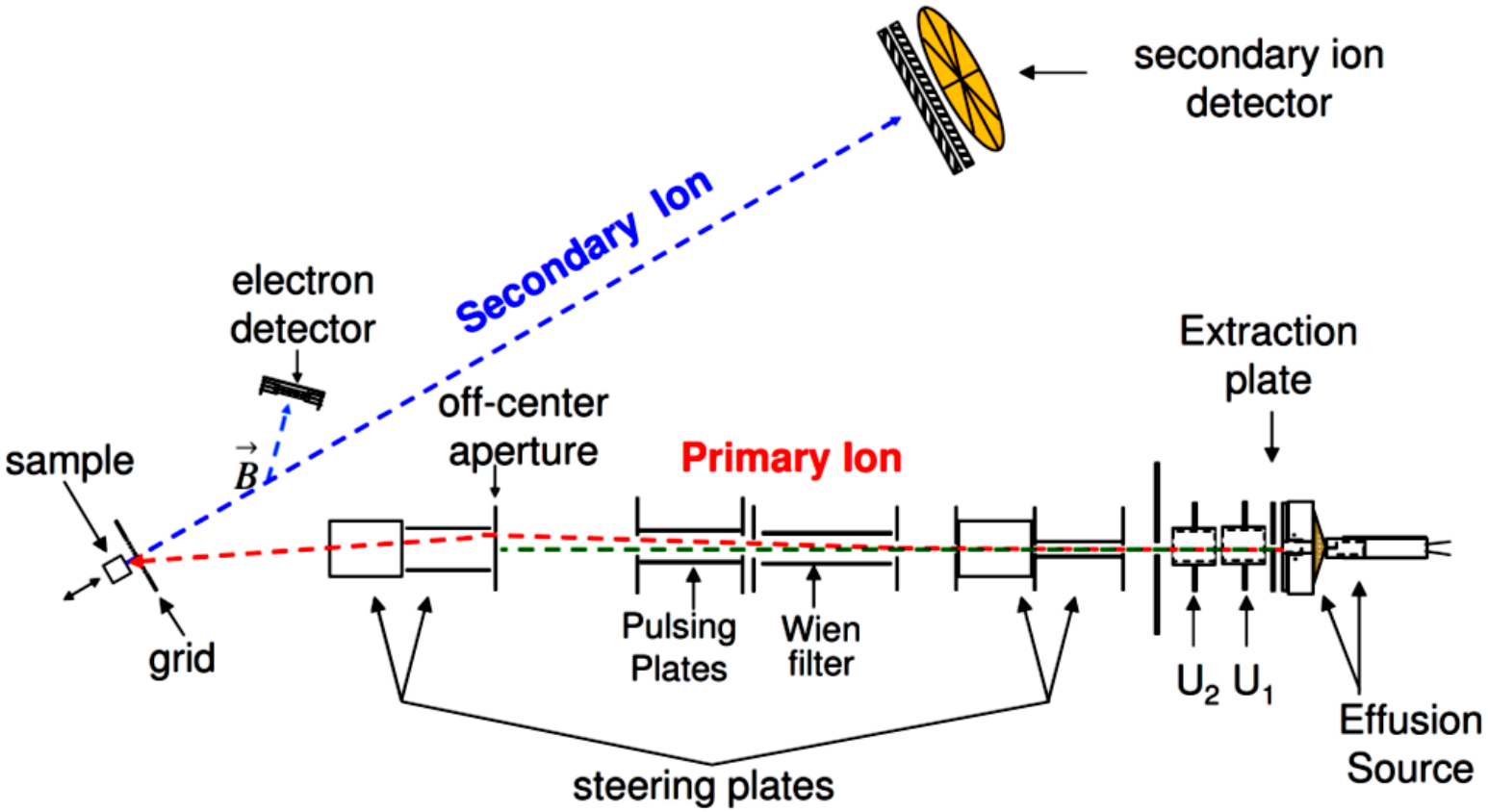

Figure II-1: Schematic of the C_{60} effusion source mass spectrometer (Reference 137)

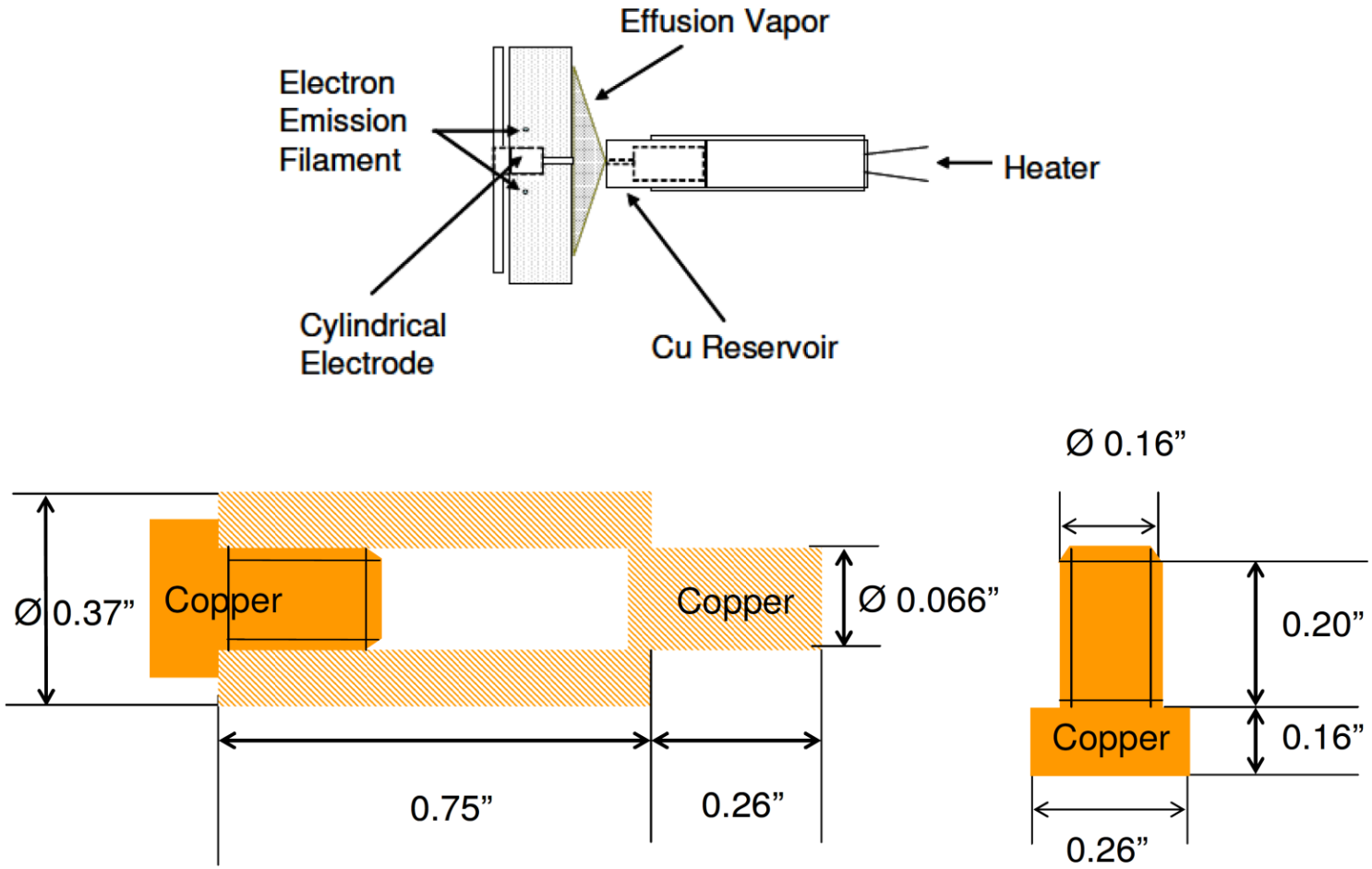

Figure II-2: Schematic illustration of the C_{60} effusion source and the copper reservoir (not drawn to scale). (References 138 & 139)

The source contains neutral C_{60} powder (Sigma Aldrich, Milwaukee, WI) packed into a copper reservoir and heated upto 450 ºC (3.9 Amp) to initiate C_{60} sublimation (Figure II-2).[138, 139] The resulting C_{60} vapor is channeled through an aperture in the reservoir into an ionization reservoir into an ionization (Figure II-2). The resulting C_{60} vapor is channeled through an aperture in the reservoir into an ionization chamber. A tungsten wire (0.1 mm diameter, Alfa Aesar, Ward Hill, MA) is positioned ~ MA) is positioned ~5 mm away with a 90 V potential drop from the cylindrical electrode. This electrode which is essentially a stainless steel tube is wrapped with a tungsten wire mesh chamber. A tungsten wire approximately 0.1 mm and 2 cm in length in diameter (Alfa Aesar, Ward Hill, approximately 0.01 inch in diameter (Alfa Aesar, Ward Hill, MA). Upon heating this tungsten framework the resulting thermally induced electrons are accelerated towards the electrode to impact the C_{60} vapor that has been channeled into the region thus resulting in the ionization of the C_{60}. The mesh covering the cylindrical electrode is grounded thus allowing for a -90 V gradient potential. This facilitates the acceleration of electrons from the filament towards the cylindrical electrode.

The resulting C_{60} ionized species are extracted with a potential gradient (0.5 kV) between the source which is maintained at16 kV and the extraction plate maintained at 15.5 kV. Electrostatic lenses are used to accelerate and focus the resultant cationic species. By employing a Wien filter the mixture of C_{60} cations are sorted and mass selected for a specific primary ion of interest (discussed in some detail in the following sections). The selected C_{60}^{+} primary projectiles are then verified by pulsing the beam over an aperture and measuring its time of flight. Any neutrals resulting from the

procedure remain unaffected by the steering potential or Wien filter mass selection. In order to remove any neutral species from the mix an off-center aperture (~ 1mm in diameter) is categorically positioned past the Wien filter. While the mass selected C_{60}^{+} are steered past this aperture the neutral species remain on an unaltered path thus effectively being extracted away from the target.

The main chamber of the C_{60} TOF-SIMS instrument is maintained at ~2 X 10^{-6} torr using a diffusion pump (760 L/s, BOC Edwards Vacuum, Tewksbury, MA) backed with a two stage rotary vane mechanical pump (5 L/s, Alcatel Vacuum Product, Hingham, MA). The sample inlet chamber is segregated from the main chamber via a gate valve and maintains a vacuum of ~5 X 10^{-6} torr during sample introduction. The total impact energy of the C_{60}^{+} primary ions is 26 keV. The primary ions are extracted by applying 16 keV to the effusion source and a 10 keV potential drop is applied to the negatively biased target.

Once past the collimating aperture, the C_{60}^{+} primary projectiles are steered towards the negatively biased target with a set of horizontal and vertical plates. Upon impact with the negatively biased target the C_{60}^{+} projectiles lead to the production of secondary ions, electrons, photons and neutral species. By applying a magnetic field (< 100 Gauss) the resulting electrons are deflected towards a start detector that consists of microchannel plates (MCPs) arranged in the chevron formation. This detected signal motions as the start of a collision event. The simultaneously ejected secondary ions travel through a field free time of flight drift tube (92.9 cm in length) towards a grounded grid (90% transmission, attached in front of the time-of-flight tube). This

results in a -10 keV potential gradient. The secondary ions are detected by an 8-anode detector as the stop signal for the time of flight event.

This 8-anode detector consists of 8-separate copper plates assembled with a dual MCP assembly. The detector can simultaneously record upto 8 distinct ions with the same flight time striking the MCPs. The distribution of the detected species can be monitored using an in-house data acquisition program. In order to optimize the distribution of the secondary ion detection, voltages maybe applied onto the respective steering plates to change the position of C_{60}^{+} primary ion impact. The upkeep and maintenance of the C_{60} effusion source has been described in detail elsewhere.[137]

Au Liquid Metal Ion Source Mass Spectrometer

A detailed description of the instrument is available elsewhere.[140, 141] In brief, the instrument consists of a primary ion leg where the pressure is maintained at less than 1 X 10^{-6} torr using a turbo pump (400 L/s, Adixen, ATP400, Alcatel Vacuum Technology France) and backed by another mechanical pump composed of 5 root type stages (Adixen, ACP28, Alcatel Vacuum Technology France). A schematic of the instrument is shown in Figure II-3.[139] The primary ion leg is where the primary ion generation and the subsequent delivery of the cluster projectiles to the target surface takes place. It consists of a gold liquid metal ion source (Au-LMIS) focusing lenses, Wien filter and pulsing plates. The length of the primary ion leg is approximately one meter from the LMIS to the target.

The Au-LMIS was originally developed by Serge Della Negra and coworkers at the Institute de Physique Nucleaire d'Orsay (IPN in Orsay, France) and the mass spectrometer was assembled in the Schweikert research lab at Texas A&M University. It consists of a tungsten spring reservoir consisting of a tightly wound tungsten coil with approximately 8-10 turns and a tungsten needle (0.2 mm diameter; 20 mm length). Refer Figure II-4 for a schematic.[140] The needle is electrolytically etched to have a ~90º angled tip and arranged centrally within the confines of the coiled reservoir. This is done to facilitate the formation of a Taylor cone, in which case the Au clusters are emitted from the tip of the needle during primary ion extraction. The reservoir and needle assembly is then dipped into a Au-Si eutectic (97% Au, 3%Si by mass, Academy Precious Metals, Albuquerque, NM). Primary ions are extracted by heating the Au/Si eutectic to its melting point (~363 ºC) and applying an extraction potential (6.9-7.4 kV) between the needle tip and the extraction electrode (0.5 mm away). The fabrication of the Au-LMI is The fabrication of the Au-LMIS is detailed in these references.[141, 142]The Au-LMIS is floated at 20 keV relative to the platform providing primary ions with 120 qkeV total kinetic energy. The resulting Au projectiles are then accelerated to 130 qkeV to impinge upon the negatively biased target (10 keV). The LMIS emits a wide range of gold projectiles Au_n^{q+} ranging anywhere from $1 \leq n \leq 1000$ and $1 \leq q \leq 10$. The projectile beam is focused using an einzel lens assembly. The details for the einzel lens potential adjustment for this instrument can be found elsewhere.[141] The beam current, which is measured using a Faraday cup without pulsing is measured to be ~200 nA. Post focusing, the projectile of interest is mass selected using a Wien filter (discussed further

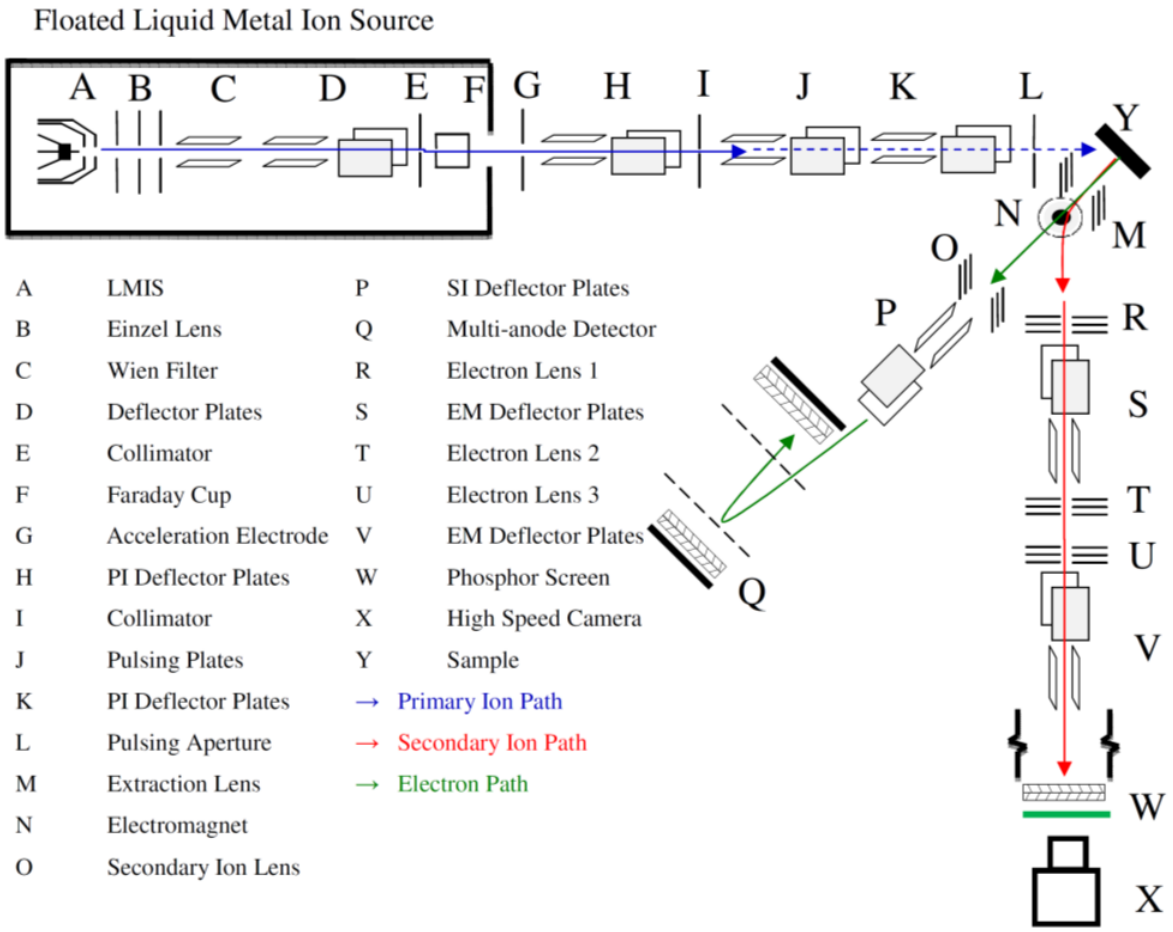

Figure II-3: Schematic of the Au-LMIS ToF-secondary ion mass spectrometer. (From reference 139)

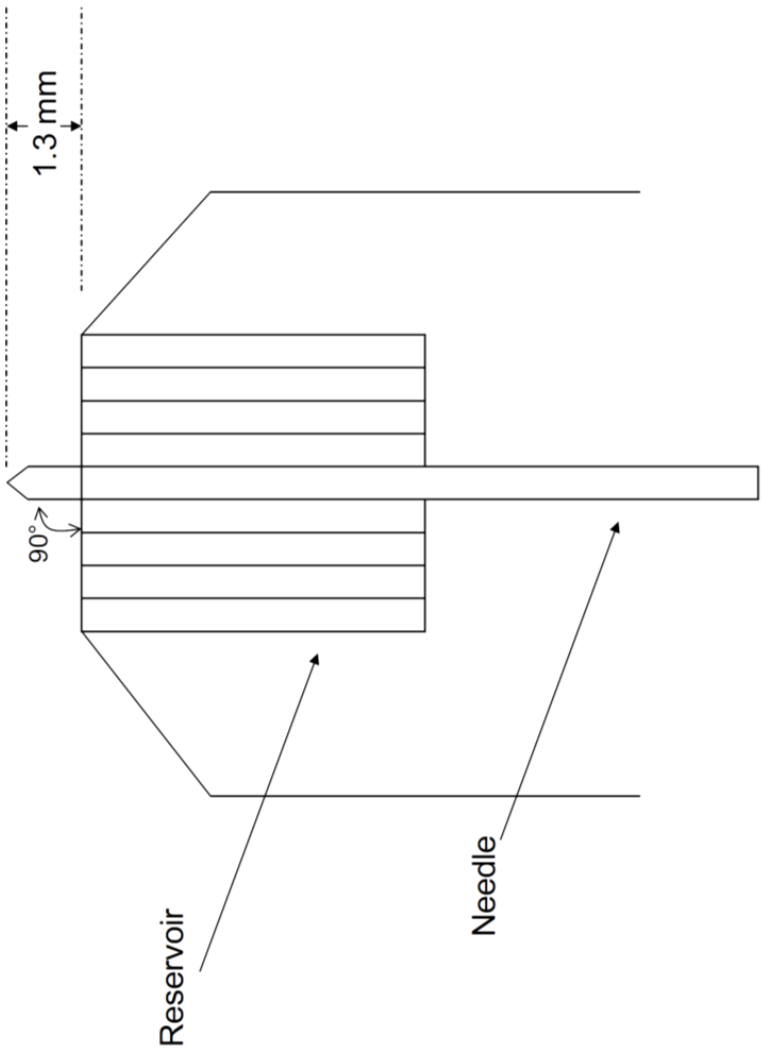

Figure II-4: Schematic of the ion source (Reference 142)

in following sections). The mass selected projectiles are then deflected onto a pair of collimators where they pass through. These collimators have a variable set of apertures ranging from 5mm, 1mm, 500μm and 200μm. The projectiles are steered by applying voltages to the primary ion deflection plates and passing through the second collimator before entering the pulsing system.

The beam is pulsed in order to provide a start signal for the primary ion time of flight so as to verify the mass to charge ratios of the particles. The second reason for pulsing is to reduce the beam flux so as to enable event-by-event bombardment/detection. The pulsing system consists of a set of horizontal and vertical plates (-1 keV to +1keV at 3 kHz). Subsequently, the primary projectiles are steered towards an exiting variable aperture (200μm, 500μm or 5mm) to finally impinge upon the negatively biased target at -10keV. To assure only a single Au_{400}^{4+} projectile impacts, a fluence of 1000 primary ions per second is set. Post interaction the electrons that are produced as a result are deflected onto a MCP assembly to capture the start signal, a lot like the previously mentioned C_{60} instrument. The secondary ions produced simultaneously are accelerated towards a grounded grid at which point the secondary ions enter the field free drift region. This maybe linear or reflectron time-of-flight analyzer. The secondary ions are detected by a dual MCP assembly and an 8-anode detector(Figure II-5). By changing the voltages of the horizontal and vertical steering plates it is possible to alter and adjust the monitoring of the secondary ion distribution.

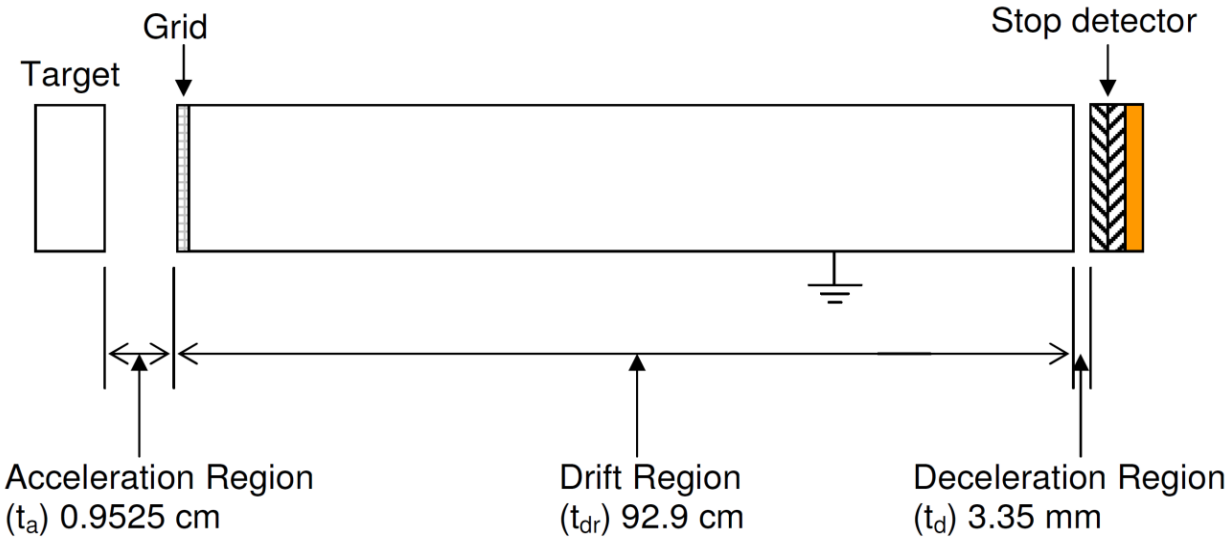

Figure II-5: Schematic representation of the time of flight mass analyzer in the C_{60} instrument (not drawn to scale) (Reference 139)

Time of Flight Mass Spectrometry

Both the C_{60} and Au-LMIS instruments work on the principles of time of flight for the mass analyzers used in the course of the experiments discussed in this dissertation. Using a time of flight mass analyzer ensures that all the events are sampled when compared to other techniques such as quadrupole mass filters, magnetic and electric sector instruments, in case of which greater than 90% of the ions, go undetected.[143] ToF mass analysis is possible because temporal separation occurs in a field free drift region of ions having the same kinetic energy, but different masses and therefore different velocities.[140]

The secondary ions that are produced are influenced by two distinct regions that directly affect its recorded time of flight. The first is the acceleration region (Figure II-3). The time it takes to traverse this regions, ta, is:

$$t_a = \sqrt{\frac{2L_a^2}{V_a}}\sqrt{\frac{m}{q}} \qquad \textbf{Eq.II-1}$$

where L_a is the length of the accelerating region, Va is the bias applied in the acceleration region; m is the mass of the ion with a charge q. Once past the acceleration region the secondary ions will now encounter the drift free region. The time taken by the ion at this juncture can be calculated as follows:

$$t_{dr} = \sqrt{\frac{L_{dr}^2}{2V_a}}\sqrt{\frac{m}{q}} \qquad \textbf{Eq II-2}$$

Where L_{dr} is the length of the drift free region. The last contributing factor for the total time of flight is the deceleration region L_d with the application of a high voltage bias V_d, the time taken to traverse this region maybe calculated as follows:

$$t_d = \frac{L_d^2}{V_d}\sqrt{\frac{2m}{q}}\left(\sqrt{V_a + V_d} \pm \sqrt{V_a}\right) \qquad \textbf{Eq. II-3}$$

Thus bringing the total time of flight for the ion to t_{tot}:

$$t_{tot} = t_a + t_{dr} + t_d = \sqrt{2}\sqrt{\frac{m}{q}}\left(\sqrt{\frac{L_a^2}{V_a}} + \frac{1}{2}\sqrt{\frac{L_d^2}{V_a}} + \frac{L_d^2}{V_d}\left(\sqrt{V_a + V_d} \pm \sqrt{V_a}\right)\right)$$

Eq. II-4

A more detailed explanation for these derivations have been discussed elsewhere.[100, 102, 103, 105]

Once the spectrum is collected it must be mass calibrated. Knowing that the flight time, t_{tot}, of an ion is proportional to the square root of its *m/q* ratio, all other factors can be reduced to two constants giving rise to the following:

$$t_{tot} = \sqrt{\frac{m}{q}}C_1 + C_2 \qquad \textbf{Eq. II-5}$$

Where C_1 is a constant determined by the sample bias and flight length and C_2 is determined by the speed of the timing electronics.[124, 144] Out of all the unknowns if the identities of at least two ions are known, then it is possible to solve a system of two equations for C_1 and C_2 to calibrate the entire spectrum. A more precise determination can be made through iterative determinations of C_1 and C_2.

The mass resolution, is the capability of the mass spectrometer to distinguish two peaks of slightly different mass-to-charge ratios Δm, in a mass spectrum. The mass resolution, R, for a mass spectrometer can be defined as:

$$R = \frac{m}{\Delta m} = \frac{t}{2\Delta t} \qquad \textbf{Eq. II-6}$$

Where m is the measured value at the center of the peak at mass m; Δm is measured at the full width at half maximum (FWHM). The mass resolution for the studies presented in this thesis is ~600 at m/z 74.

Detectors and Detection Electronics

Once the electrons and secondary ions are emitted the signals from them are amplified by striking a microchannel plate (MCP) (Photonis, Pittsfields, MA) assembly. Microchannel plates are generally lead-doped glass electron multiplier microtubes (dynodes) set in parallel arrays. The outside diameter of the MCPs for secondary ion detectors is 50 mm with the active area ~40 mm in diameter and a thickness of 0.46 mm. Fused together, they form a thin plate which can be used singly or stacked together. When the electrons or secondary ions interact with the microchannel plate an electron cascade is formed, resulting in a ~10^3 gain across a single MCP. In the detector assemblies used in the mass spectrometers here (Figure II-6), MCP's are used in Chevron formation.[143] The total assembly consisting of two microchannel plates is ~10^6.

The electron cascade that results from a particle impact on the MCP assembly is collected at the exit of the MCP using a copper anode. In the case of the electron detector, a single copper plate is used as a "single anode" collector. The stop detector for

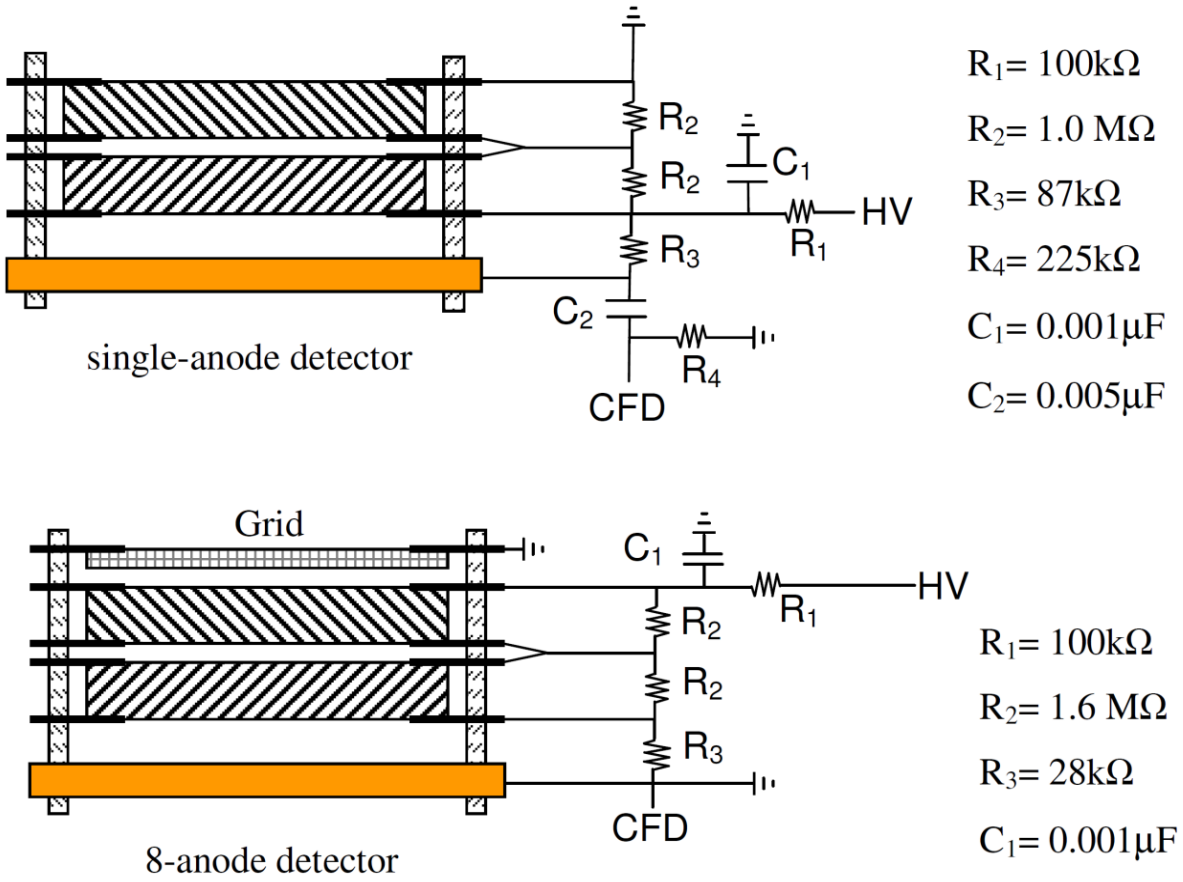

Figure II-6: Schematic of micro-channel (Chevron formation) plates for start and stop detectors (not drawn to scale). (Reference 139)

the secondary ions consists of an 8-anode detector allowing for upto 8 isobaric ion detection per event. The 8-segment collector made from a copper plated circuit board is discussed in detail elsewhere.[140] A newly modified anode was installed on the C_{60} instrument.[139] Using an 8-anode detector ensures that each anode registers equal amounts of ions and the detector therefore achieves the maximum detection capability. This results in a detection efficiency of ~40% for the experiments performed in this thesis.[143]

Signal Processing

The electron flux once collected by the anode is processed by a quad CFD (Tennelec, Meriden, CT). The output signal from the SI detector is passed to an octo-port CFD (Ortec, Oak Ridge, TN). The CFD transforms the negative voltage pulse from the anode into a NIM (Nuclear Instrumentation Module - square wave) pulse which proceeds to the time to digital converter (TDC).[142] The CFD helps set a threshold for signals allowing only those above a certain limit to pass onto the TDC for processing. The TDC has one input for the "start" signal and 8 "stop" signals. The start signal initiates a data acquisition window during which stop signals are collected. The TDC converts the NIM pulse to a digital signal which is recorded. The digital output is processed by the "Total Matrix of Events" (TME), which is an in house processing software described in depth elsewhere.[141] This software helps draw relationships between individual emission events as well as calculate secondary ion yields.

Event-by-Event Bombardment/Detection Mode

The key defining feature for the mass spectrometry methodology used in these experiments is the use of the event-by-event bombardment/detection mode. Single projectiles impact the target surface and the resulting secondary electrons and ions are collected as individual "events". As noted earlier, the sampling is performed in a stochastic manner ensuring the same spot isn't sampled more than once. Each cluster impact causes a nanovolumetric impact crater. The fragmented secondary ions are co-ejected after each projectile impact and are resolved separately in time and space as "singular" events. An event is defined by a single projectile impact, the detection of the resulting electrons as the start and subsequently detecting the resulting secondary ions. For a typical experiment anywhere over a million events are collected. The Schweikert lab employs the concept of coincidence counting in conjunction with ToF-SIMS for further analysis. Park et al report some requirements for coincidence counting: 1) in order to spatially distinguish the components of the samples the sampled regions should be small; 2) each component of the sample must generate distinct secondary ions to enable chemical distinction. In the case of samples bombarded by the $C_{60}^{+,2+}$ and Au_{400}^{4+} projectiles, the volume from which secondary ions are emitted is ~10^3 nm^3. Using the event-by-event bombardment detection it is possible to identify co-located species within nanodomains using coincidental ion mass spectrometry. From the coincidence ion mass spectrum the co-emissions can be deconvoluted from the cumulative secondary ion mass spectrum (seen in Figure II-6). Once individual ions from complex surfaces are identified, using coincidental ion mass spectrometry. The coincidental emission intensity

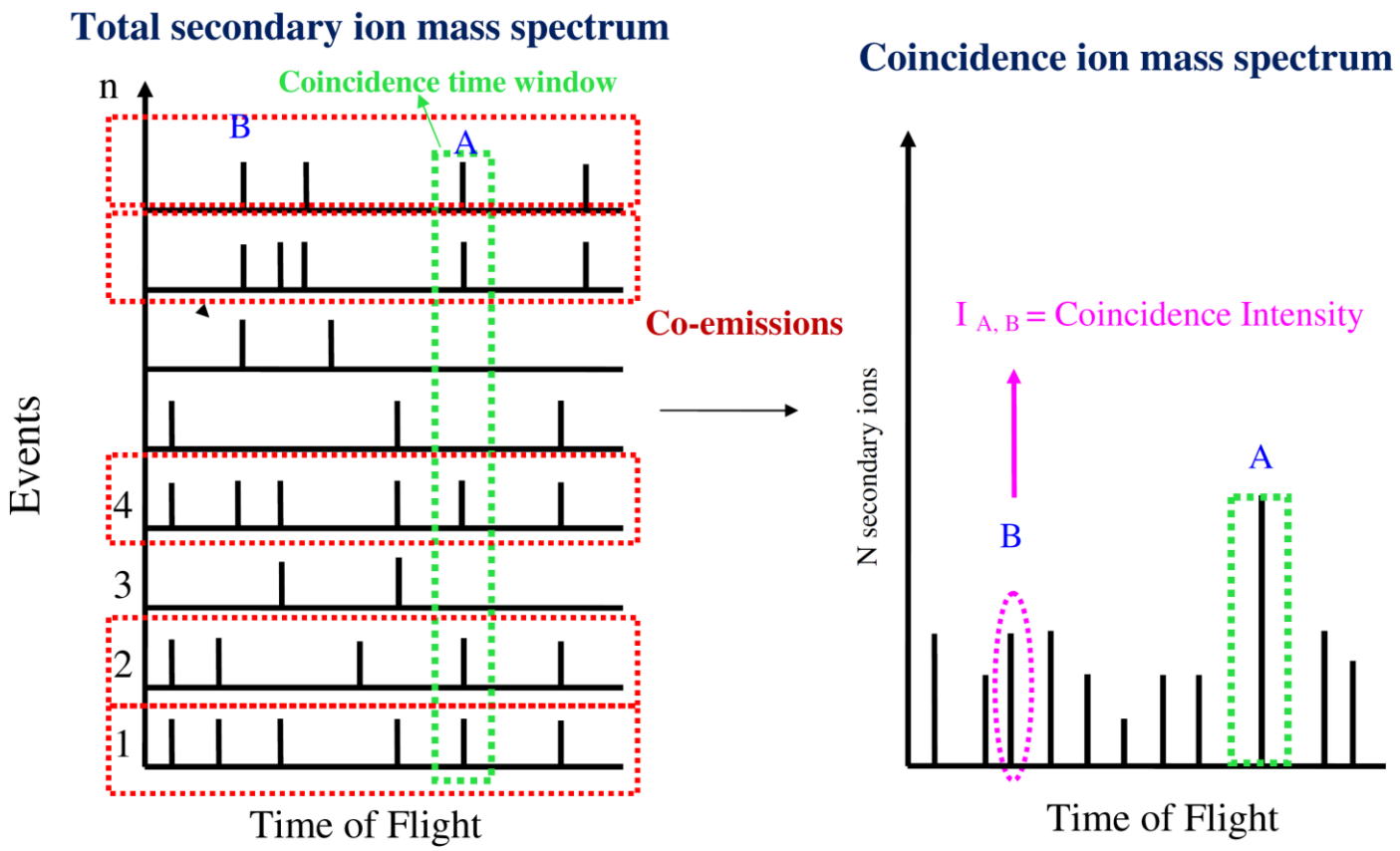

Figure II-7: Schematic illustration of coincidental ion mass spectrum.

of two specified ions allows for a variety of applications in the quantification of surface immobilized species(Figure II-7). In this dissertation, the concept of coincidental ion mass spectrometry is applied to quantify the surface modification of nanomaterial. Before addressing the concept of the quantitative analysis, the correlation coefficient is defined below.

Correlation Coefficient

In nuclear science correlation coefficient is a widely employed concept using coincidentally detected signals.[123] The yield of the detected ions A is computed as in Eq. II-7:

$$Y_A = \frac{I_A}{N_T} \qquad \textbf{Eq. II-7}$$

I_A is the measured peak area under ion A. N_T is the total number of projectile impacts sent to bombard the target surface Coincidental yields can be experimentally determined for two ions, A and B, given:

$$Y_{A,B} = \frac{I_{A,B}}{N_T} \qquad \textbf{Eq. II-8}$$

Where $Y_{A,B}$ is the coincidental yield for ion A coemitted with ion B, $I_{A,B}$ is the experimental relative intensity for ion A in coincidence with ion B. The secondary ion yield is expressed as follows:

$$Q_{A,B} = \frac{Y_{A,B}}{Y_A Y_B} \qquad \textbf{Eq. II-9}$$

Y_A and Y_B are the secondary ion yields of the detected ions A and B respectively. The correlation coefficients Q correlated to the spatial homogeneity of chemical species are summarized as follows:

$\boldsymbol{Q = 1}$, the emission of two coincidental ions A and B originated from a nanovolume is uncorrelated, i.e., when ions A and B are emitted independently, the probability of the co emission is equal to the product of each individual emission/detection probability.

$\boldsymbol{Q > 1}$, the emission of ions A and B is correlated, i.e., the emission of ion A enhances the emission of ion B.

$\boldsymbol{Q < 1}$, the emission of ions A and B is anti-correlated, i.e., the emission of ion A suppresses the emission of ion B.

Quantitative Methodology

The concepts of fractional coverage and material homogeneity are applied to some of the studies discussed in the course of this thesis. They are used to identify the quality of immobilized molecules on the surface of nanomaterials and the physical assemblies of complex layer by layer drug-nanomaterial assemblies. The quantitative methodology, extent of surface coverage is in terms of the ratio of the number of effective impacts in specific species to the total number of projectile impacts sent to bombard the target surface. The sample preparation procedures used to fabricate the sample depositions in each of the studies is described in detail in the next chapters.

CHAPTER III

SURFACE FUNCTIONALIZATION OF ZIRCONIUM PHOSPHATE

Introduction

The modification of platforms with multiple molecules or containing molecules with varied functional components has become increasingly popular in the past two decades.[145] When it comes to the characterization of morphologies in the nanometric scale there is a general consensus that more needs to be done to improve the characterization of these materials.[16, 17] Considerable effort has been devoted to the design and controlled fabrication of nanostructured materials with functional properties. The ability to control the surfaces with high precision and level of control has led to the need for characterizing these molecular constructs by which the surfaces are modified. Effective strategies to build tailored nanomaterials reliably and predictably are required in order to meet the ever-increasing demands (e.g., structural and compositional complexity) placed on materials synthesis and performance by nanotechnology.[146] Surface tethered molecular components can serve a multitude of scopes, including coupling biomaterials,[2] allowing electron transfer through layers,[3-5] sensors and biochips,[6, 7] drug delivery,[8-10] photovoltaics,[12, 13] fuel cell,[14] and molecular electronics,[2, 12, 15]as well as controlling reactions at surfaces,[5] and tailoring surface properties.[147]

Zirconium phosphates (ZrP's) are the ideal class of sophisticated acidic, inorganic cation exchange materials for surface modification reactions. The ease of synthesis, of crystallinity and size control has allowed for α-ZrP to be used as the model

system for intercalation and surface modification chemistry studies for over four decades.[148-151] The tunability of the size, morphology and aspect ratios[30] of ZrP has opened up a wide range of applications[11, 40, 45, 152-158] through the immobilization of organo and metal-based modifiers. By custom designing the surface of the ZrP for specific applications, its applicability in the realm of catalysis, drug delivery, as polymeric surface interfaces among many others can be greatly enhanced. Establishing a technique to monitor the surface coverage can help maximize the respective application properties.

This chapter reports the surface modification of the α-phase of the ZrP with a host of different modifiers based on the reaction of the surface which consists of parallelogram arrays of P-OH groups. This was monitored and followed using secondary ion mass spectrometry (SIMS) in the event-by-event bombardment mode using the custom built C_{60}^{+} instrument described in the previous chapters in conjunction with thermo gravimetric analysis (TGA), infrared spectroscopy(IR), nuclear magnetic resonance spectroscopy (NMR), microprobe analysis and x-ray powder diffraction (XRPD) techniques to determine the quality and tentative degree of surface coverage. Although the exact bonding arrangement was not immediately apparent the quality of surface coverage was easily identified using these techniques in conjunction. The evolution of self-assembly techniques for surface modification has led to a wealth of research on the construction and applications of nanostructures thin film materials.

Previous investigations have demonstrated that inorganic particles dispersed in aqueous solutions can be coated with a variety of organic and inorganic materials either

by precipitation of the coating material, or by direct surface interaction through covalent bonding utilizing specific functional groups on the cores to induce coating.[159, 160] The layered compounds obtained in this manner are considered organic derivatives of the parent. It is possible to change the hydrophobic/hydrophilic character of the surface of the material by interspersing the inorganic P-OH groups with suitable organic modifiers.[161]

The structure of α-ZrP has a layered configuration in which the Zr ions are slightly above and below the mean plane of the layer. Three of the monohydrate phosphate oxygen atoms bond to three adjacent Zr ions with phosphate groups alternating above and below the plane. The remaining OH groups points out toward the interlammelar space. A very attractive aspect of zirconium phosphate chemistry is related to the possibility of replacing the P-OH groups anchored to the layer surface with P-OR or P-R groups without altering the inorganic texture of the layer (R is an organic group).[162] Schematic representations of α-ZrP are provided in Figure III-1.

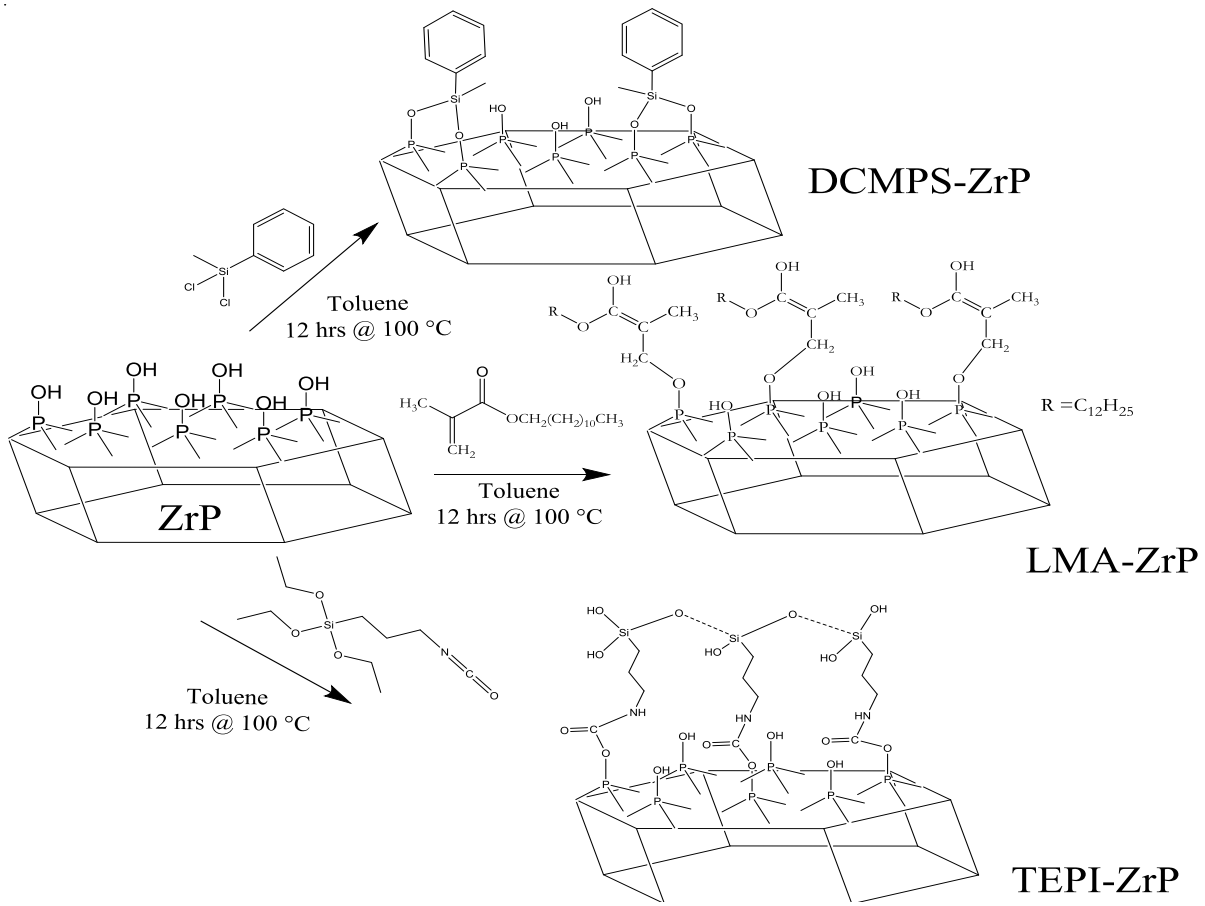

Figure III-1. Schematic of surface functionalized zirconium phosphate nanoplatelets surface modified by dichloromethylphenylsilane (DCMPS), lauryl methacrylate(LMA) and 3-(triethoxysilyl)propylisocyanate(TEPI).

Experimental Section

Materials

In this study all the chemicals were purchased from Sigma-Aldrich Chemical Co. and used as received with the exception of phosphoric acid, 85% (v/v) (H3PO4), which was purchased from Fisher.

Synthesis

The synthesis of the ZrP nanoparticles was performed by following the procedure outlined by Kijima in 1982.163 200 mL of 0.05M ZrOCl2.8H2O aqueous solution was added drop wise to a 200mL solution of H3PO4 (6M) preheated to 94°C. The resulting solution was refluxed for 2 days. The product was washed several times with deionized water and dried at 70°C resulting in a powder which is ground up and characterized by XRPD, FTIR and TGA, SIMS, NMR and depth profiling respectively.

The surface modification of the α-ZrP nanoparticles was carried out by suspending the nanoparticles in hot toluene at 75 °C for the 3-(triethoxysilyl) propyl isocyanate (TEPI), dichloromethylsilane (DCMPS) modifications for 1 h under constant stirring and switching between vacuum and N2 atmosphere in a Schlenk line with a condenser attachment, to eliminate all the water from the surface of the α-ZrP. A solution of each respective modifier was dissolved in toluene (200 mL final volume) and was then added (1:10 TEPI/ZrP & 1:10 DCMPS/ZrP molar ratio) and reacted with the "dry" α-ZrP suspended in the toluene for 12 h. The product was washed several times by

centrifugation with dry hexanes, and then with a mixture of hexanes and ethanol. The final product (TEPI/α-ZrP & DCMPS/ α-ZrP) was dried at 80 °C for 24 h. The lauryl methacrylate (LMA) reaction was performed in a round bottom flask in hot hexane at 75 °C for 12 hours in a 7:1 LMA/ α-ZrP molar ratio with a condenser attachment. The resulting product was treated the same as the other two modifications (vide supra).

Instrumentation

Once the materials were synthesized the complete characterization of the materials was performed using several analytical techniques. X-ray powder diffraction (XRPD) patterns were collected with a Siemens D8 diffractometer using CuK α radiation (1.5418 Å) at 40 kV and 40 mA with a filtered flat LiF secondary beam monochromator. The measurements were recorded from 2‑40° (2θ range). Bragg's law was applied to the (002) diffraction plane of the α-ZrP diffraction pattern to determine the interlayer distance. According to Bragg's Law the distance (dh*kl*) between planes (*hkl*) is equal to the ratio between the wavelength of the source and 2 times the sine of the diffraction angle, or as is expressed in the equation of the Law:

$$d_{hkl} = \frac{\lambda}{2sin\theta} \qquad \textbf{Eq. III-1}$$

Thermogravimetric analyses were performed with a TA Q500 instrument. The temperature was ramped at 10 °C min^{-1} under a flow of air/N_2 9:1 up to 1000 °C.

Quantitative compositional analyses were carried out on a four spectrometer Cameca SX50 electron microprobe. Analyses were run at an accelerating voltage of 15

kV at a beam current of 20 nA. All quantitative work employed wavelength-dispersive spectrometers (WDS). Analyses were carried out after standardization using very well characterized compounds or pure elements. Qualitative analyses (spectra) were obtained with an Imix Princeton Gamma Tech (PGT) energy dispersive system (EDS) using a thin-window detector.

Typical accuracy for major elements (> 10 wt. %) is about =+/- 1 to 2 % of the amount present; the uncertainty at low concentrations would increase as the concentration decreased, with the uncertainty reaching 100% at the lower limit of detection (LLD). The lower limit of detection for most elements under typical conditions would usually be about 0.05 to 0.10 wt. %. Pressed powder samples will have some additional uncertainty based on surface roughness. The main effect of surface roughness will be to reduce analytical totals because of X-ray scatter. However, X-ray scatter is also wavelength dependent, which could result in a few percent change in apparent elemental ratios if the surface is very rough and there are significant differences in wavelength.

The secondary ion mass spectrometry measurements were carried out with the custom-built instrument coupled to a 1 m linear time-of-flight (TOF) mass analyzer described in the previous chapter.[164] The $C_{60}^{+,2+}$ and Au_{400}^{4+} projectiles were used to perform the experiment in this chapter. The SIMS analysis for each of the samples was conducted in the super static regime, where less than 0.1% of the surface is impacted. This enabled stochastic sampling. The measurements were collected in the event-by-event bombardment detection mode, meaning the secondary ions from a singular

projectile impact were collected and analyzed prior to the ensuing impact. All the collected secondary ion information is derived from ~5 nm excavation radius on the sample surface. Each sample interrogation consisted of ~1.5×10^6 projectile impacts on an area ~ 100 μm in radius thus, sampling several million particles stochastically to retrieve relevant surface information. Multiple measurements were performed to ensure sample consistency.

The transmission electron micrographs (TEM) of the samples were acquired using a JEOL 2010 transmission electron microscope at an acceleration voltage of 200 kV. Samples were prepared using copper grids from Ted Pella. The FTIR were performed using a Shimadzu IRAffinity-1 spectrophotometer in an ATR (attenuated total reflection) mode.

Results and Discussion

For each surface modification reaction the X-ray powder diffractograms for the pristine α-ZrP and the surface modified materials are compared in Figure III-2. To ensure the modification was solely sequestered onto the surface each of the three resulting products were monitored. The diffractograms reveal no significant alteration in the layer lattice arrangement of the α-ZrP in each of the three cases vs. that of pristine α-ZrP. This is evidenced by the characteristic 002 diffraction peak at 7.6Å attributed to the α-phase in each case and the absence of diffraction peaks at lower angles.

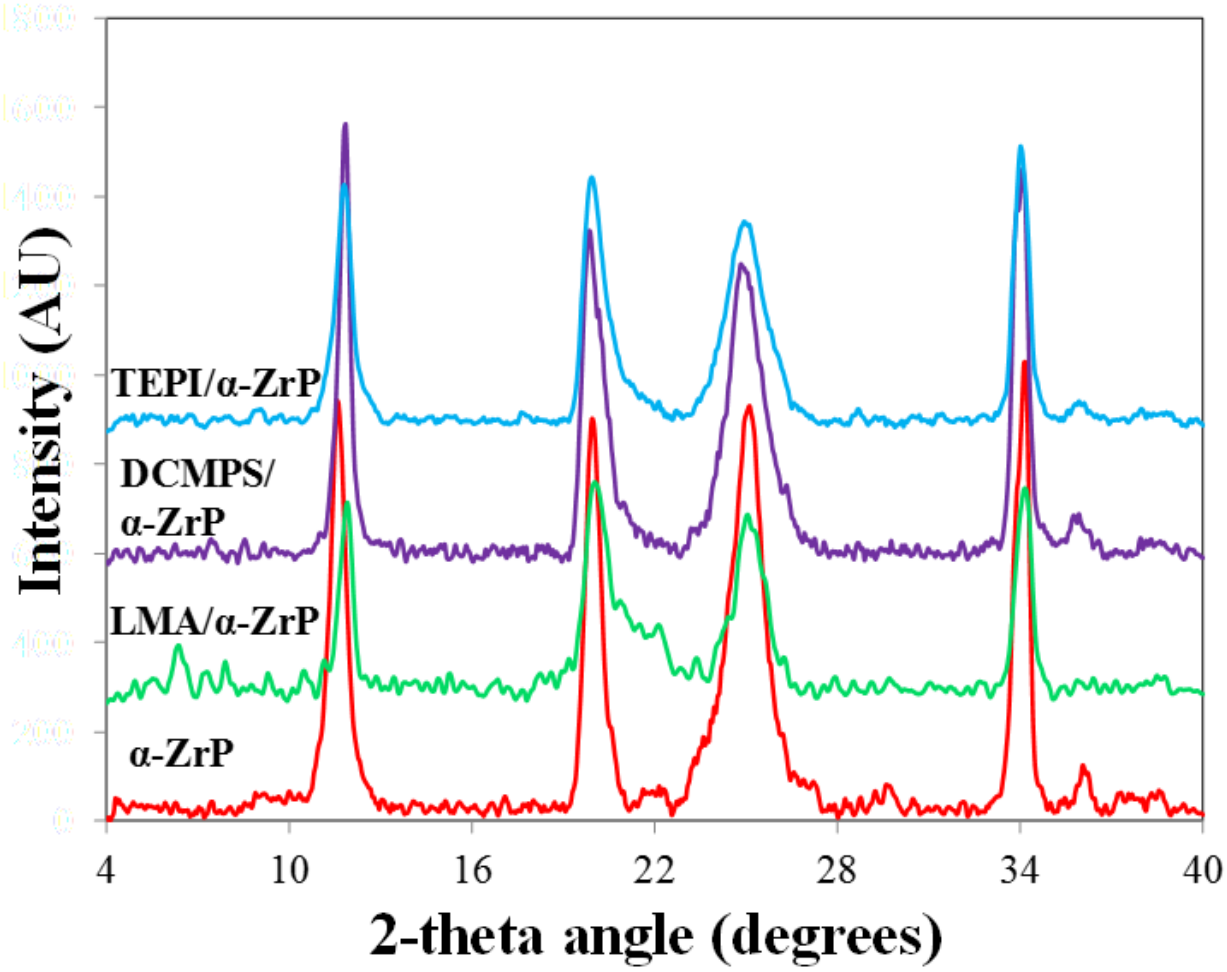

Figure III-2. X-ray powder diffraction of α-ZrP before (red) and after LMA (green), DCMPS (violet) and TEPI(blue) surface modification

The TEM images reveal no significant alteration in surface chemistry from that of pristine α-ZrP (Figure III-3) in the case of both TEPI (Figure III-4) and DCMPS (Figure III-5) modifiers, however the modifier LMA (Figure III-6) appears slightly altered.

The FTIR patterns were monitored for all the modified materials and compared to the pristine α-ZrP to reveal respective characteristic stretches which have been summarized in Figure III-7. α-ZrP has two characteristic IR bands that correspond to the splitting of the crystallization water band at 3590 and 3510 cm^{-1}, ν_{as} (OH),[165] which remains in the spectrum of the surface-modified materials in each case. This resonance becomes less intense when the adsorbed amount of modifier increases. It also confirms the XRD results showing that there was no intercalation or displacement of the intercalated water molecule. In addition, the FTIR spectrum of TEPI /α-ZrP shows the disappearance of the strong characteristic bands associated with the isocyanate band at 2260cm^{-1} in the reaction product which maybe indicative of the reaction of the isocyanate group with the hydroxyphosphate on the surface of ZrP (Figure III-8a). Additionally the appearance of the secondary amine band at 3375cm^{-1} (Figure III-8b) along with the symmetric stretching of the C–H, between 2900 and 3000cm^{-1} in the reaction product also indicates modification.

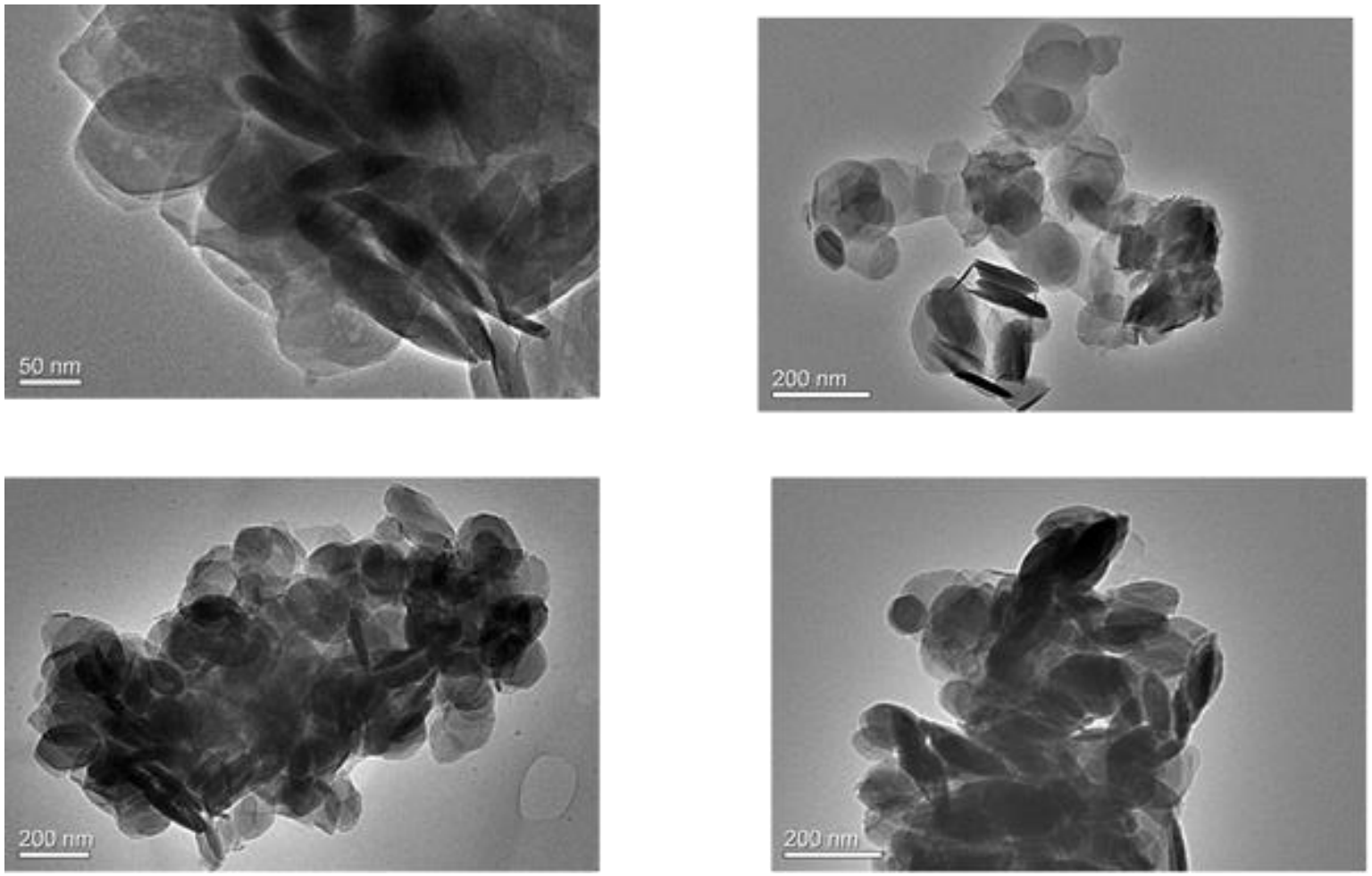

Figure III-3: TEM images of pristine α-ZrP (~150 nm) prior to surface modification

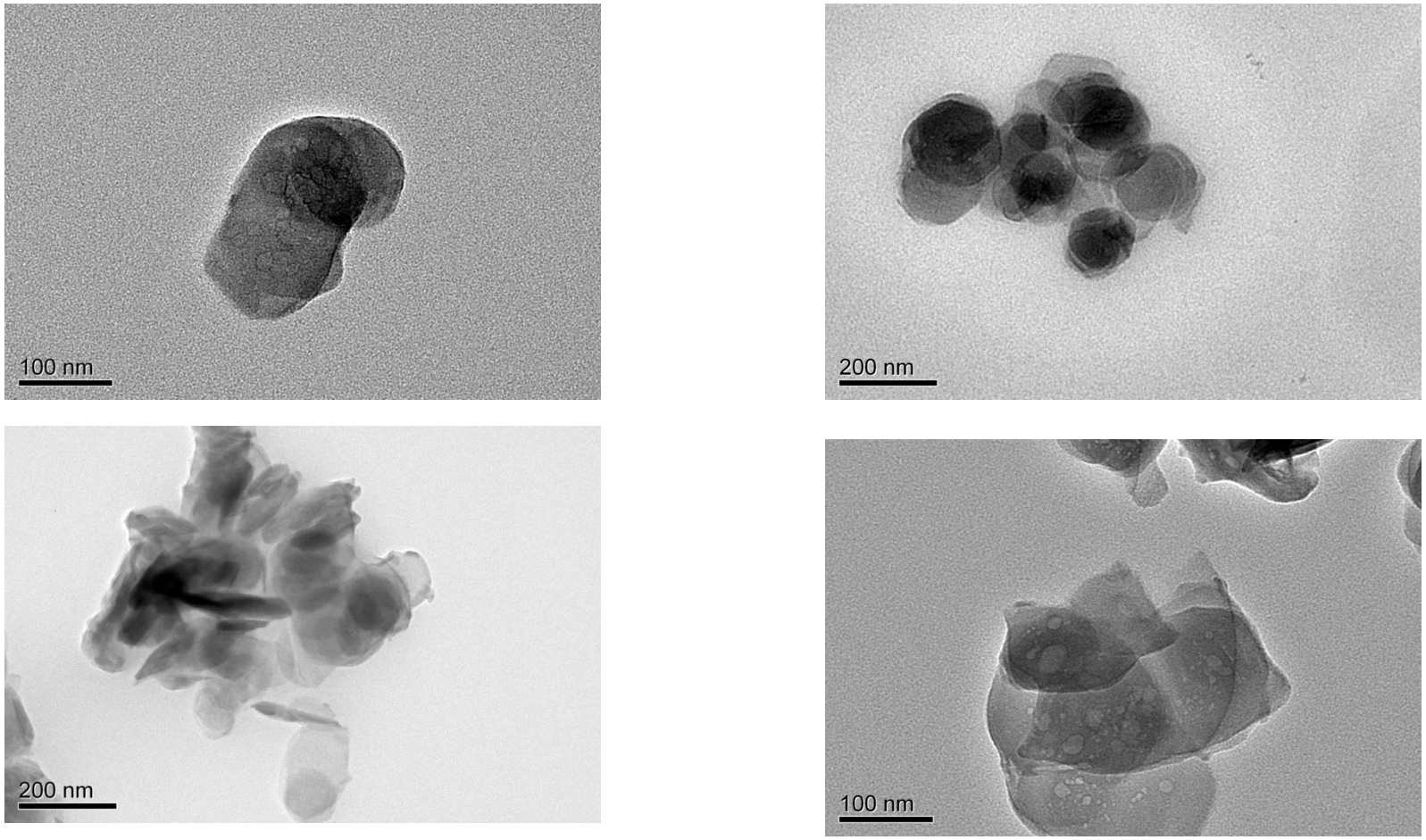

Figure III-4: TEM images of TEPI modified α-ZrP (~150 nm)

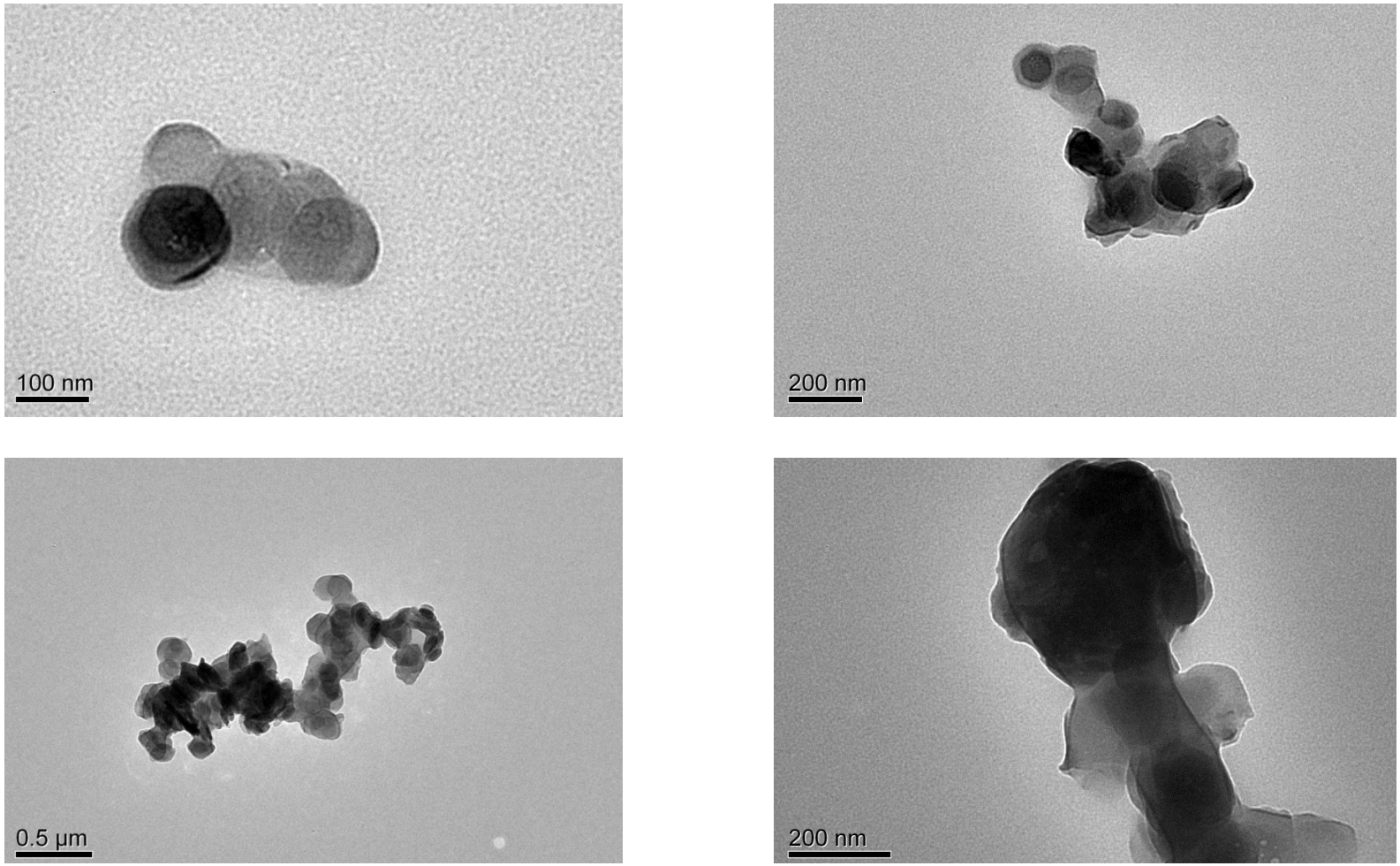

Figure III-5: TEM images of DCMPS modified α-ZrP (~150 nm)

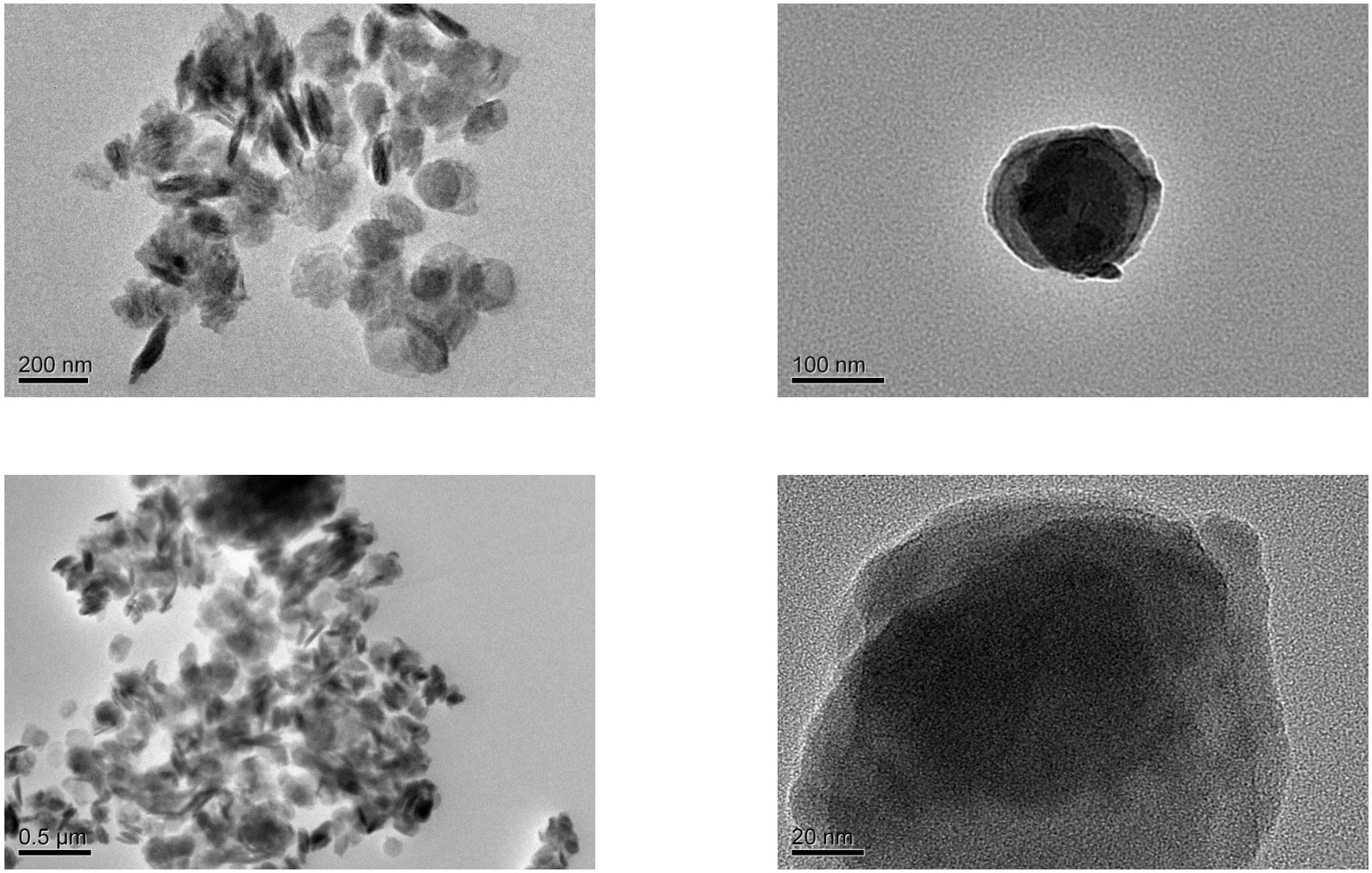

Figure III-6: TEM images of LMA modified α-ZrP (~150 nm)

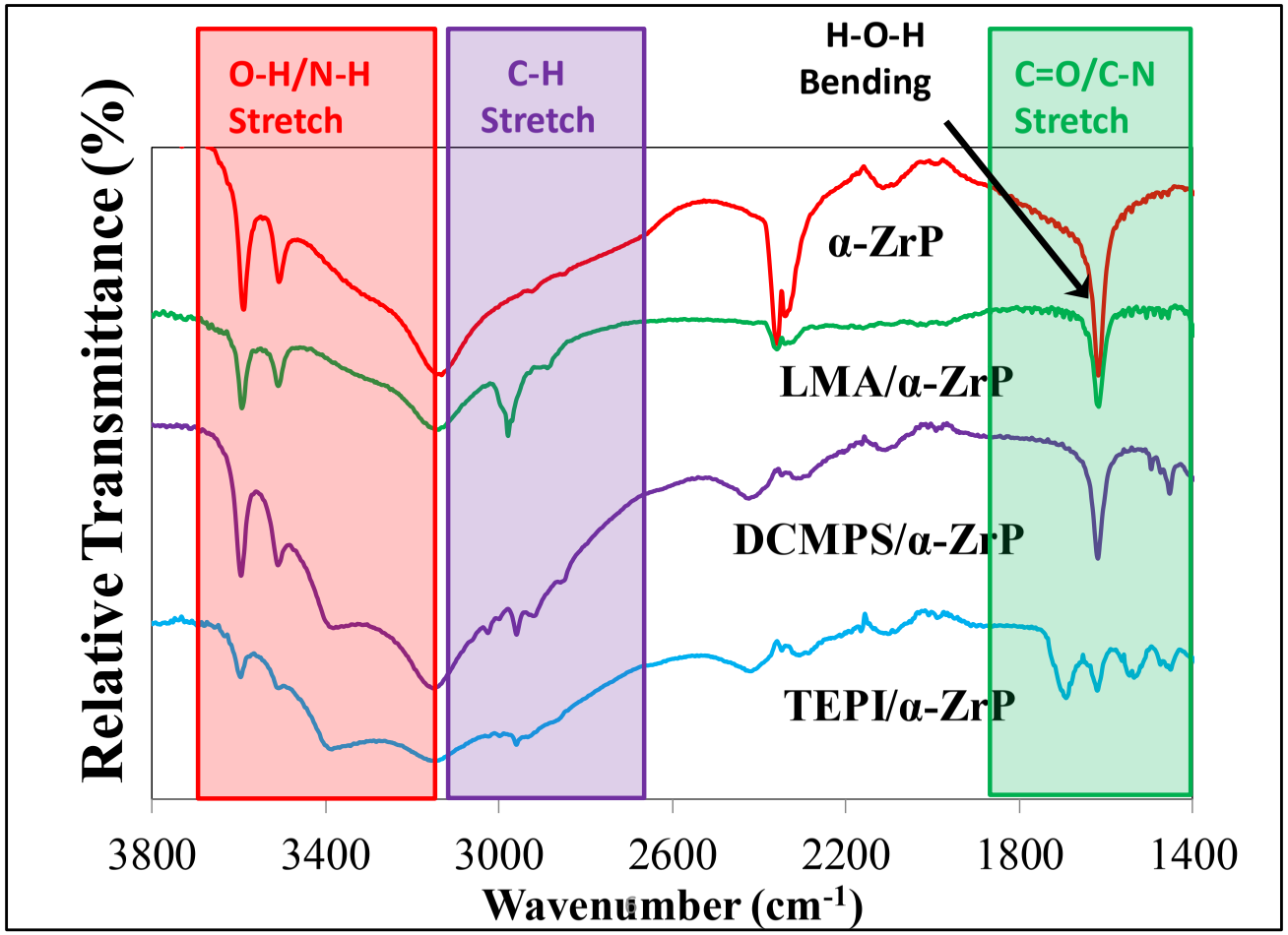

Figure III-7: FTIR of ZrP before (red) and after surface modification with TEPI(blue), DCMPS(violet), LMA(green).

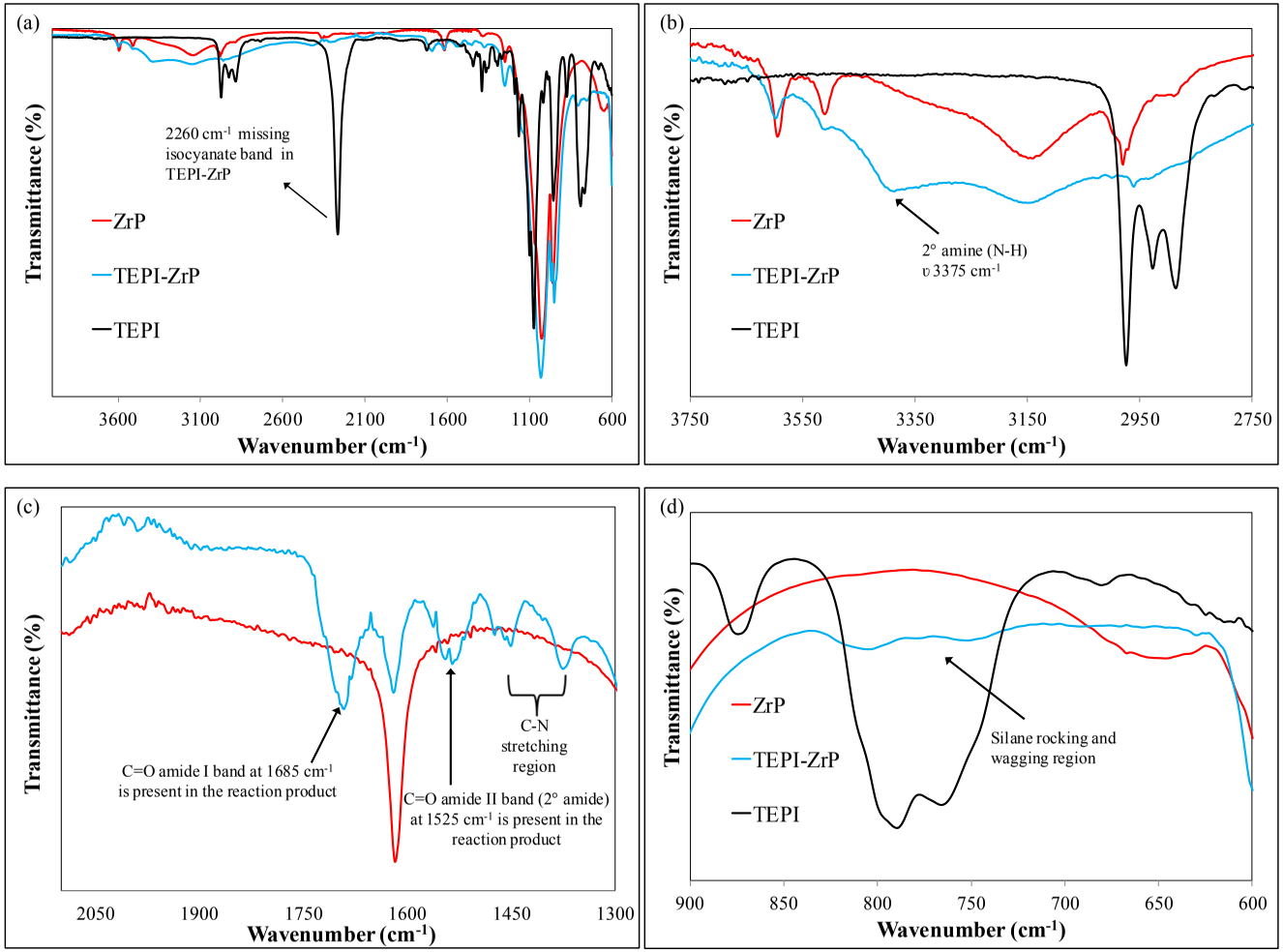

Figure III-8: (a), (b), (c) & (d) FTIR spectra of TEPI-ZrP.

The C=O amide band appears at 1685 cm^{-1} (Figure III-8c) in the reaction product and the secondary amide band at 1525 cm^{-1}. The silane rocking and wagging also appears between 750 and 800 $cm^{-1.}$ (Figure III-8d).In the DCMPS/ α-ZrP the appearance of the silane rocking and wagging stretches between 750 and 850 cm^{-1} in the reaction product indicate modification (Figure III-9a). The appearance of the stretches between 1700-1500 cm-1 indicate the addition of aromatic C=C bending onto the modified ZrP product (Figure III-9b).

For LMA/ α-ZrP the emergence of the $–CH_2$ stretching absorbance at 2900 cm^{-1} points to the possible addition of LMA onto the surface.[166] The disappearance of the carbonyl peak between 1705-1730 cm^{-1} (Figure III-10b) indicates a possible bonding site for the LMA onto the surface P-OH groups and the possible polymerization onto the ZrP surface to form PLMA. The absence of the peak in the reaction product also indicates a lack of free or unassociated carbonyls. The other FTIR resonance at the lower frequency (roughly at 1710 cm^{-1}) was from the carbonyl groups that were bound to the ZrP surface.[166] It was discovered experimentally that the relative intensities of bound carbonyl compared with the free carbonyls decreases with an increase in the adsorbed amount of LMA hence the 7:1 molar ratio for LMA/ZrP was settled upon.

The TGA for each surface modified material and its characteristic weight loss is elucidated (Figure III-11) and the overall extent of modification is estimated in each case in Table III-1. The TGA of all three modified materials shows an increase in the weight loss as compared with the pristine α-ZrP which has a typical weight loss of ca. 12%.[3] The first weight loss observed can be attributed to the loss in surface and intercalated

water molecules at ca. 120 °C. The next major weight loss is observed at ca. 540 °C and can be attributed to the formation of the pyrolysis product ZrP_2O_7.

The TGA for the TEPI /α-ZrP shows a weight loss of 17.3 %, DCMPS/ α-ZrP a weight loss of 14.2% and for LMA/ α-ZrP a weight loss of 19.51% with the appearance of additional weight loss points. In all cases the first weight loss at can be attributed to the cleaning solvents and surface moisture. The next weight loss at ca. 135 °C can be attributed to the loss of the intercalated water within the lattice structure for each of the materials. Due to the modifiers, accessing this water becomes harder hence why the temperature is higher in the modified compounds vs. the pristine ZrP in each of the three cases. Additionally, due to the varied lengths of the attached aliphatic chains and differences in individual functional groups in each of the three cases the next weight loss occurs between 250-425 °C. The final weight loss takes place ca. 525 °C and is attributed to the formation of the zirconium pyrophosphate due to the condensation of the phosphate groups. It is interesting to note that the LMA which we suspect is actually forming PLMA onto the α-ZrP surface reveals the biggest weight loss compared to the other two modifiers. This last weight loss attributed to the condensation of the phosphate groups is decreased by 15 °C when compared to that of the pristine α-ZrP, probably because of the pyrolysis of the aliphatic chains causing damage to the crystal structure of the ZrP particles, allowing a faster thermo decomposition.[3]

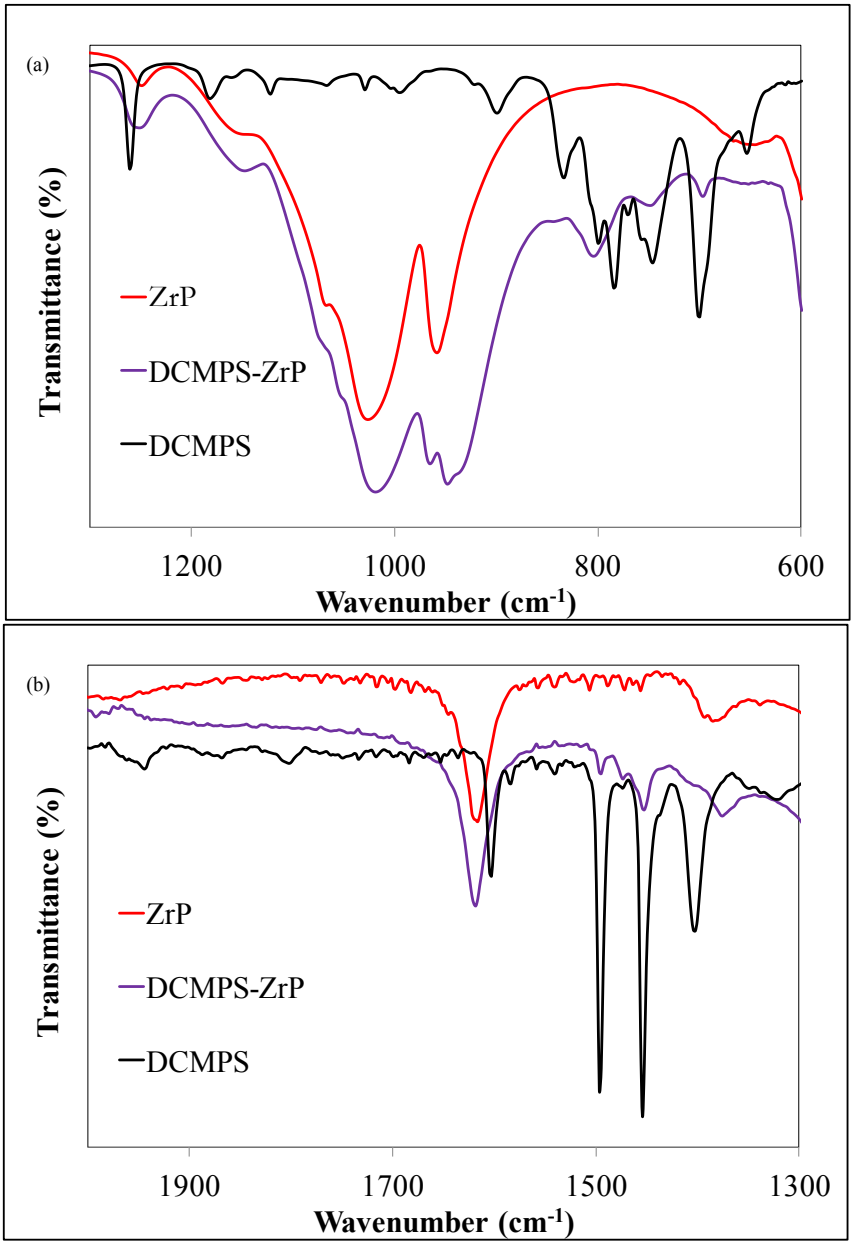

Figure III-9 (a) & (b) FTIR spectra of DCMPS-ZrP

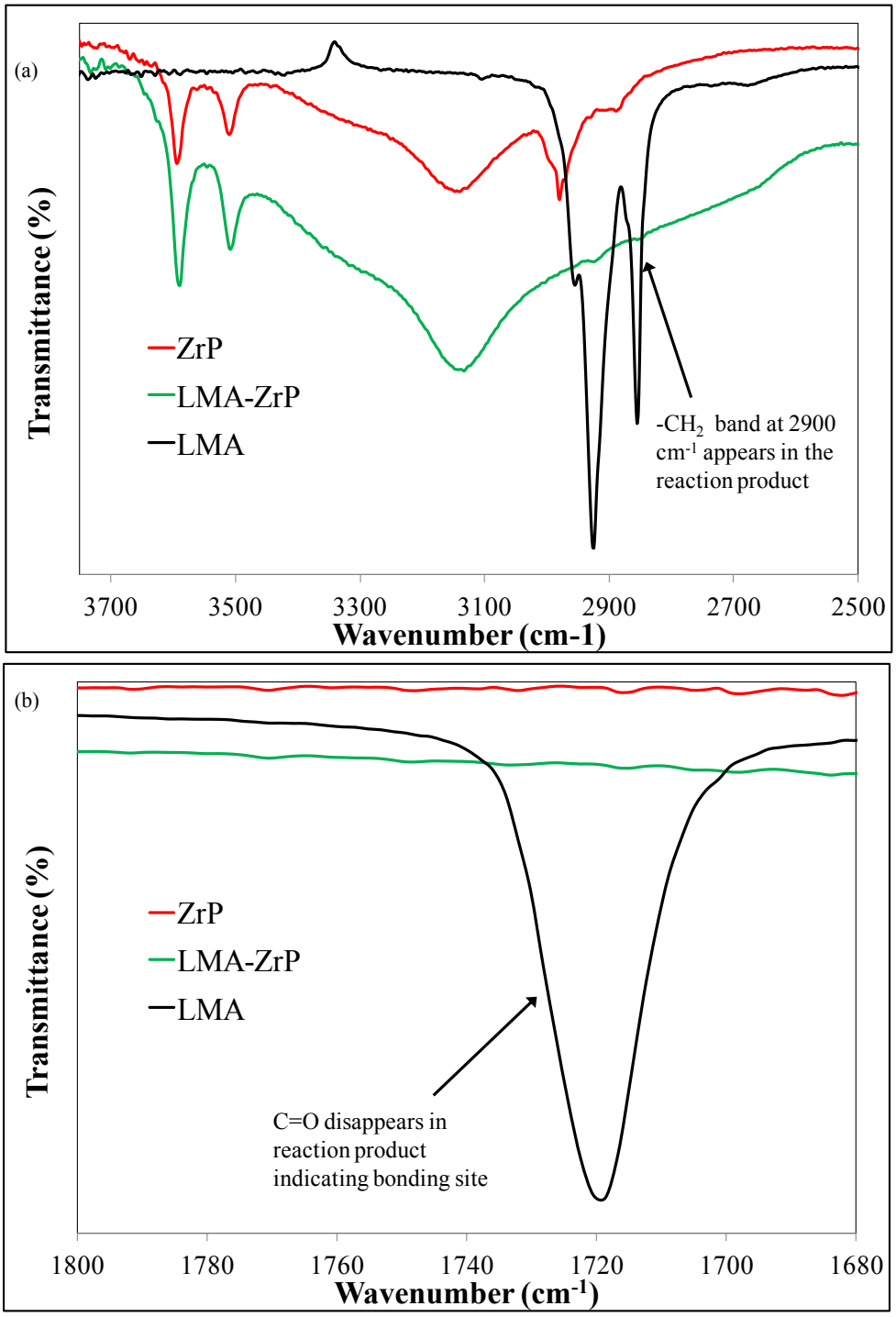

Figure III-10 (a) & (b) FTIR spectra of LMA-ZrP

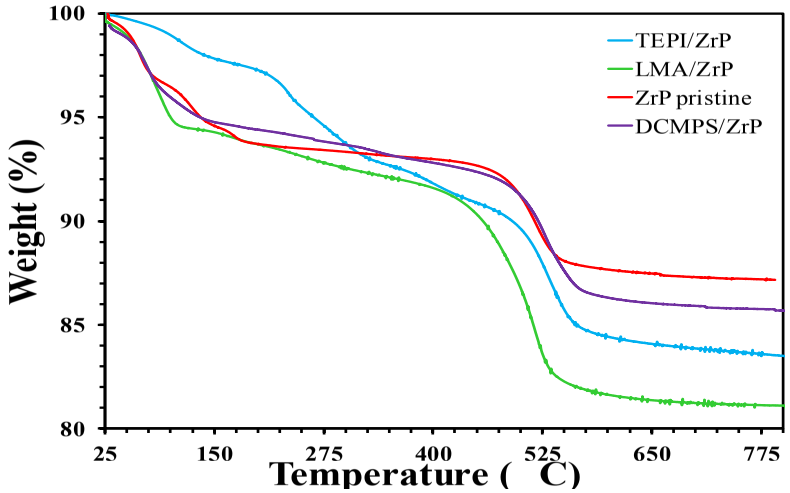

Figure III- 11: TGA analysis of ZrP before (red) and after surface modification with TEPI (blue), DCMPS (violet), LMA (green).

Sample	Total Wt Loss	End Product	Proposed Chemical Formula
ZrP pristine	12%	ZrP_2O_7	$Zr(HPO_4)_2.H_2O$
TEPI-ZrP*	17.25%	$ZrP_2O_7 + SiO_2$	$Zr(H_{0.88}PO_4)_2(TEPI)_{0.24}.0.93H_2O$
DCMPS-ZrP*	14.23%	$ZrP_2O_7 + SiO_2$	$Zr(H_{0.94}PO_4)_2(DCMPS)_{0.12}.0.89H_2O$
LMA-ZrP	19.51%	ZrP_2O_7	$Zr(H_{0.88}PO_4)_2(LMA)_{0.12}.0.82H_2O$

Table III- 1: Proposed chemical formula for the surface modified α-ZrP. * Indicated chemical formula calculated using both TGA & ICP-MS results.

The surface modification for the ZrP nanoplatelets were monitored by the substitution of the surface phosphate groups and further confirmed by microprobe quantitative compositional analyses (Figure III-11& III-12) and ICP-MS (Table III-2). The amount of silicon in the surface modified products can be easily monitored in the case of both TEPI-ZrP and DCMPS-ZrP. Since LMA doesn't offer any easily identifiable species it wasn't analyzed using microprobe or ICP-MS analysis.

Event-by-event cluster SIMS was performed on each of the surface modified samples to probe the effective surface coverage and to determine both qualitatively and quantitatively if a chemical modification event was occurring. A quantitative estimate of surface coverage of modifier (TEPI,DCMPS or LMA) containing molecules was calculated for each sample by using the coincidence counting technique by comparing the signals attributed to modifier m/z indicated in the respective mass spectra in color (Figures III-13,14 & 15), corresponding to each respective modifier anion, and m/z = 79 or 63, corresponding to PO_3^- or PO_2^- anion, with the signal of "coincidentally emitted/detected" surface modifier and PO_3^- or PO_2^- anions.167 A quantitative estimate of TEPI, DCMPS & LMA surface coverage was calculated,167 following eqn(1) and (2), where it was determined that the TEPI coverage is 45.2% ± 2.8%, DCMPS coverage is 20.85% + 2.3% and LMA coverage is 94.9% + 2.5%.

$$N_E = \frac{Area_{Coincidental\ emission}}{Area_{\ Modifier\ anion}\ X\ Area_{\ ZrP\ anion}} \qquad \textbf{Eq III-2}$$

$$Coverage = \frac{N_E}{N_O} \qquad \textbf{Eq. III-3}$$

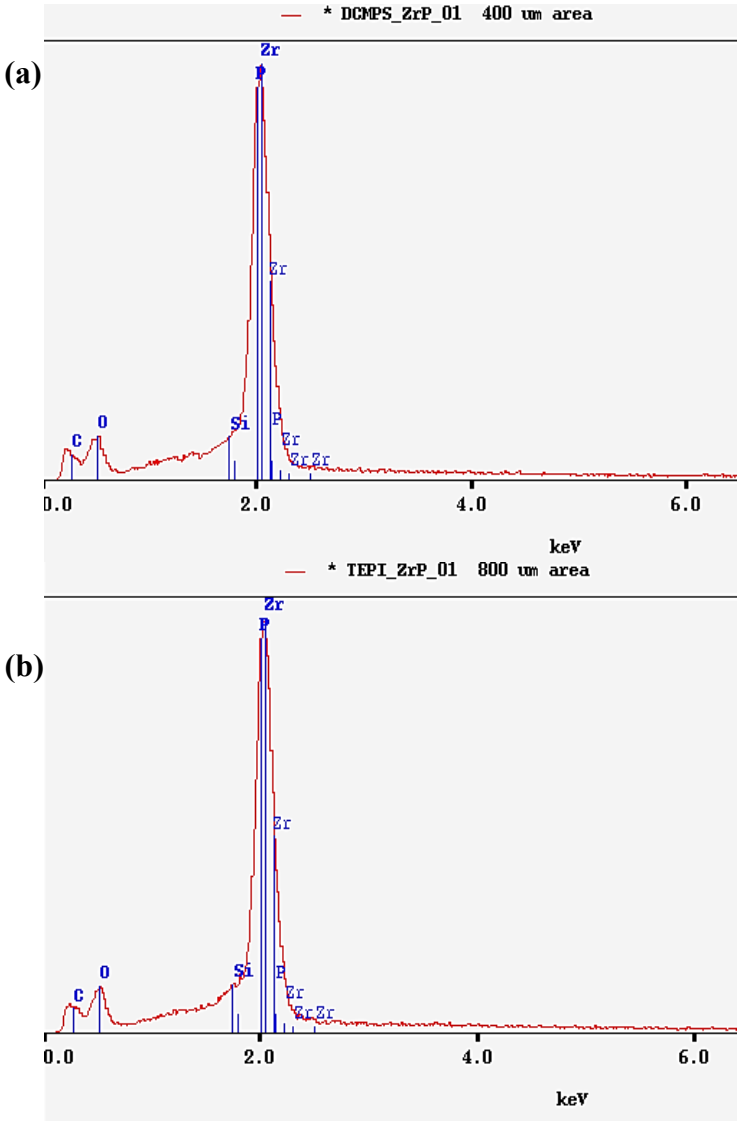

Figure III-12: Microprobe analysis X-Ray Spectrum of (a) DCMPS-ZrP (b) TEPI-ZrP from 800 μm area

Sample	P (ppm)	Si (ppm)	Zr (ppm)
DCMPS-ZrP	155	8.03	228
TEPI-ZrP	156	10.1	201

Table III-2: Elemental concentrations for surface modified ZrP nanoplatelets.

One benefit of using the event-by-event bombardment/detection mode is the ability to obtain more insight into specific impact/emission events. In order to obtain a representative mass spectrum for a given component of the system, the co-emission from that component may be displayed in a coincidence mass spectrum. For example, in order to obtain a representative mass spectrum from the modifier domain, all ions coemitted with Cl^- are monitored for the DCMPS modified α-ZrP. Projectile impacts resulting in chloride emission also showed emission from hydrocarbon peaks and silicon oxide peaks. The most intense peak in the coincidence spectrum is m/z 77 SiO_3H^- (coincidence yield = $3.5x10^{-5}$), which implies that chloride-rich areas of the modified α-ZrP are less than 10 nm in thickness. In the previous chapters the equations for calculating surface coverage were briefly discussed. Calculating N_E gives the fraction of relevant modified ions and compares that with N_o which is the total number of projectile events.

Subsequently, the calculated experimental coverage for each of the surface modified ZrP were compared to their maximum theoretical coverage. For the TEPI-ZrP if the bonding occurs through the amino group it would be placed midway between the two P-OH groups and held in place by a hydrogen bond. The hydrogen bonding is (P)-O-H--N-H--O-H—N, etc.[168] This is similar to the hydrogen bonding in α-ZrP between the P-OH groups and water.[169] If all the possible P-OH sites on the ZrP plane were actively involved in covalent bonding the highest possible coverage due to the TEPI modifier would be 100/2 (bonded by both the amine group and the carbonyl group) which indicates an ideal surface coverage of 50%. Using SIMS we estimate the surface coverage for TEPI-ZrP is about 45.2% $\pm$ 2.8%. Similarly for the DCMPS-ZrP material

there are two available Cl^- groups which readily react with the available P-OH sites. The geometry and steric hindrance attributed to the methyl and phenyl groups the possible third occupation site is blocked effectively thus resulting in a tripod occupation. Additionally it is also possible to have Si-O-Si type bridging on the surface indicating only every other surface P-OH is modified successfully. While SIMS provides a pretty good estimation of surface coverage quality, the bonding information is insufficient for conclusive evidence. In this case the ideal coverage would be about 33.33% and using SIMS surface coverage estimation the coverage is found to be 28.05%$\pm$2.3%.

NMR Results Discussion

TEPI / ZrP

The $^{31}P(^{1}H)$ MAS NMR spectrum (**Figure III-16**) recorded at direct excitation shows the phosphorus pattern (-18.2, -20.2 and -21.6 ppm) typical of the ZrP matrix and a very low intense shoulder at -30.3 ppm, which can be well assigned to the surface phosphorus in the groups P-O-C(O)NH. In fact, the relative intensity of this line decreases in the $^{31}P(^{1}H)$ CP MAS NMR spectrum. In accordance with the structure, the ^{13}C (^{1}H) CP MAS NMR spectrum of the compound exhibits six groups of resonances expected for the organic part: -1.5, 11.0, 21.6, 41.4, 61.4 and 156. 4 ppm (**Figure III-17**) assigned to ***C***H_2Si, ***C***H_3CH_2, ***C***H_2-NH, ***C***H_2O and ***C***(O)NH carbons. The appearance of the three resonances centered at 156.4 ppm can be explained by different local environments of the ***C***(O)NH carbons on the matrix surface.

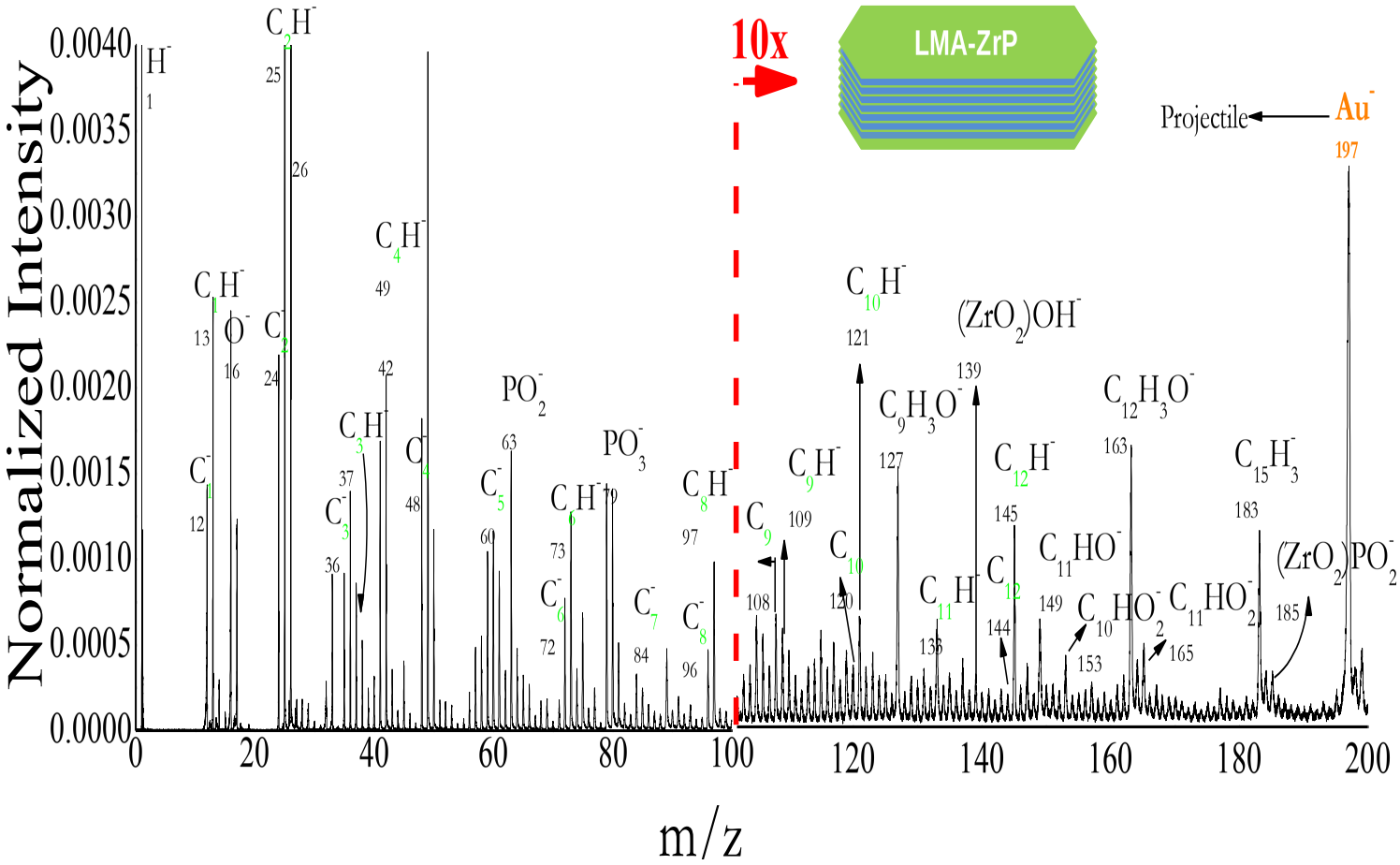

Figure III-13: Secondary ion mass spectrum of α-ZrP modified with LMA analyzed with 50 Kev Au_{400}^{4+} projectiles. The y-axis is normalized to the total number of projectile events. The modifier fragments are indicated above (in green).

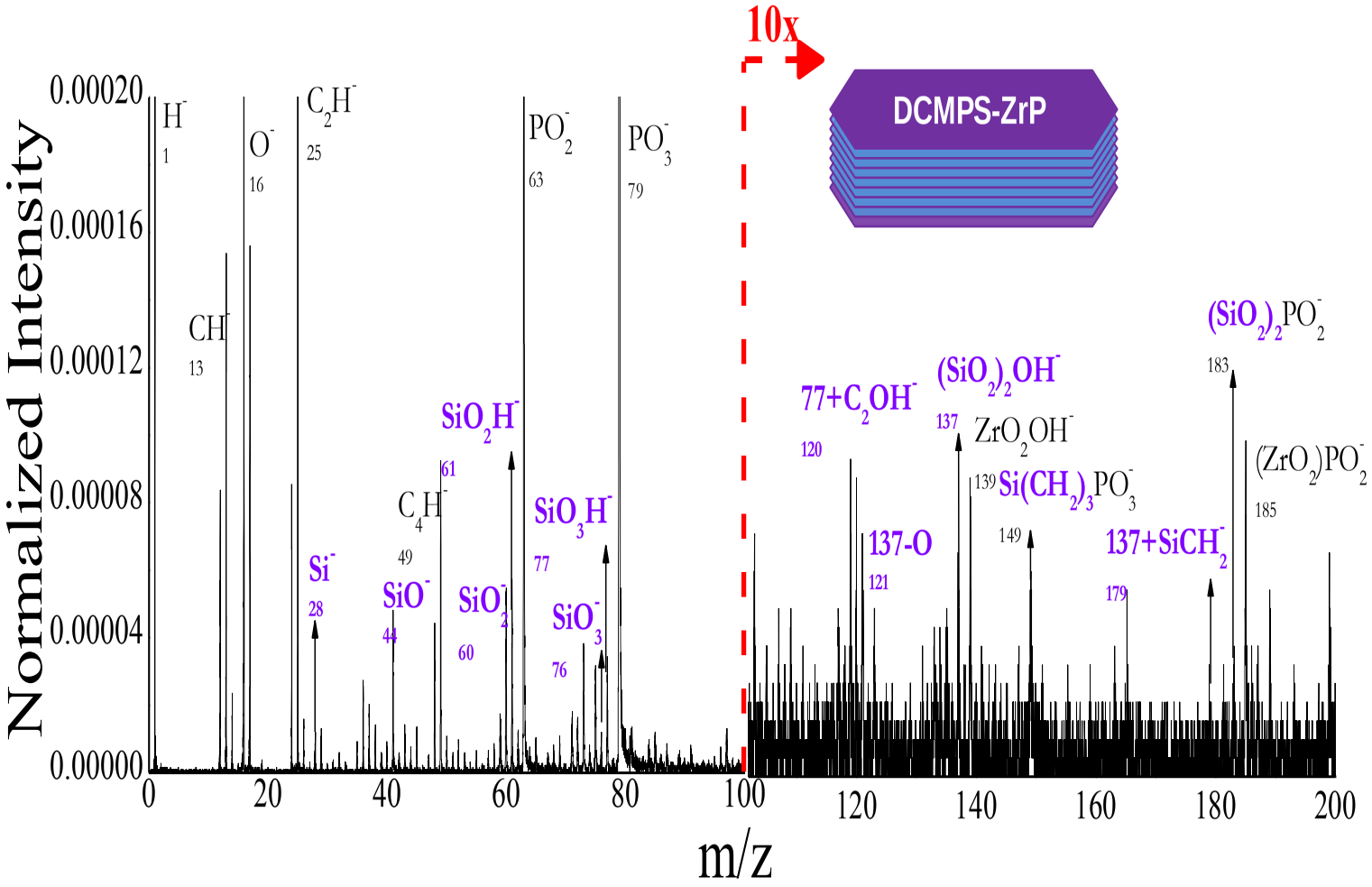

Figure III-14: Secondary ion mass spectrum of α-ZrP modified with DCMPS analyzed with 26 KeV C_{60}^{+} projectiles. The y-axis is normalized to the total number of projectile events. The modifier fragments are indicated above (in violet).

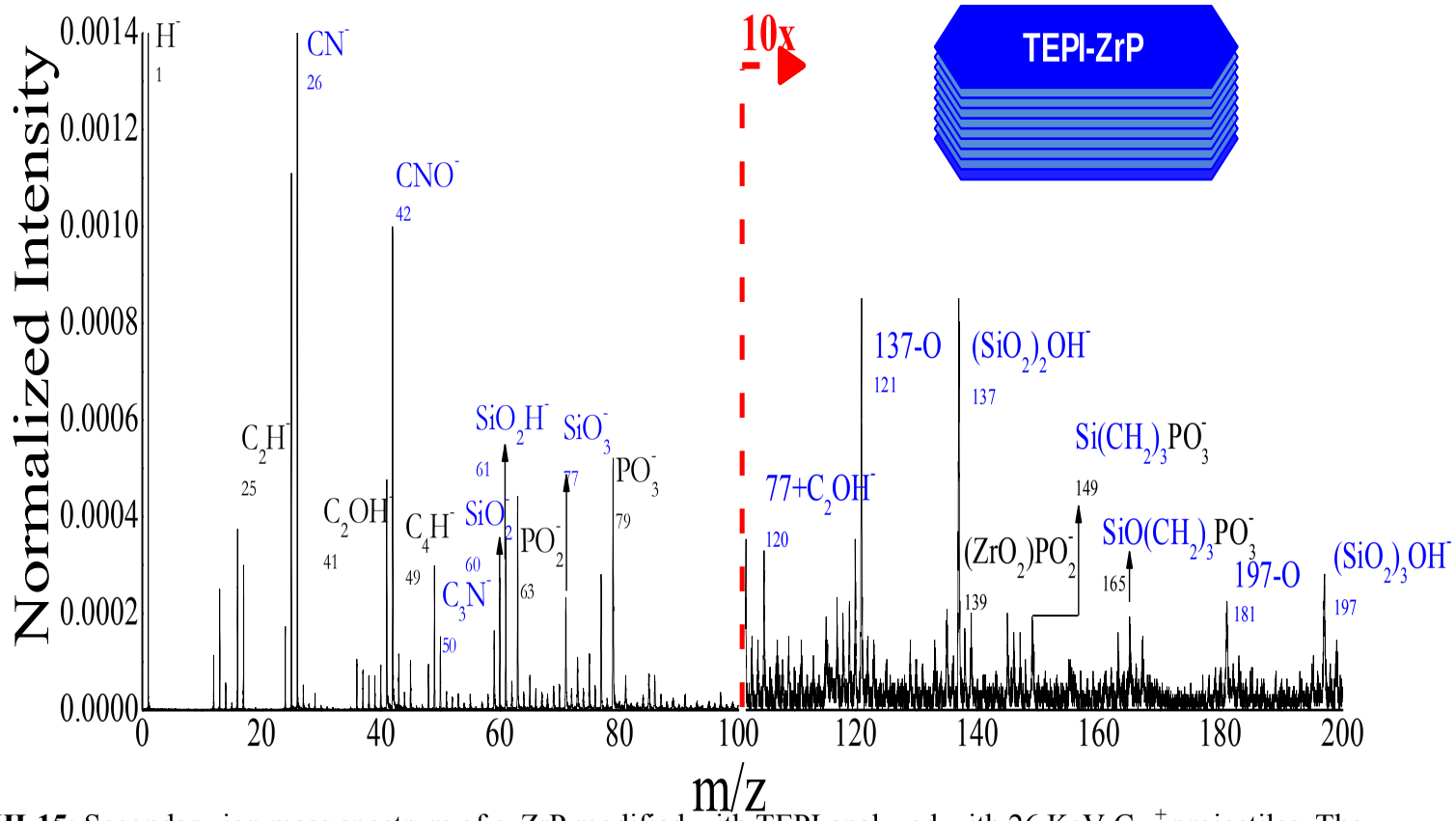

Figure III-15: Secondary ion mass spectrum of α-ZrP modified with TEPI analyzed with 26 KeV C_{60}^{+} projectiles. The y-axis is normalized to the total number of projectile events. The modifier fragments are indicated above (in blue).

Finally, the proposed structure is supported by the ^{29}Si (^{1}H) CP MAS NMR spectrum where the group of the resonances at -56.2 - - 67.5 ppm is observed (**Figure III-18**).

DCMPS / ZrP

The $^{31}P(^{1}H)$ MAS NMR spectrum of this compound is very similar to that in **Figure III-16** to show again the phosphorus ZrP matrix pattern and a very low intense shoulder at -29.7 ppm assigned to the surface phosphorus in the groups P-O-Si. Again the relative intensity of this shoulder reduces in the $^{31}P(^{1}H)$ CP MAS NMR spectrum supporting the assignment. **Figure III-19** shows the ^{13}C (^{1}H) CP MAS NMR spectrum where the signals at -5.4 and 131.6 and 125. 9 ppm corresponds to the $CH_3Si(O_2)C_6H_5$ structural units on the surface (the broad line is coming from the NMR probe). The two lines at 60.9 and 15.2 ppm belongs probably to ethanol located in the pores.

The ^{29}Si (^{1}H) CP MAS NMR spectrum shows two sharp resonances at -28.2 and 34.9 ppm (**Figure III-20**) again in accordance with the structure.

LMA / ZrP

The $^{31}P(^{1}H)$ MAS NMR spectrum of this compound shows the phosphorous ZrP matrix pattern and a very low intense shoulder located now at -23.1 ppm. The line can be assigned to the surface phosphorous in the groups P-O-CH_2. The latter is supported by decreasing the relative intensity of the shoulder in the $^{31}P(^{1}H)$ CP MAS NMR spectrum. In spite of the very large number of scans, the signal/noise ratio in the ^{13}C (^{1}H) CP MAS NMR spectrum of this compound is poor (**Figure III-21**).

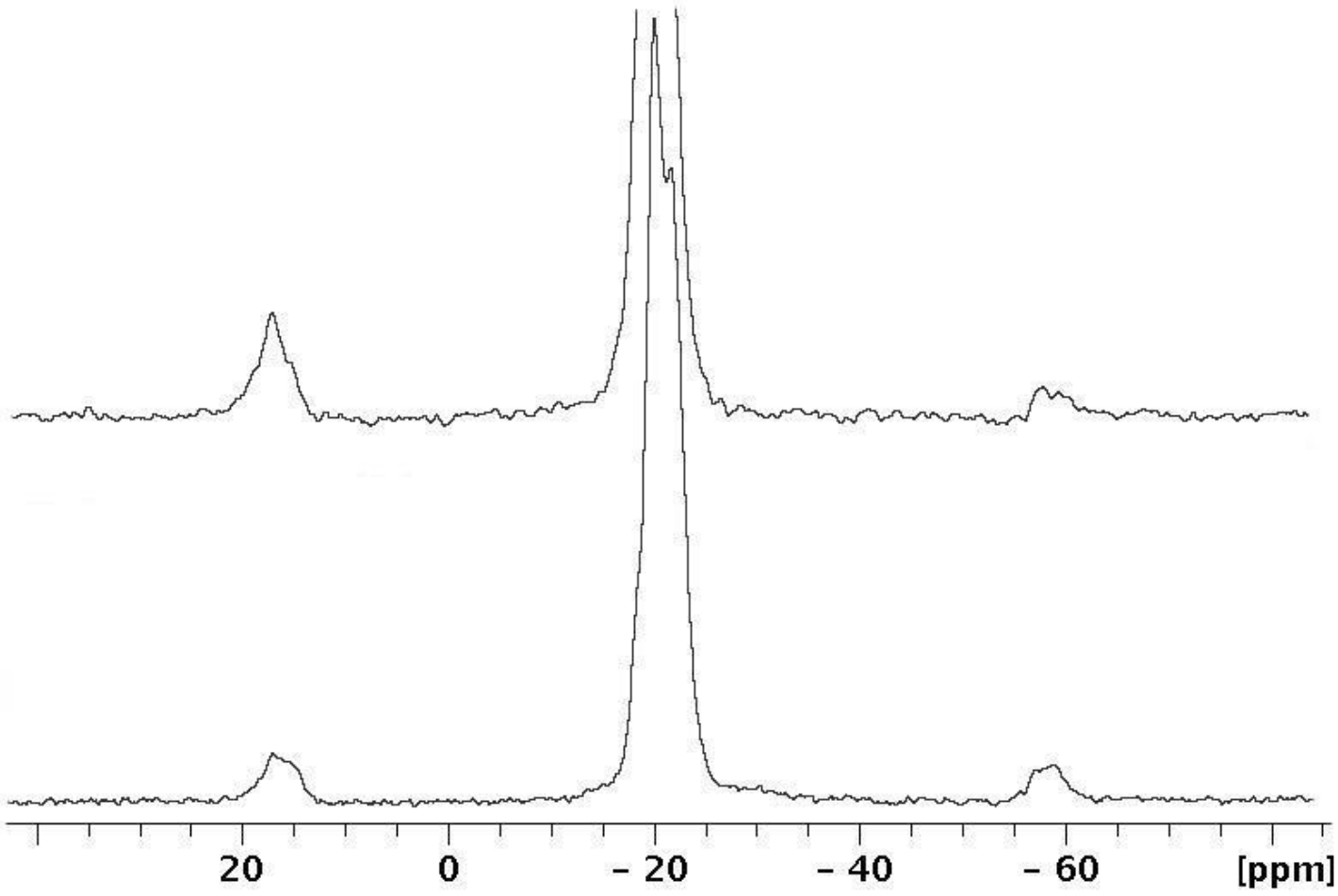

Figure III – 16: The $^{31}P(^{1}H)$ MAS NMR spectrum (bottom) and the $^{31}P(^{1}H)$ CP MAS NMR spectrum (top) recorded at spinning rate of 6 kHz for compound **TEPI / ZrP.**

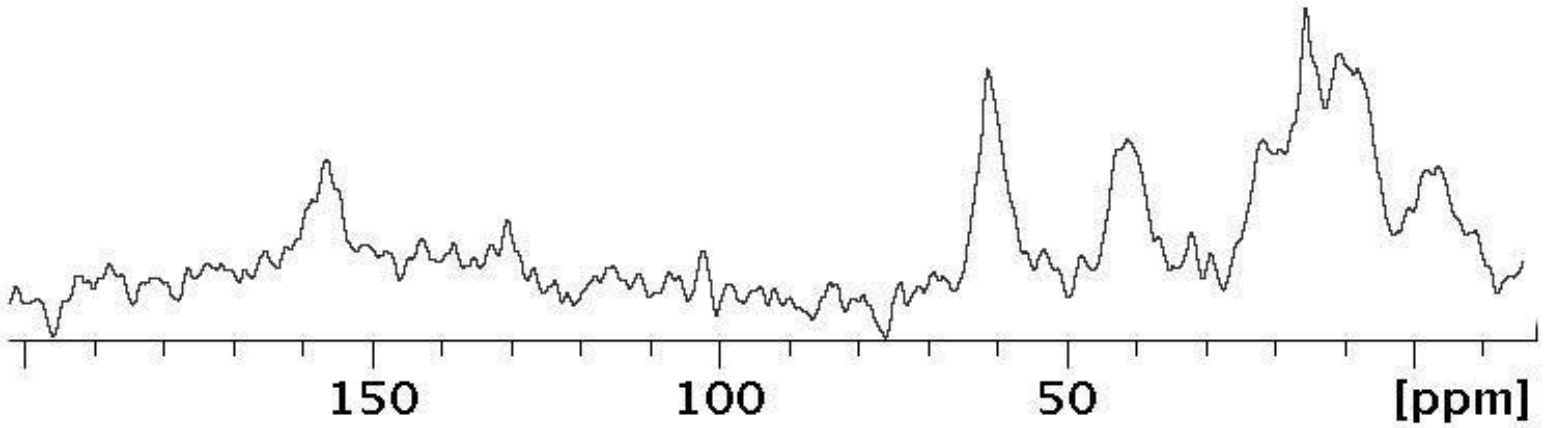

Figure III – 17: The ^{13}C (^{1}H) CP MAS NMR spectrum of compound **TEPI / ZrP** recorded at spinning rate of 6 kHz.

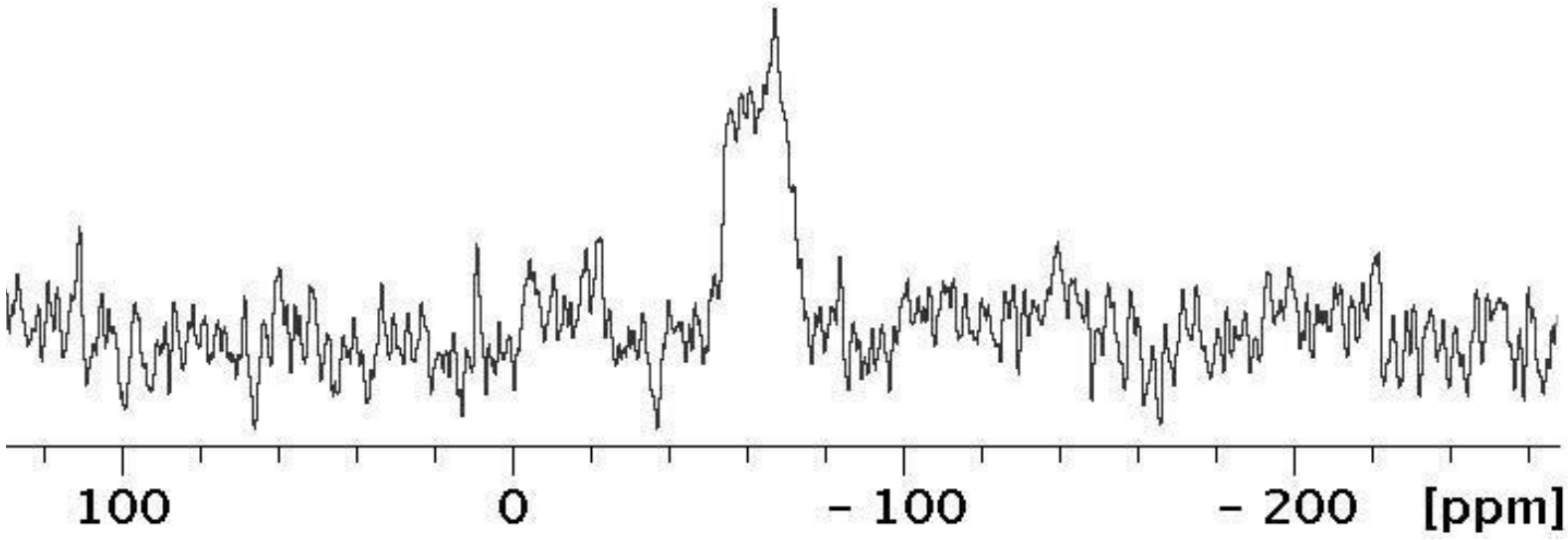

Figure III – 18: The $^{29}Si(^{1}H)$ CP MAS NMR spectrum of compound **TEPI / ZrP** recorded at spinning rate of 6 kHz.

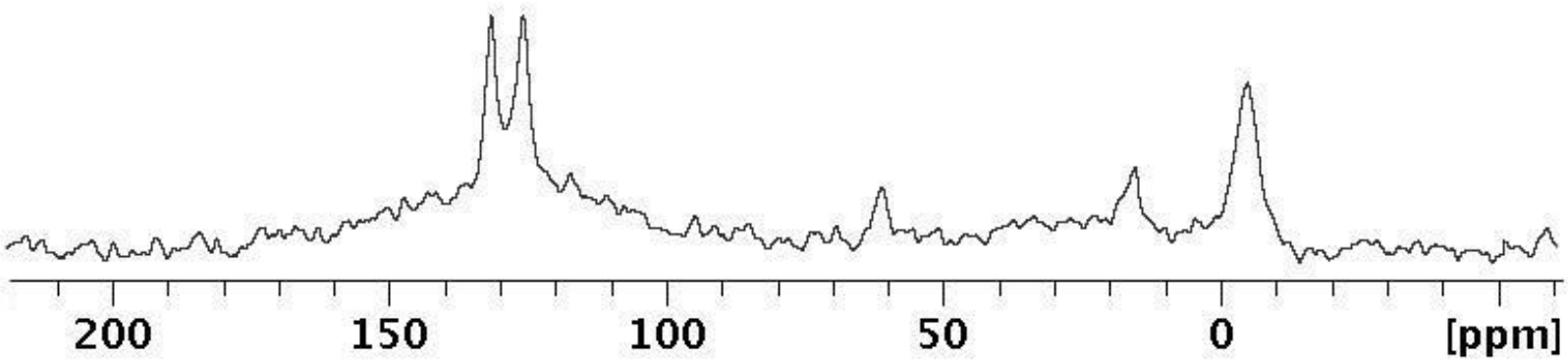

Figure III – 19: The ^{13}C (^{1}H) CP MAS NMR spectrum of compound **DCMPS / ZrP** recorded at spinning rate of 10 kHz.

Nevertheless the resonances cantered at 62.3, 28.2 and 15.9 ppm can correspond to the aliphatic carbons in accordance with the expected structure. In addition, a very weal resonance at 166 ppm can belong to the carbonyl carbon R-O-C=O(CH)(CH_2-O-P)(CH_3).

Conclusion

In conclusion, we have demonstrated the successful fabrication of surface modified α- ZrP crystals grafted with TEPI, DCMPS & LMA. Their chemical structures were confirmed via TGA, FTIR, solid state NMR and SIMS measurements. TEPI, DCMPS and LMA are powerful functionalization agents used to initiate the surface reaction of α-ZrP. We anticipate this introduces a new possible platform for further surface functionalization studies that may lead to a variety of applications. We also showed for the first time that SIMS in the event-by-event bombardment mode can be used to quantify the degree of surface modification in ZrP nanoplatelets SIMS also revealed possible surface polymerization for the LMA modified crystals and could potentially be applied in nano-composite quality determinations The established protocol could also quite easily translate to other inorganic materials such as TiO_2 nano-sheets in determining the quality of surface coverage for nano-domain analysis. These reactions can delineate the path for useful new applications in building versatile and flexible "smart" platform for surface studies.

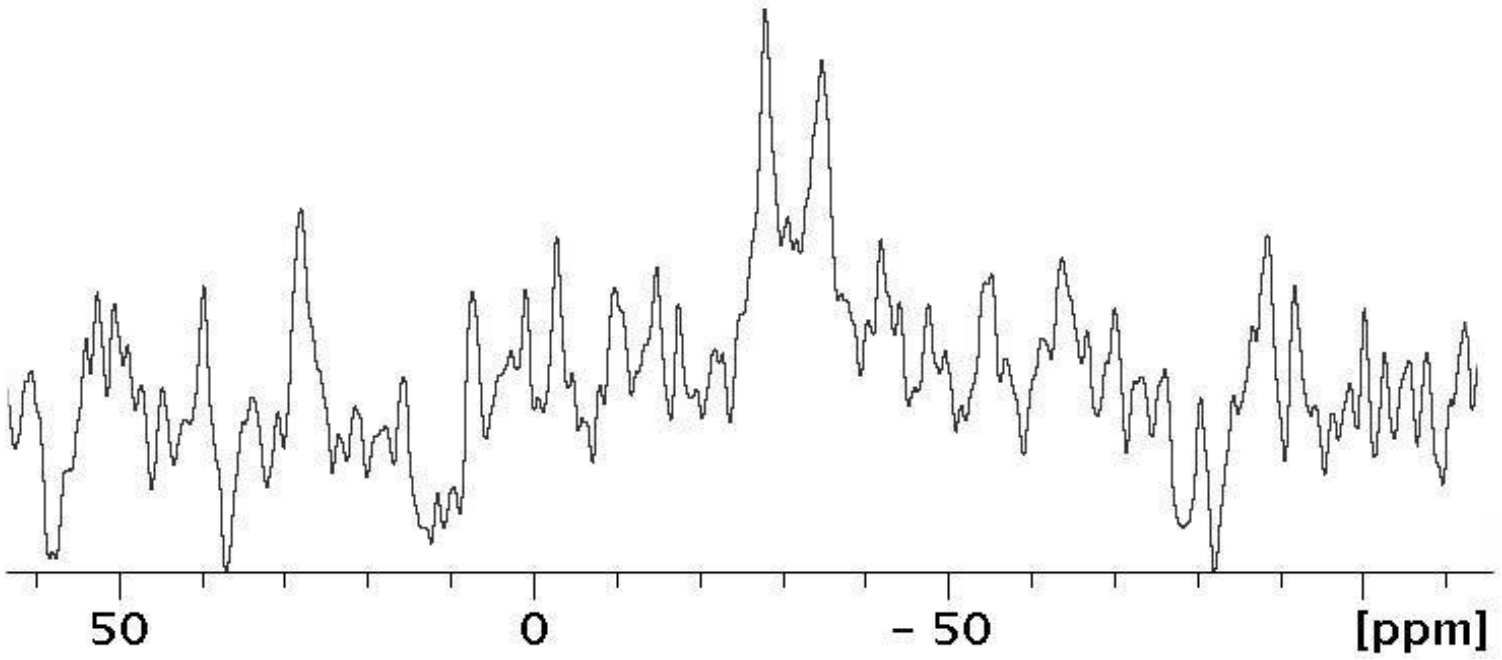

Figure III – 20: The ^{29}Si (^{1}H) CP MAS NMR spectrum of compound **DCMPS / ZrP** recorded at spinning rate of 6 kHz.

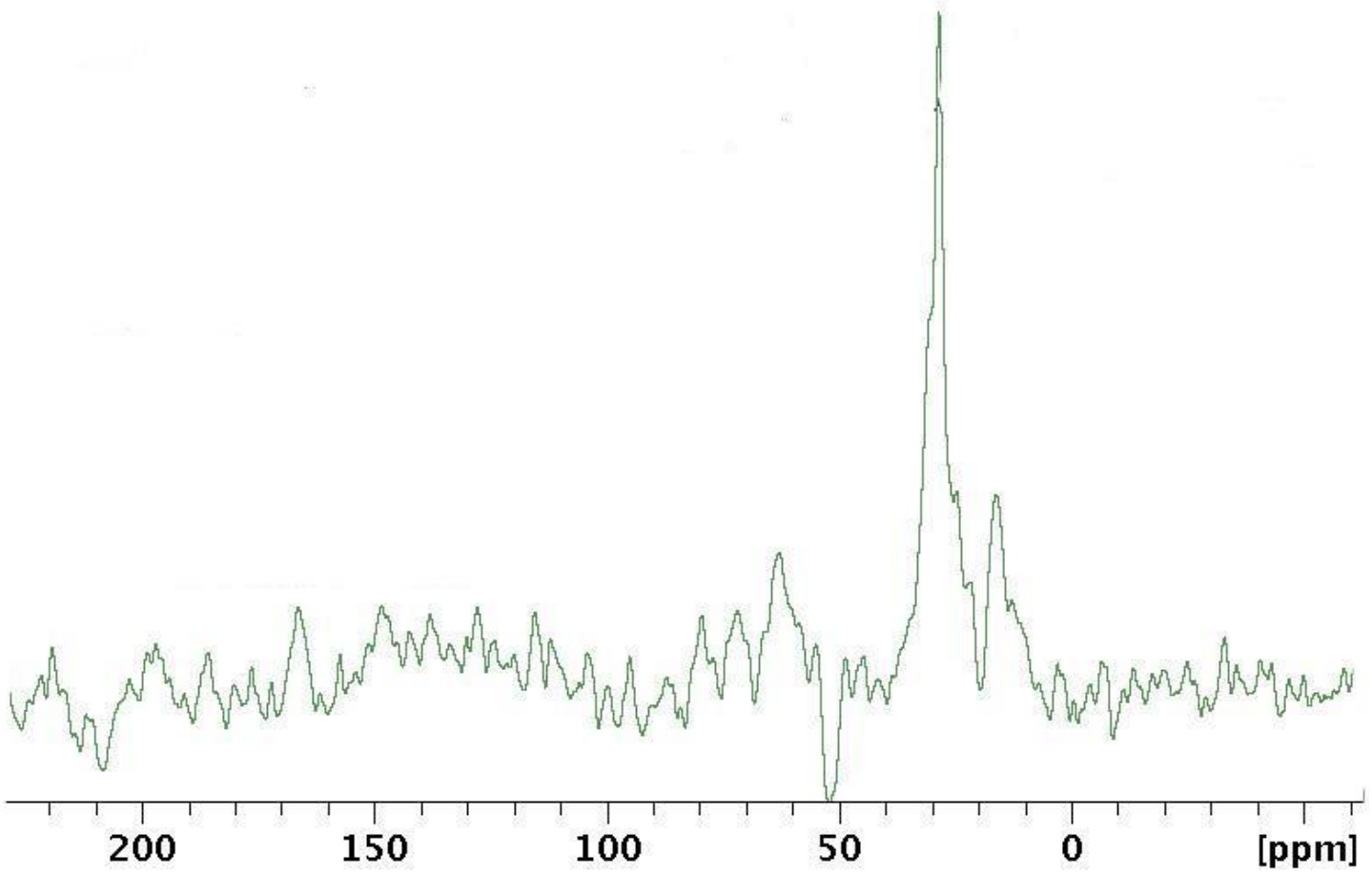

Figure III – 21: The ^{13}C (^{1}H) CP MAS NMR spectrum of compound **LMA / ZrP** recorded at spinning rate of 10

CHAPTER IV

TOF-SIMS HOMOGENEITY CHARACTERIZATION OF INORGANIC LAYERED NANOMATERIALS (ILNs) IN DRUG DELIVERY SYSTEMS

Introduction

There is a general consensus the characterization of morphologies in the nanometric scale needs to be improved.[16, 17] Intercalated nanomaterials pose the challenge of determining the effectiveness of intercalation, i.e. of characterizing materials that are likely heterogeneous. When considering nano sized materials there is the additional challenge arising from the complexity in accessing their physicochemical information in the nanometric domain. The intercalation chemistry of inorganic layered nanomaterials (ILN, such as metal phosphates and phosphonates, layered double hydroxides, clay materials, etc.) has been extensively studied.[170] The practical applications of these materials are a subject of widespread study in today's materials sciences and often require functionalization in order to improve their applicability.

We selected a model inorganic layered nanomaterial, the theta phase of zirconium phosphate, $Zr(O_3POH)_2 \cdot 6H_2O$, referred to as θ-ZrP. The structure of α-ZrP has a layered configuration in which the Zr ions are slightly above and below the mean plane of the layer. Three of the monohydrogen phosphate oxygen atoms bond to three adjacent Zr ions with phosphate groups alternating above and below the plane. The

remaining OH groups form a bilayer in the interlamellar space (**Figure IV-1a**). The theta phase has similar characteristics, except instead of only one molecule of water there are six in the theta phase. The ZrP particles are clay–like in that the hexacoordinated zirconium ions are sandwiched between outer layers of tetrahedral monohydrogen phosphate groups. ZrP has the ability to intercalate many species[171-177] and is also readily exfoliated.[178] The surface consists of parallelogram arrays of P-OH groups as was shown by complete displacement of the hydroxide protons on the surface phosphate by Cs^+ exchange.[179] The surface area could be predicted by the size of the Cs^+ ion and the number of protons liberated. These particles can be grown in sizes of less than 100 nm or as large crystals.[180]

The ease of synthesis, of crystallinity and size control has allowed for α-ZrP to be used as the model system for intercalation chemistry studies for over four decades.[148-151] It represents an ideal platform for intercalation reactions. The immobilization of organo and metal-based modifiers on a variety of solid supports remains crucial for many applications. The studies presented in this article discuss ~150 nm ZrP NPs and subsequently explore the use of SIMS from a fundamental approach for the purposes of nanomaterial characterization. It has been shown previously how SIMS can be applied to intercalated structures.[181, 182] The homogeneity parameter is of immense importance for the purposes of robust physicochemical characterization as it effects the bioavailability and hence the activity of the drug.

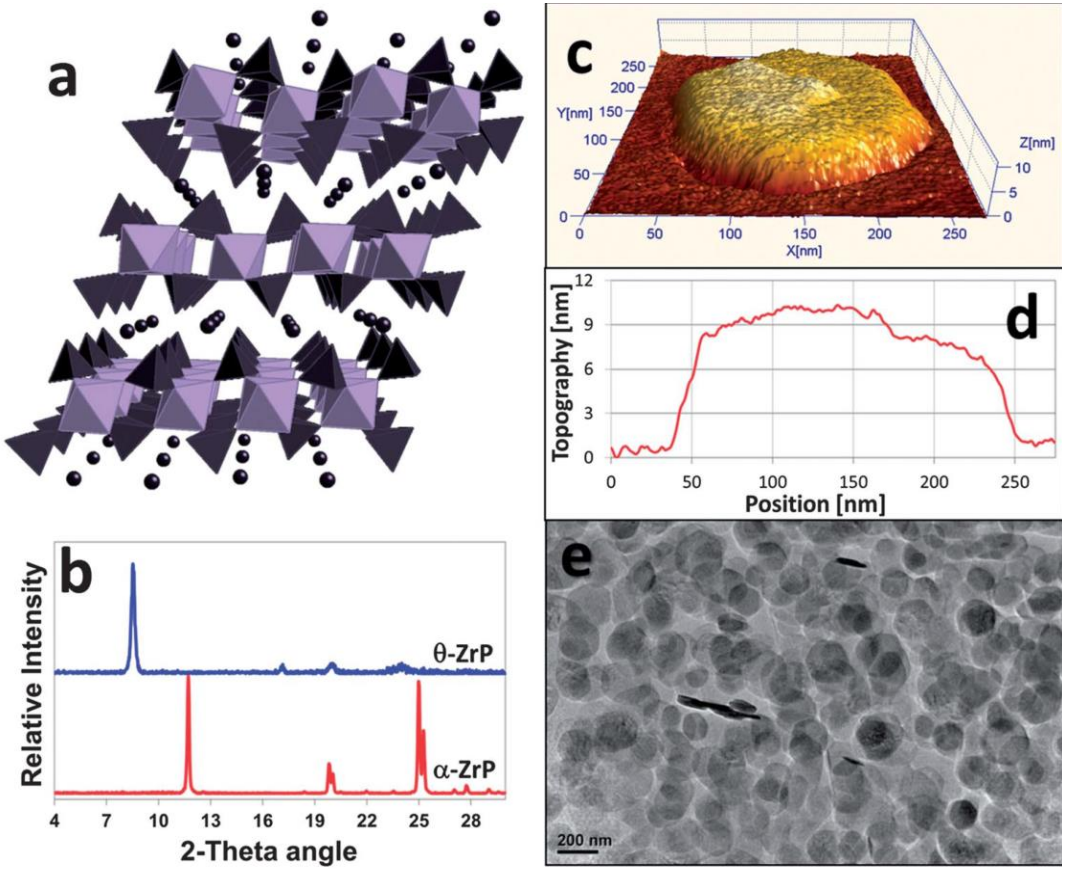

Figure IV-1: (a) Polyhedral representation of the alpha phase of zirconium phosphate [$Zr(HPO_4)_2.H_2O$] with phosphate tetrahedra in black, zirconium octahedra in light violet and the intercalated water molecules as violet spheres (hydrogen atoms are omitted for clarity). (b) X-ray powder diffraction pattern for the alpha (bottom) and theta (top) phases of zirconium phosphate. (c) AFM 3-D topography image of a single platelet of ZrP showing a particle diameter of ca. 187 nm. (d) Height profile for the ZrP nanoparticle in (c), showing a height of ca. 8.7 nm. (e) TEM image of ZrP nanoplatelets with an average diameter of 186 $\pm$ 39 nm, from vertex to vertex of the hexagon, and 160 $\pm$ 36 nm from edge to edge. (Image reprinted from reference 158)

In designing a controlled-release drug delivery system, the matrix must be easy to manufacture, be stable over an extended shelf life, and must deliver the appropriate drug dosage to the target area over the desired time period.[89] Nano sized drug delivery carriers had shown the advantage of higher accumulation in tumor tissues via the enhanced permeation and retention (EPR) effect defined by leaky vasculature and poor lymphatic drainage commonly seen in solid tumors.[183, 184] The superiority of ZrP materials over other ILN has been previously established: (1) not cytotoxic and not associated with any metabolic function;[10, 185] (2) solved crystal structures;[186, 187] (3) almost no impurities (<0.01%); (4) high ion exchange capacity of 6.64 meq. g^{-1} [39] to accommodate higher loading of drugs; (5) stability under biological conditions; (6) chemically modifiable surfaces;[150, 188] and (7) peculiar nano-platelet shape. The fabrication of drug delivery systems can be challenging due to the need for evaluation and analysis of the final product. One of the major advantages of these systems is their capacity to entrap high loads of bioactive species and protect their loads until they are released.[158] With drug delivery systems using nano vectors gaining in popularity, vetting the efficacy and design of these systems becomes essential. There has been an increase in uptake and delivery systems that are ion exchangers such as metal phosphate materials (which are cation exchangers), layered double hydroxides (LDH) or hydrotalcites (which are anion exchangers), and clays mineral materials as smectites and laponites, among many others. Additionally polymeric drug hybrids have also gained a lot of popularity.

Recently the potential of using layered structured nanomaterials (LSN) as non-viral vectors and drug carriers has been explored. [5,11, 158, 189-191] In the last several years

nanoparticle-mediated drug delivery has been studied as a novel and valuable means for overcoming the problem of significant side effects (due to lack of specificity) and the emergence of drug resistance. The fabrication of controlled release systems can be technically difficult compared with conventional dosage forms, the evaluation and analysis of the final product is vital. While the Trojan horse concept of delivering the drug through stealthy means is an interesting approach, in reality how much of the drug is actually incorporated into the matrix. In addition the location of the drug in the context of overall assembly is of utmost importance for the long term success/failure evaluations. In practice, dissolution studies have the capability to monitor the rate of drug release; however, any unwanted effects observed by these methods cannot be readily associated with specific defects in the structure or composition of the controlled-release system. An analytical technique is required that can probe the interior or probe cross sections of the assembly for the detection and distribution of various ingredients[91]. While it is important to recognize the benefits of molecular tagging an alternative method serving a parallel purpose may be developed utilizing the technique of SIMS. Traditionally polymeric drug delivery systems have been studied extensively using SIMS,[93, 182, 192] however the use of ILNs for biomedical applications is a relatively new field with little to no literature showing the SIMS studies of these new materials. In this paper we look at an ILN with a host of compatible anti-cancer drugs and evaluate their homogeneity side by side at various drug to substrate molar loading level ratios.

Experimental Methods

Materials

Zirconium(IV) oxychloride octahydrate ($ZrOCl_2 \cdot 8H_2O$), ethanol, acetone, cis-diamminedichloroplatinum(II), molybdocene dichloride and doxorubicin were obtained from Sigma-Aldrich while the titanocene dichloride, 99% was purchased from Acros Organics and used without further purification. Phosphoric acid (H_3PO_4) at 85% (v/v) (ACS grade reagent) was obtained from Fisher. Water was of nanopure quality from a Zyzatech reverse osmosis water system (18 MW/cm). All glassware was cleaned with Alconox from VWR and rinsed with abundant nanopure water. For sample deposition in SIMS and CAMECA ion microprobe analysis, customized Si wafers with 200nm thick metal layer of Au was used. The silicon wafers used were P(100) 10-20 ohm/cm cut down to 7x7 mm using a diamond knife and purchased from Silicon Valley Microelectronics.

Synthesis and Characterization

θ-ZrP was synthesized using a procedure reported by Kijima in 1982.[22] The procedure consists of slow drop wise addition of 200 mL of 0.05M zirconyl chloride ($ZrOCl_2$) solution to a preheated 200 mL solution of 6M H_3PO_4 at 94°C.The resulting solution is heated at 94°C for three days before the product is filtered and washed several times with water to obtain the θ-ZrP. In a typical procedure the intercalation process was performed by the batch method, adding the desired quantity of the drug (cisplatin,

titanocene, doxorubicin or molybdocene) to a water suspension of θ-ZrP ($Zr(O_3POH)_2 \cdot 6H_2O$) with interlayer spacing of 10.3 Å) at different molar ratios (loading levels).The complete details of sample preparation can be found elsewhere.[12a, 15] The complete characterization of the materials was performed using several analytical methods. The XRPD experiments were performed from 4° to 40° (2θ angle) using a D8 X-ray diffractometer system (Bruker AXS, Madison, WI) with a copper anode source ($K\alpha_1$, λ= 1.5418 Å) with a filtered flat LiF secondary beam monochromator for the ZrP:CisPt and ZrP:Dox samples. The divergence, receiver, and detector slit width was 2 mm; the scatter slit width was 0.6 mm. The interlayer distances were determined using Bragg's Law for the (002) diffraction plane of the diffraction pattern of θ-ZrP and the (001) diffraction plane of the diffraction pattern for the intercalation products. For the ZrP: Cp_2MoCl_2 and ZrP: Cp_2TiCl_2 samples X-ray powder diffraction (XRPD) measurements were performed from 2 to 40° (in the 2θ axis) using a Siemens D5000 X-ray diffractometer with Cu Kα radiation (λ = 1.5406 Å) with a filtered flat LiF secondary beam monochromator.

The transmission electron micrographs (TEM) of the samples were acquired using a JEOL 2010 transmission electron microscope at an acceleration voltage of 200 kV. Samples were prepared using copper grids from Ted Pella. X-ray elemental distribution “maps” were obtained at the Department of Geology and Geophysics at Texas A&M University. Quantitative compositional analyses were carried out on a four spectrometer Cameca SX50 electron microprobe. The detailed information is provided in

the SI. The depth profile study was performed using the CAMECA IMS 4f ion microprobe employing a 5.5 keV oxygen plasma.

SIMS

The instrument used in these studies is a custom-built instrument equipped with a custom-built C_{60} source capable of producing $C_{60}^{+,2+}$ at 26 & 43 keV total impact energy.[130, 193] The instrumentation used for the analysis and the protocol used has been described extensively in the previous chapters.[131] Briefly, the instrument is equipped with a 1m linear time-of-flight (ToF) and an electron emission microscope. The singly and doubly charged C_{60} ions of interest were mass selected using a Wien filter. The collection of the start signal is triggered by the emitted electron from the impacted site. The targets were interrogated using the C_{60} projectiles sent in one by one at a repetition rate of 1000 impacts/s. A single projectile impact stimulated emission of secondary ions from a surface area of ~10nm and depth of ~5nm.The mass spectrum from each individual impact was recorded in a discrete manner and resolved. There is no overlap in time or space between successive projectiles.[194] This is key for effective quantitative observations in the event-by-event bombardment detection mode. The samples were negatively biased and each of the events was detected using an eight anode detector. The individual mass spectra were recorded and stored in a "total matrix of events" (TME)[195] and a summation of these individual spectra (~ 2 x 10^6 detection events) gives rise to the conventional mass spectrum. Using this technique it is possible to deconvolute the events with single secondary ion emissions and those with multiple emissions. If two or

more secondary ions are ejected from one bombardment event, they will be spatially related at the nanometric level. Additionally, it is also possible to compute the yields for each of these ions and find associations in their coemissions. Individual cluster impact TOF-SIMS consist of an accumulation of single events defined as one primary ion impact on target sample followed by the emissions of secondary ions and their subsequent detection.

A coincidental ion mass spectrum is generated by selecting an ion of interest and recording the collection of all coemitted secondary ions under individual projectile impacts. The coincidence secondary ion spectrum contains the record of colocalized secondary ions emitted from a given nanovolume after each individual impact.[196] Two or three discrete 200 μm radius spots were analyzed for each sample to ensure sample consistency and bulk homogeneity.

Sample Preparation

The Au coated Si wafers and stainless steel cubes were immersed and sonicated individually in ethanol and acetone baths for 10 minutes each. The wafers were then thoroughly dried with nitrogen. Each of the drug delivery ILN samples were agitated with DI water in 0.01% w/v using a sonicator for 15 min to create a slurry. 50 μL of the slurry was carefully drop-cast onto a cleaned wafer surface (Au side) and the moisture is allowed to dry quickly with the aid of a heating lamp. Once the material is affixed onto the wafer it is subsequently attached onto a stainless steel cube using carbon tape prior to

introduction into the vacuum chamber for SIMS analysis. For depth profile analysis the wafer is introduced directly into the vacuum chamber post deposition.

Results and Discussion

The objective of using SIMS in homogeneity analysis for nanomaterials utilized for drug delivery was both qualitative and quantitative. The first was to recognize both substrate (ZrP) as well as drug specific (cisplatin, titanocene, doxorubicin or molybdocene) ions to ensure intercalation from a qualitative assessment point of view. Secondly, to recognize and access whether at the nanometric level these intercalations are too subtle or pronounced enough for quantification. To this effect the first study looks at the unique intergallery spaces of the substrate layered material which is combined with stoichiometrically different levels of anti-cancer therapeutics. A proposed schematic of the intercalation reaction is provided in **Figure IV-2**. Cisplatin ($Pt(NH_4)_2Cl_2$/ MW 300.05 g/mol) was intercalated into θ-ZrP at stoichiometrically variant levels, to form three different materials with the ZrP:cisPt molar ratios varying from 1:1, 10:1 to 1:5 **(Figure IV-3)**.

Cisplatin-intercalated ZrP materials at different loading levels were synthesized with the purpose of elucidating how the modifications of the layered compound affect their structure, morphology, and physicochemical characteristics of the material, and study these characteristics in the produced materials. **Figure IV-4** shows the XRPD patterns obtained for α-ZrP and θ-ZrP upon reaction with different ratios (loading levels) of ZrP:cisPt (θ-ZrP converts to the α phase upon drying and therefore the

characterization of the dried intercalation compounds is going to be compared with the α phase of ZrP).[8] The XRPD patterns show the formation of a new phase with an interlayer distance of ca. 9.3 Å for all the intercalation products. In this new phase the interlayer distance of ZrP is increased by 2.7 Å, confirming that intercalation has taken place; α-ZrP has an interlayer distance of 7.6 Å but just one layer of ZrP has a thickness of 6.6 Å if the space occupied by the water molecule is excluded.[197, 198]

Cisplatin within the ZrP matrix is separated both depth wise and via planarity due to the substrate's layered nano structure. The labile nature of the chloride ligands in the cisplatin complex makes highly likely that in the new phase the chloride ions are displaced by the phosphate groups from the layer (**Figure IV-3**).[199] The location of the molecule facilitates the study of the secondary ion emission and its dependence on the 3-D location of the molecule of interest. By observing the recombination fragments in the higher mass ranges due to the addition of the substrate group (PO_2^- m/z 63) onto the identified cisplatin secondary ion $Pt(NH_3)_2Cl^-$ **(Figure IV-5)** we were able to determine the successful intercalation.

The negative ions in the mass range from m/z 320 to 340 are labeled as peaks suggested originating from the cisplatin addition to the ZrP, i.e., indicating the presence of the drug intercalation particulates (shown in **Fig. IV-5 a&b).**These are expected secondary ions considering the ion exchange capacity of ZrP. Additionally it can be

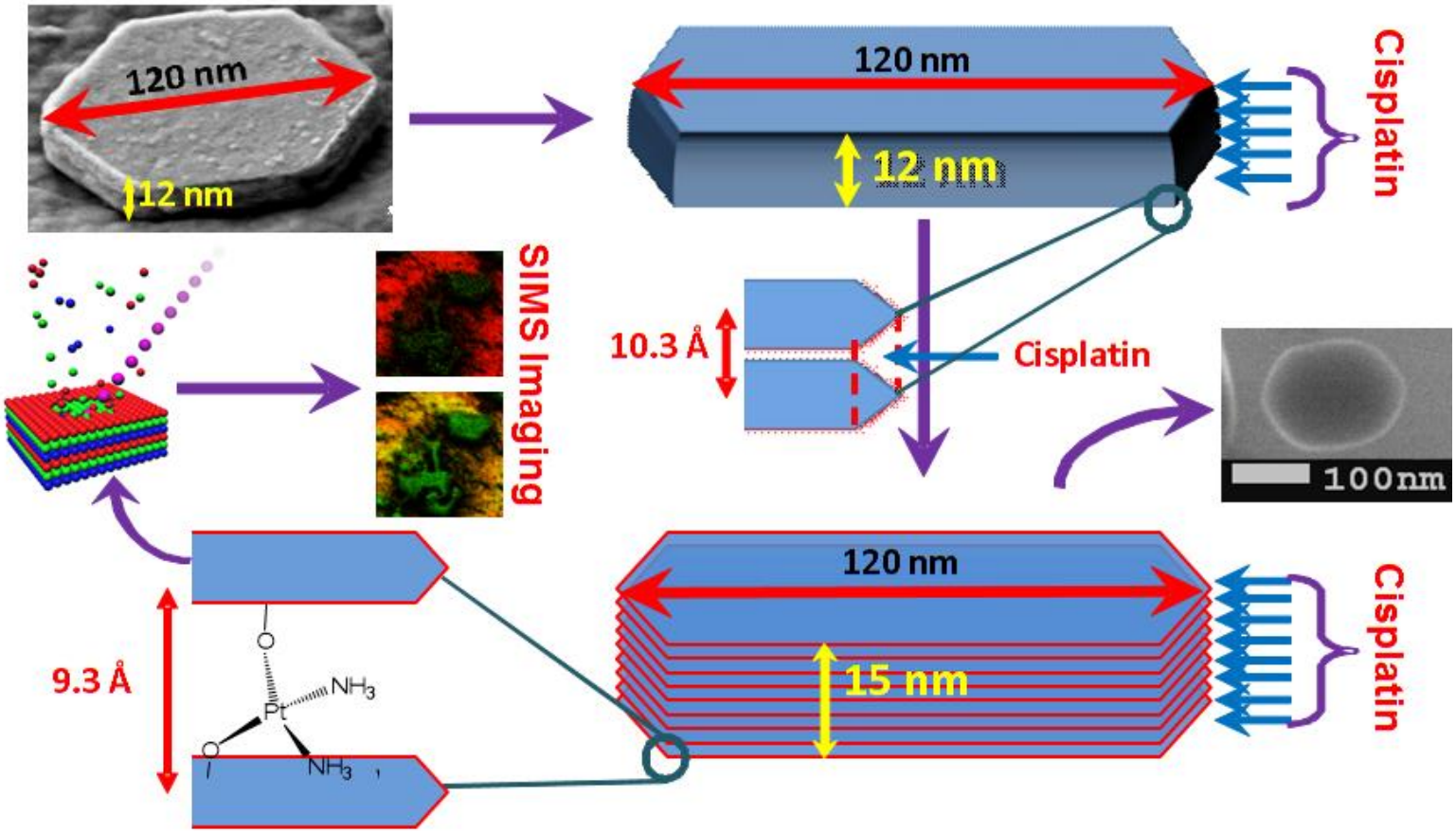

Figure IV- 2 – Schematic representation of the intercalation of cisplatin into θ-ZrP by direct ion-exchange; the image shows the intercalation of the cisplatin between layers of ZrP causing the formation of a new phase with an interlayer distance of 9.3 Å. Once intercalated the materials at their varied loading levels are analyzed using SIMS

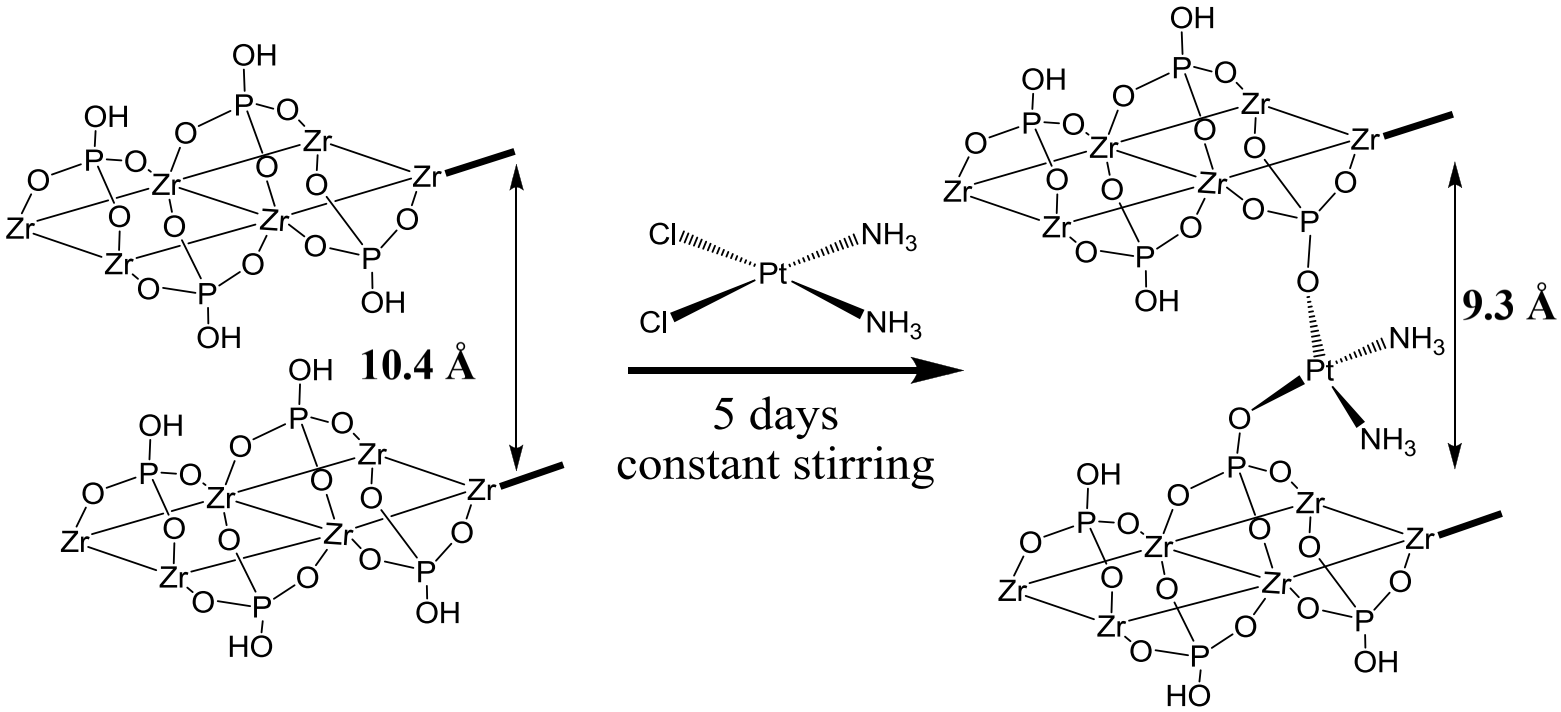

Figure IV-3 Proposed idealized intercalation mechanism for direct ion-exchange intercalation of cisplatin in θ-ZrP.

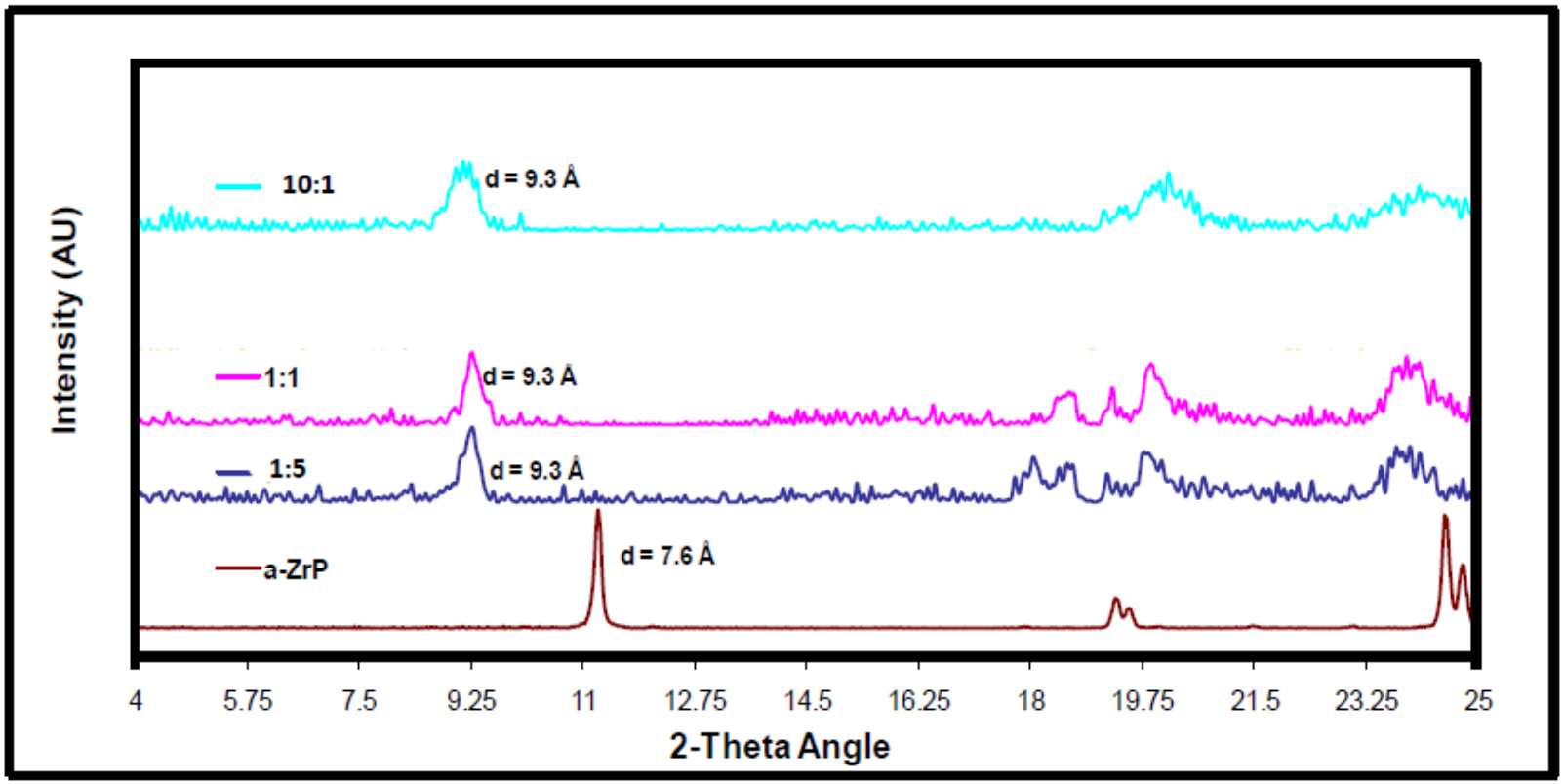

Figure IV-4 X-ray powder diffractograms for a-ZrP and the intercalation products of the reaction of ZrP and cisplatin at several ZrP:cisPt molar ratios. The molar ratios are (from top to bottom): 10:1, 1:1, and 1:5. (Adapted from Reference 158)

seen that the intensity of the signal due to these secondary ions from the combination of the substrate with the intercalate increases with the increase in the amount of intercalate (drug) as is observed in the normalized mass spectrum from **Figure IV-5b**. This is further revealed by looking at the % yields of the secondary ions of interest. We observe that at the highest loading level of the drug the yields for the secondary ion attributed to the drug are consistent with those observed by the drug in its native state. Additionally we see the reduced yields of the secondary ions in question at the lower loading levels attributed to the layered assembly of the drug within the ZrP galleries.

Because the location of the intercalate as well as the degree of distribution is of utmost importance for effective delivery, using the technique of SIMS the percent homogeneity of the material has been estimated. The impacts on the substrate (ZrP) were isolated from those on the intercalate ($Pt(NH_4)_2Cl_2$). Additionally events that involved secondary ion emissions of both from the same emission volume were also estimated using coincidence mass spectrometry. Each of these event types is illustrated in **Figure IV-6**. This information was then compared to the total number of events. The homogeneity of the intercalation of the cisplatin into the interlayer galleries could thus be estimated by monitoring the compilation events or "event type 3". A compilation event represents those events which result in the emission of secondary ions from both the substrate (ZrP) as well as the intercalate (cisplatin). The distribution of the drug at stoichiometrically variant loading levels was calculated in a similar fashion. The degree of homogeneity of each drug-matrix nano composite was calculated using the

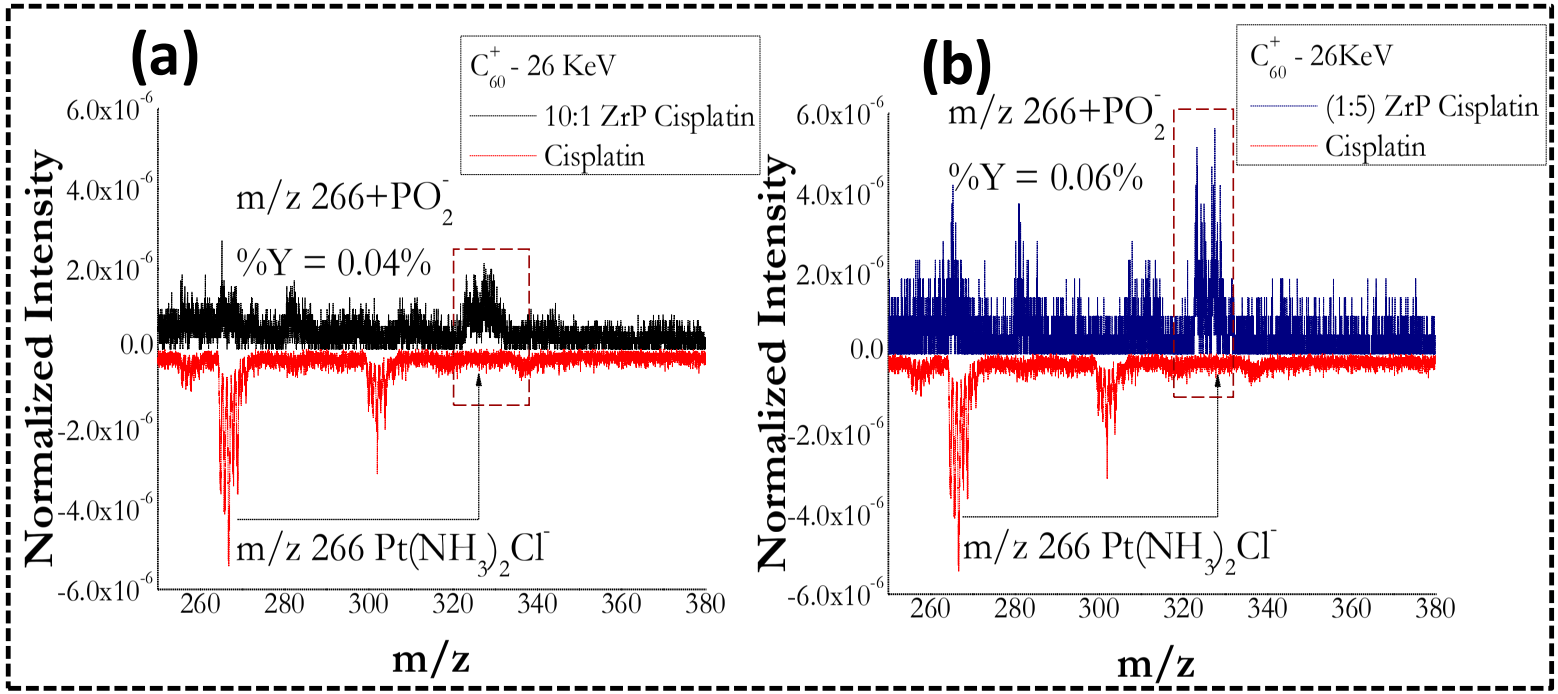

Figure IV-5: Negative ion mass spectra of cisplatin intercalated in ZrP nanoplatelets at two different loading levels (a) 10:1 (b) 1:5 vs. cisplatin in both cases in the negative y axis. The spectra are obtained under C_{60}^{+} bombardment at 26 keV total impact energy. The peak intensities are normalized to the total number of projectiles on the y-axis.

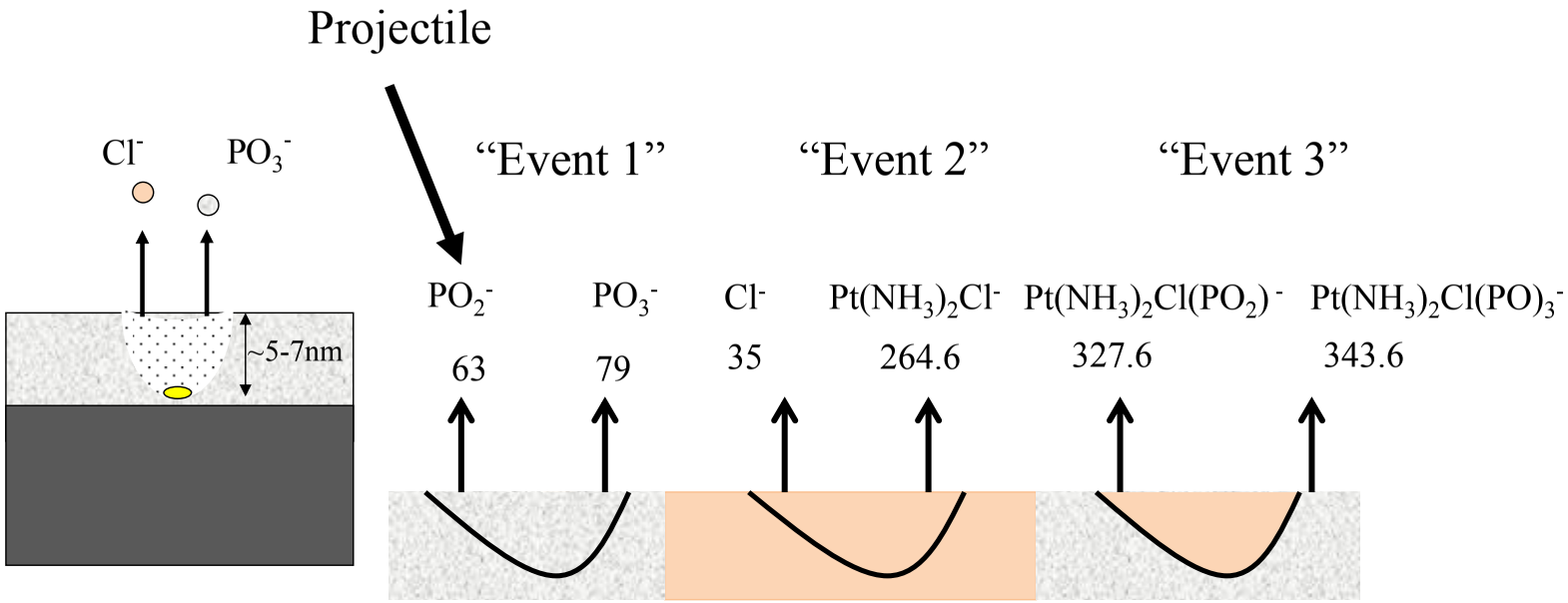

Figure IV-6: Scheme of event-by-event bombardment/detection mode. Event 1 signifies those events where the projectile leads to the emission of the substrate (ZrP) type SIs. Event type 2 determines those where we may only see SIs from the intercalate while Event type 3 are those events where we see SIs from both substrate and intercalate or compilation events. Since the signal derives from the impact of a single projectile, co-emitted secondary ions must originate from molecules co-located within the emission volume. In order to relate the information, we repeat this process of impacting the surface with a single projectile and recording the resulting SI's several times.

relationship described below. The ions that were used in each drug-substrate system to calculate distribution homogeneity are included in **Table IV-1.**

The degree of homogeneity, expressed as a percentage can then be calculated and can be extracted from the experimental data using the following relationships:

$$\frac{I_a \times I_b}{I_{a,b}} = \mathrm{N_x} \qquad \% \, Homogeneity = \frac{N_x}{N_o} \times 100$$

where, $I_{a,b}$ is the intensity of ion type ***a*** coemitted with ion type ***b***, obtained from the coincidence emission spectra. I_a and I_b are the intensities of ion a and b respectively which are obtained from the cumulative total matrix of events spectra. N_x represents the number of effective impacts on the drug fragments in the presence of the substrate (ZrP) while N_o represents the total number of collisions. "Event type 3" leads to the homogeneity calculations using coincidence mass spectrometry.

Using the afore mentioned setup the extent of homogeneity of the samples was estimated for each of the three ZrP:cisPt cases. The dimensions of each ZrP NP are approximately 150 nm with a thickness of about 15-30 nm depending on the size of the drug. Thus with each emission depth the chance of excavating a majority of the particle is quite high. We find that the 1:1 sample where the ZrP and cisplatin are in equimolar concentrations reveals the highest level of mixing, with a 94% event compilation, followed by a 54% compilation for the 1:5 material where the cisplatin is heterogeneously distributed due to the agglomeration of the intercalate on the substrate surface due the drug being in excess. Since the depth of emission is ~10 nm the

Drug	I_a	I_b
ZrP:cisPt (1:1), (10:1) & (1:5)	$Pt(NH_3)_2Cl^-$	PO_2^-
	Cl^-	PO_3^-
Doxorubicin	CN^-	PO_2^-
	CNO^-	PO_3^-
Titanocene	Cl^-	PO_2^-
		PO_3^-
Molybdocene	$Cp_2MoPO_2^-$	PO_2^-
	Cl^-	PO_3^-

Table IV-1: Ion intensities that are used to calculate the percent homogeneities in each drug delivery system. I_a represents the ion attributed to the drug while I_b is the ion from the substrate. This table describes the I_a and I_b in each of the drug-ZrP assemblies that were used in order to determine their respective homogeneities.

accumulation of cisplatin on the surface of the ZrP NPs inhibits the detection of ZrP secondary ions. The least amount of event compilation of 24% is found in the 10:1 where the substrate is in excess of the intercalate leaving behind several unsaturated galleries significantly reducing the probability of finding compilation events. This corroborates observations made with electron microprobe analysis. **Figure IV-7** & **Table IV-2** show the X-ray elemental distribution "mappings" obtained for the 10:1, 1:1, and 1:5 intercalation products which show the atomic distribution of Pt, P, and Cl in a 62 x 62 μm^2 section of the surface of the intercalation products. The X-ray elemental maps show uniform distribution of Pt and P in the 1:1 intercalation material with a very small amount of Cl. On the other hand for the 1:5 intercalation material there is an agglomeration of cisplatin on the surface with visible Cl depositions on the surface. In addition, for the 10:1 intercalation product there is a lack of Cl atoms, which was expected since in the intercalation product there appears to be a complete ion exchange of the drug into the ZrP layers.

Additionally a depth profile study was performed using the drug delivery materials at the CAMECA 4f ion microprobe employing a 5.5 keV oxygen plasma beam to study the isotopic elemental signal due to ^{190}Pt (intercalate) vs. the signal from ^{90}Zr (from the substrate). The material was sampled at different points to check for consistency of the signal. The results were consistent with those found using the SIMS and microprobe analysis. From the 1:1 sample (**Figure IV-8**) it can be seen that over time, while the ^{90}Zr signal is relatively constant for a singular spot (it fades once the entire sample has been excavated).

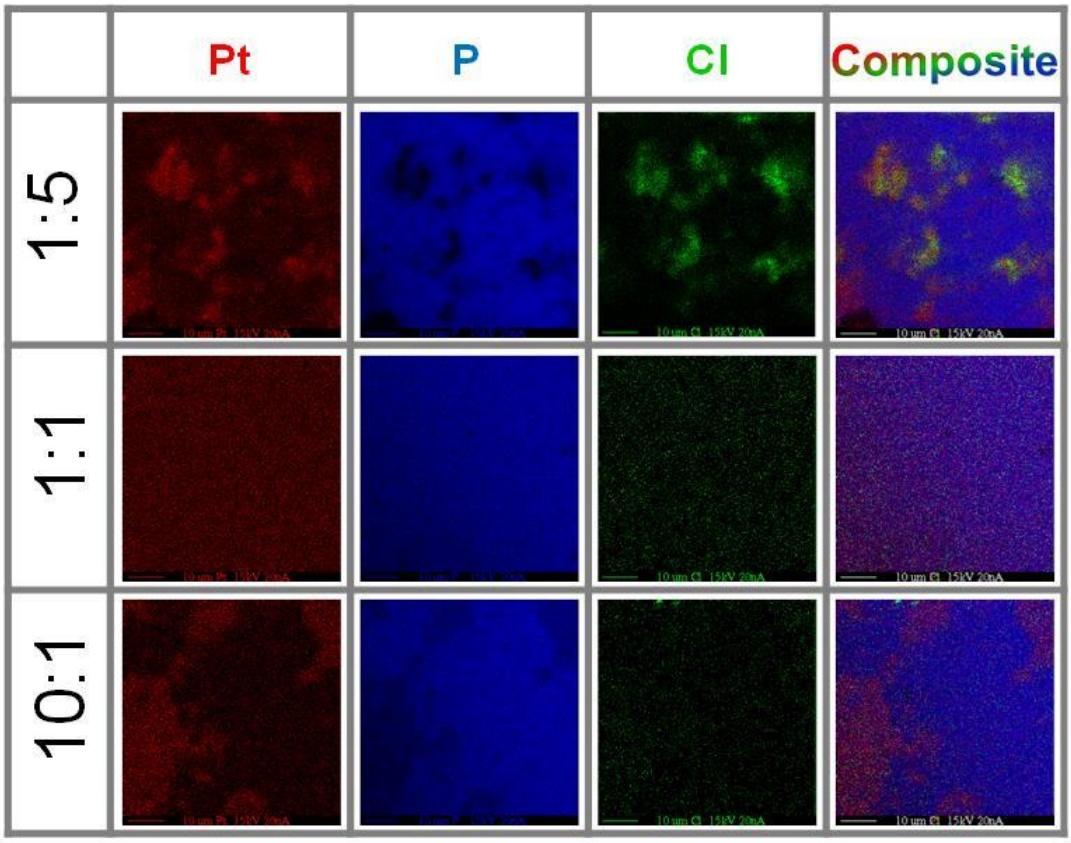

Figure IV-7:X-ray elemental distribution "maps "of ZrP:CisPt at 1:5, 1:1, 10:1 molar ratios. The microprobe image composites X-ray maps were generated using the program Image J® by combining three 8-bit X-ray images into a false color 24-bit RGB image, where red was selected for Pt, blue for P, and green for Cl. (Adapted from Reference 9)

ZrP:CisPt	MW	O	N	P	Cl	Zr	Pt
(1:5)	437.623	33.52	1.70	14.57	1.29	20.79	12.74
(1:1)	444.40	32.99	1.89	15.18	0	20.48	13.97
(10:1)	311.51	48.19	0.36	21.70	0	29.21	0.78

Table IV-2: Elemental analysis of ZrP:CisPt at 1:5, 1:1, 10:1 molar ratios for Pt, P, and Cl. (Reference 9)

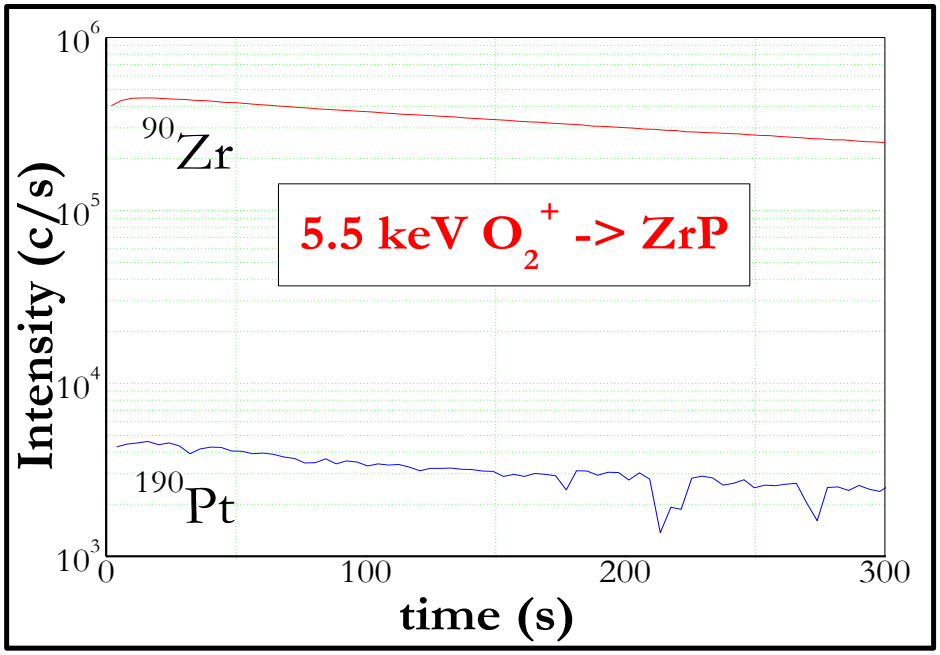

Figure IV-8. Depth profile of ZrP intercalated with cisplatin (1:1) using an O_2^+ primary beam (5.5 keV)

(a) ZrP:CisPt (10:1)	Point 1 (cps)*	Point 2 (cps)	Point 3 (cps)	Point 4 (cps)	Average (cps)*
190 Pt	15000	2971	3555	3373	3300
90Zr	227000	87300	83000	364000	178100

(b) ZrP:CisPt(1:1)	Point 1 (cps)	Point 2 (cps)	Point 3 (cps)	Average (cps)
190Pt	30400	33800	34700	32967
90Zr	189000	215000	198000	200667

Table IV-3. Depth profile study results obtained using the CAMECA 4f using a 5.5keV O_2^+ beam for ZrP:CisPt in (a) 10:1 (b) 1:1 loading ratios. (* Point 1 has been excluded after performing Dixon's Q test. The heterogeneity is an expected feature of this material since the substrate is in considerable excess of the intercalate.)

The signal from ^{190}Pt steadily decreases hinting at the layered arrangement. Furthermore, it can be seen that there is a signal correlation in the 10:1 sample when compared to the 1:1 sample (Table IV-2). The $^{90}Zr/^{190}Pt$ ratio for the signal of the (10:1) sample reveals a proportion of ~54 while the same ratio for the (1:1) sample reveals a proportion of ~ 6. The signal ratios for the (10:1) sample/ (1:1) sample result in a proportion of ~9 which is in close agreement with the expected value of 10 for the excess ZrP present in the former sample as compared to the latter (Table IV-3). There appears to be a direct relationship between the intensity of the signal measured in counts per sec (cps) for each of the isotopes in the corresponding materials that is further elucidated using depth profile analysis.

The 1:1 combination of the drug: substrate was analyzed for the next set of drugs, i.e., doxorubicin, molybdocene and titanocene. Figure IV-9 shows the XRPD pattern obtained for the intercalation product of doxorubicin into θ-ZrP. For the ZrP:Dox reaction product the resultant d_{001} plane shifts from 10.3Å in θ-ZrP to 20.3Å confirming the intercalation of doxorubicin. Figure IV-10 shows the X-ray diffractograms for α-ZrP, θ-ZrP and the intercalation products for the reaction of ZrP and molybdocene dichloride. The appearance of a new phase at 10.8 Å is attributed to the resultant ZrP: Cp_2MoCl_2 complex. Figure IV-11 shows the XRPD for α-ZrP, θ-ZrP and compared to the intercalation products of the reaction of ZrP and titanocene at several titanocene:ZrP molar ratios. Only the highlighted XRPD material is for consideration in the course of this thesis. The d_{001} plane is at 9.8 Å in the resultant ZrP: Cp_2TiCl_2 material.

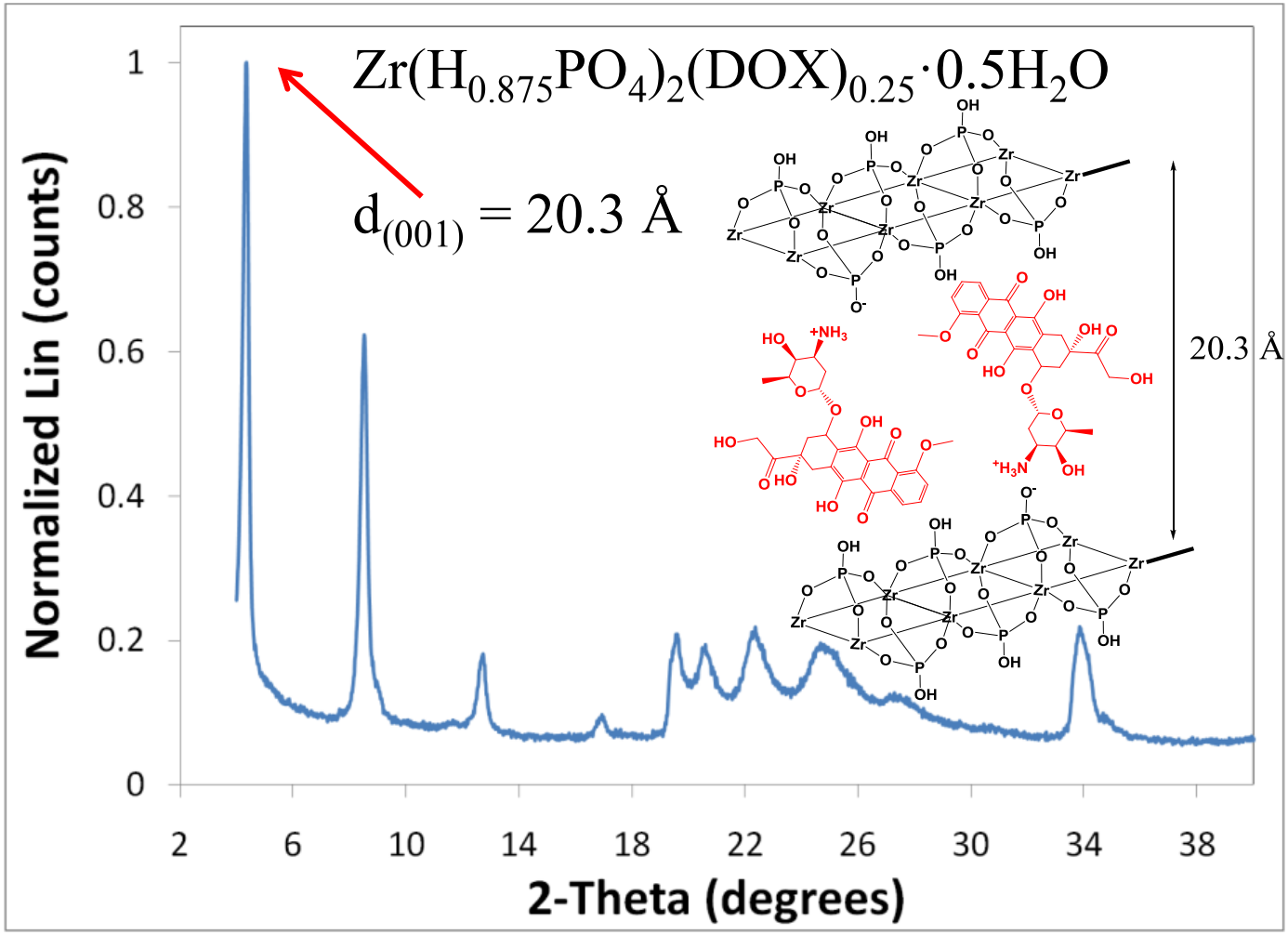

Figure IV-9 X-ray powder diffractogram for the intercalation product of doxorubicin into θ-ZrP. The d_{001} plane shifts from 10.3Å in θ-ZrP to 20.3Å due to the intercalation of doxorubicin into the layers. (Reference 11)

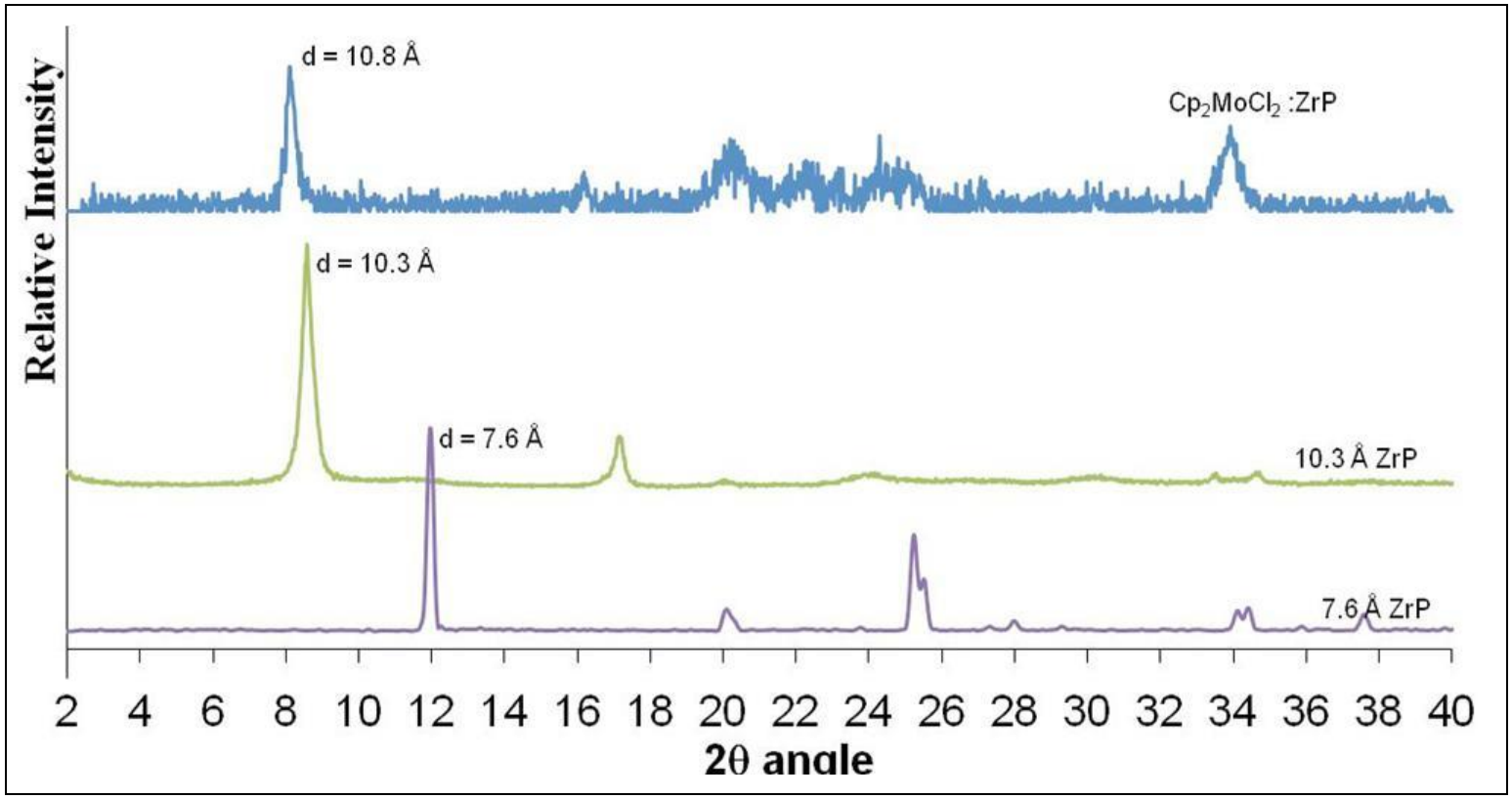

Figure IV-10: X-ray powder diffractograms for α-ZrP, θ-ZrP and the intercalation products of the reaction of ZrP and molybdocene dichloride. The d_{001} plane shifts to 10.8 Å in the resultant molybdocene-ZrP complex. (Reference 9)

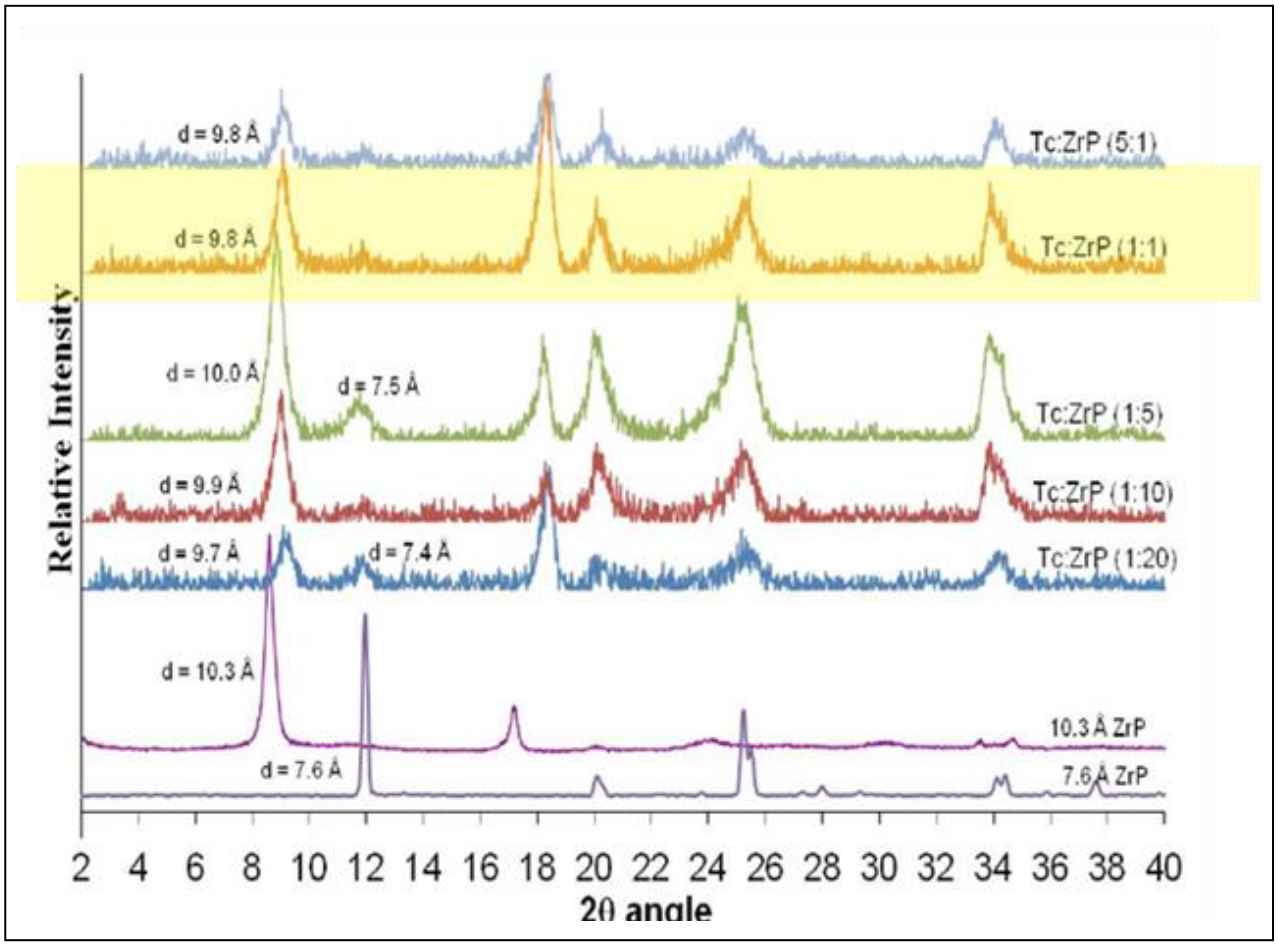

Figure IV-11: X-ray powder diffractograms for α-ZrP, θ-ZrP (bottom two spectra) and the intercalation products of the reaction of ZrP and titanocene at several titanocene:ZrP molar ratios. Only the highlighted XRPD material is for consideration in this paper. The d_{001} plane is at 9.8 Å in the resultant titanocene:ZrP material. (Reference 9)

For each of the drug:ZrP samples, the combinant secondary ions attributed to the ion exchange reaction between the drug and the substrate were identified and have been elucidated on each individual mass spectra. Next the % homogeneities for each were also determined. **Figure IV-12, 13 & 14** determine the cumulative mass spectra for ZrP:doxorubicin, ZrP:titanocene and ZrP:molybdocene respectively. A sample calculation is illustrated in the case of doxorubicin ($C_{27}H_{29}NO_{11}$ /MW 543.52 g/mol) in **Table IV-4**. The N_{eff}/N_o for ZrP is equal to that of doxorubicin indicating that the effective number of impacts on the drug are equal to those on the substrate thus revealing the homogeneous nature of the drug-substrate assembly. Additionally the % homogeneity is calculated to be 90% using the earlier given relationship. The mass spectrum in **Figure IV-10** shows a signature fragmentation pattern elucidated by the subsequent N^{15} additions in the higher mass regions between m/z 280–350 attributed to the drug also appearing in the drug:substrate hybrid material albeit in smaller yields due to the layers of ZrP that it is incorporated in.

The next sample that was analyzed for homogeneity was titanocene (Cp_2TiCl_2/ MW 248.96 g/mol) intercalated in ZrP, (**Figure IV-13**)**.** The information from the impacts on the substrate (ZrP) were isolated from those on the intercalate Cp_2TiCl_2. Additionally events that involved secondary ion emissions of both from the same emission volume were also estimated using coincidence mass spectrometry. This information was then compared to the total number of events (>1 million). The homogeneity of the intercalation of the titanocene into the interlayer galleries could thusly be estimated by monitoring the compilation events. The % homogeneity for the

Effective # of impacts (N_{eff})	m/z	Yield	Coincidental Yield	N_{eff}/N_0* *Stdev = ± 0.015
ZrP	79	1.0×10^{-1}	2.2×10^{-2}	0.52
	63	1.0×10^{-1}	2.1×10^{-2}	0.53
Doxorubicin	340	3.8×10^{-3}	4.8×10^{-5}	0.55
	326	7.1×10^{-3}	4.7×10^{-5}	0.55

Table IV-4: Homogeneity calculation values for doxorubicin intercalated ZrP at loading level 1:1. The effective number of impacts on doxorubicin equals the effective number of impacts on ZrP implying homogeneity of the material.

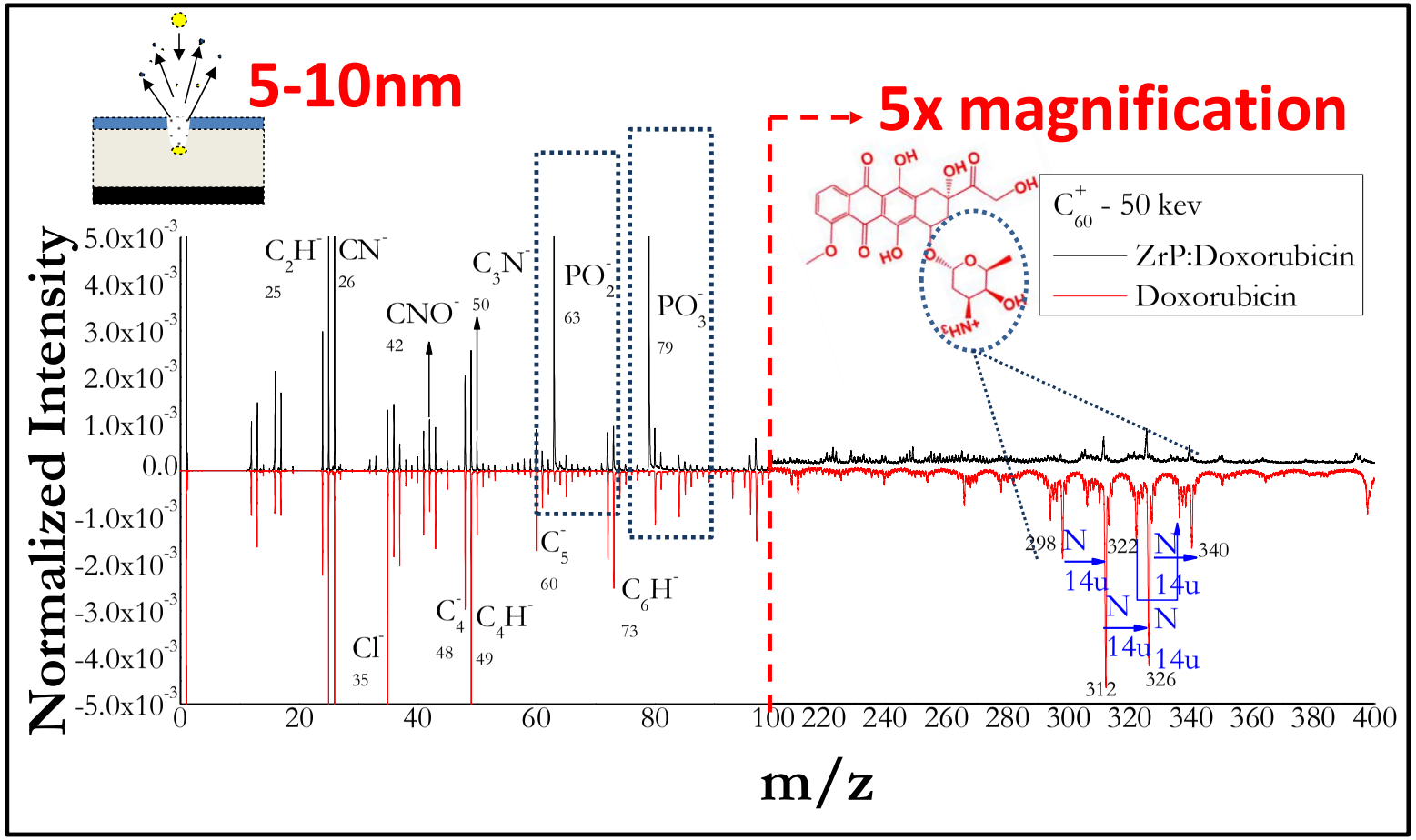

Figure IV-12 Negative ion mass spectra of doxorubicin intercalated in ZrP nanoplatelets at 1:1 loading level vs. doxorubicin. The spectra are obtained under C_{60}^{2+} bombardment at 43 keV total impact energy. The peak intensities are normalized to the total number of projectiles on the y-axis.

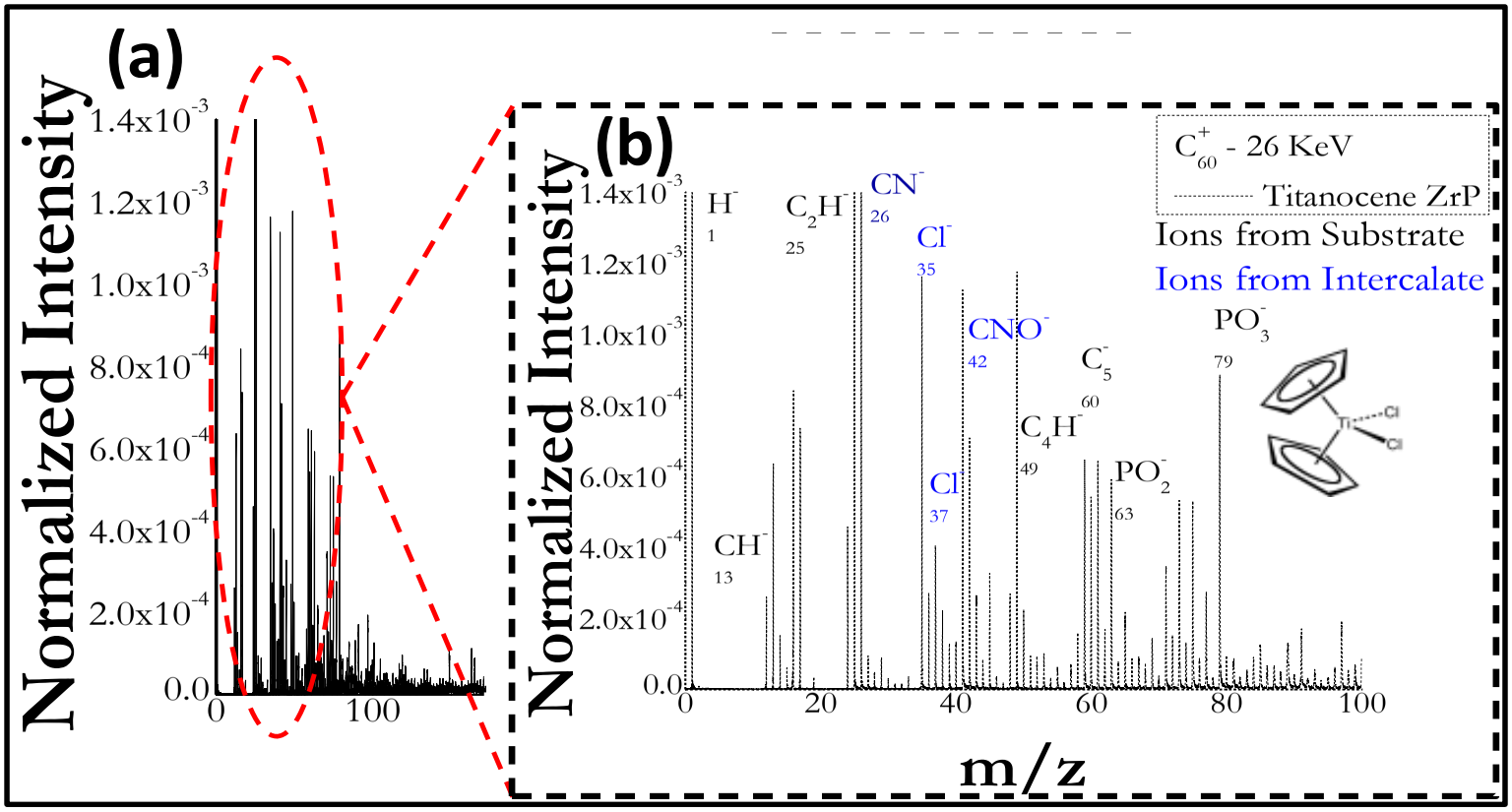

Figure IV-13: **(a)** Negative ion mass spectra of titanocene dichloride intercalated in ZrP nanoplatelets at 1:1 loading level **(b)** Magnified view of m/z 1-100. The spectra are obtained under C_{60}^{+} bombardment at 26 keV total impact energy. The peak intensities are normalized to the total number of projectiles on the y-axis.

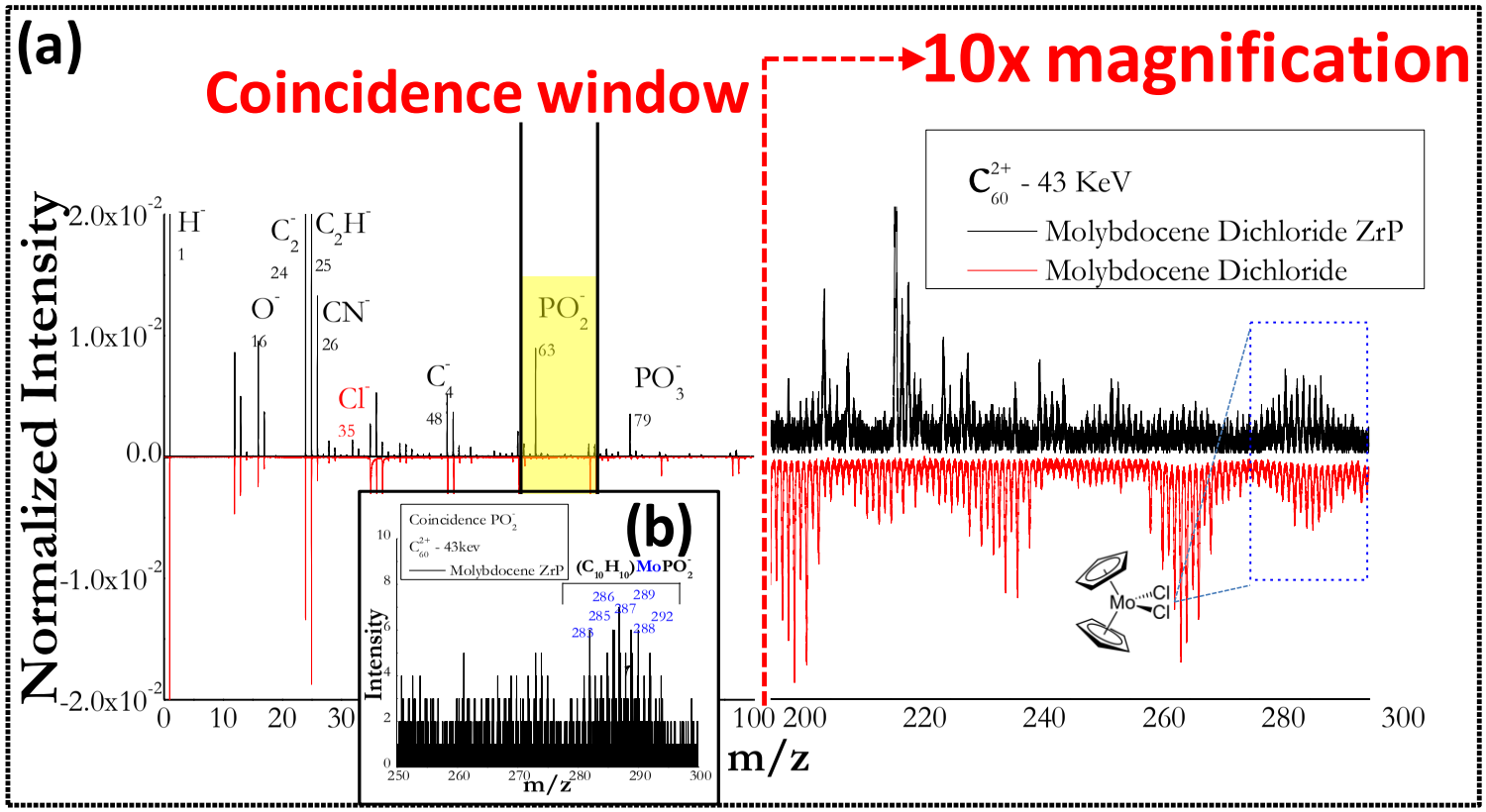

Figure IV-14: **(a)** Negative ion mass spectra of molybdocene dichloride intercalated in ZrP NPs at 1:1 loading level vs. molybdocene dichloride. The spectra are obtained under C_{60}^{2+} bombardment at 43 keV total impact energy. The peak intensities are normalized to the total number of projectiles on the y-axis. **(b)** Coincidental ion mass spectrum with ion at m/z 63 from spectra (a). The ion exchange fragment attributed to substrate drug interaction is a lot easier to characterize once the coincidence window is placed. It effectively filters out excess unrelated secondary ions.

titanocene dichloride intercalated ZrP at the 1:1 loading level was calculated to be 91%. The secondary ions from the intercalate are marked in the mass spectrum. The homogeneity of molybdocene dichloride (Cp_2Cl_2Mo/ MW 297.04 g/mol) intercalated ZrP at the 1:1 loading level was also estimated in a similar fashion and found to be ~91%. In **Figure IV-14** the clustering effect of the secondary ions is observed due to the presence of the seven stable isotopes (masses 92, 94, 95, 96, 97, 98, and 100) of molybdenum leading to the appearance of sequential clusters.

In order to facilitate the identification of additional secondary ions a coincidence spectrum was obtained (**Figure IV-14b**) by putting a window onto the m/z 63, PO_2^- .This simplified the spectra while making apparent the secondary ions that can be attributed to the intercalated material. In the case of 150 nm intercalated ZrP NPs the 1:1 drug to substrate loading ratios seem to provide the best level of homogeneity in each of the four separate drug delivery systems that were tested and hypothesized. **Table IV-5** provides a quick recap of all the homogeneity results that were obtained. It would be interesting to test this theory out with other types of ILNs more extensively in the future.

Conclusions

This study illustrates the ability of SIMS in the individual impact mode to a) provide a label-free mass spectrometric technique for the qualitative assessment of drug intercalated ILNs as has been illustrated by the incorporation of four distinct drug molecules into the ZrP substrate b) quantify the degree of homogeneity and distribution of the drug within the confines of the substrate as was illustrated specifically with the

ZrP:cisPt intercalation reactions in the nanometric domain through standardized sample preparations. Each of the studies presented demonstrates the ability of SIMS in the mode of single cluster impacts to determine composition and homogeneity with ~20 nm spatial resolution[127]. The scope of the type of applications and materials discussed in this model system study are quite extensive and may be broadly applied as a possible tool for nanomaterial characterization in drug delivery material characterization.

Sample		%Homogeneity (± 2%)
ZrP:cisplatin	1:1	94
	10:1	24
	1:5	54
ZrP:doxorubicin	1:1	90
ZrP:titanocene dichloride	1:1	91
ZrP:molybdocene dichloride	1:1	91

Table IV-5: Percent homogeneity calculated values for all the materials.

CHAPTER V

CONTROLLED RELEASE OF ANTICANCER DRUG ENCAPSULATED INORGANIC LATTICE TO GOVERN DRUG UPTAKE MECHANISMS*

Introduction

This chapter demonstrates, the very small, but growing body of literature regarding a recently discovered application of layered compounds, which involves the ability of layered materials to sequester and later release molecules of chemical and biological significance. The use of cytotoxic drugs in chemotherapy is a widely prescribed method of cancer treatment. The side effects of using anticancer drugs to tumor cells are well documented and hard to circumvent. In recent years nanoparticle mediated drug delivery for overcoming the damaging effects of these drugs is an emerging strategy. For successful cancer therapy, high efficacy and low side effect drugs are highly needed, which might possibly be achieved by drug-nanoparticle hybrid systems. A relatively new addition in the realm of nanoparticle mediated drug delivery is the use of inorganic layered nanoparticles.[8, 11, 50, 157]

---

*Parts of this chapter are reprinted with permission from *Nanoscale*, Volume 5, Agustín Díaz, Millie L. González, Riviam J. Pérez, Amanda David, Atashi Mukherjee, Adriana Báez, Abraham Clearfield and Jorge L. Colón, Direct intercalation of cisplatin into zirconium phosphate nanoplatelets for potential cancer nanotherapy, pages 11456-11463, 2013. Copyright [2013] Royal Society of Chemistry.

They afford greater robustness in structural determination as well as significant characteristic information about drug loading and homogeneity as was described in the previous chapters. Several previous studies with similar materials have suggested that anticancer drug loaded inorganic layer nanoparticle systems offer considerable enhanced cellular uptake of drugs and consequently suppress cancer cell proliferation effectively as well.[200-202]

In literature the use of luminescent porous silicon oxide nanoparticles,[203] gold (or silver) nanoparticles[204] have emerged as among the most successful inorganic based nanoparticles. They, however have shown evidence of cellular cytotoxicity and hemolytic activity.[205, 206] In addition as discussed in the introduction of this thesis, the spherical shaped nanoparticles exhibit poor penetration through vascular fenestrations and diminished endothelial wall adherence. The use of non-spherical, size controlled layered nanomaterials can lend itself to enhanced permeability and retention (EPR) by which macromolecules can accumulate passively and preferentially. The carrier material encapsulates and protects the drug from external media. This ensures the drug remains biologically inactive until a "trigger" enables the drug-loaded material inside the cancer cell where the cargo may finally be selectively released. This "trigger" is the dissolution of the carrier material in the micro-acidic cancer cell or cell lysosomal environment. The delamination or direct ion-exchange of the intercalated drugs with the ions in the cell interior allows for the eventual release of the drug.[73]

In this present study, anticancer drug intercalated zirconium phosphate composites are investigated for their drug release profiles and capacities as a function of the drug loading and material homogeneities. Additionally, this chapter attempts to investigate the cellular interaction and uptake of nanoparticles since ZrP is being considered as a possible candidate for drug delivery nano vehicles. Since ZrP is relatively harmless to the body and is not associated with any metabolic functions it makes for an ideal candidate. The platelet-like shape of these materials shows better adhesion, margination and binding properties than its spherical counter parts.[74, 75] While under standard biological conditions (pH – 7.2 – 7.4) ZrP is relatively stable, it is expected that once it reaches a low pH environment such a cancerous cell microenvironment where the pH is generally low (pH 4), it will release its loaded drug cargo. In addition, as the drug-loaded ZrP nanoparticles reach the extreme conditions of the lysosome and the peroxisomes, they will dissociate the ZrP to form phosphate ions and harmless zirconium salt or oxide both of which have excellent renal clearance.[8] Designing nanomedicines with enhanced and intentional functionalities requires an understanding of the intracellular trafficking pathway of nanoparticles so that their fate in the cell can be predicted. In the literature it has been reported that nanoparticles such as iron oxide and silica, as well as carbon nanotubes are internalized in cells via endocytotic pathways.[201, 207-209] Endocytosis is a conserved process in eukaryotes by which extracellular components are taken up into cells by invagination of the plasma membrane to form vesicles that enclose these materials.

This chapter discusses specifically the effectiveness of the ZrP nanoparticles in the delivery of cisplatin and doxorubicin drugs. The cisplatin and doxorubicin intercalated ZrP nanoplatelets were explored for their cytotoxicity elsewhere.[158] In brief, the toxicity of ZrP nanoparticles has been extensively explored from normal to malignant human cells (Figure V-1&2). The biocompatibility of the ZrP NPs were assessed using an MTT assay, a colorimetric assay for assessing cell viability in different cells lines. The human embryonic kidney cells lines or the HEK-293 are commonly used in drug toxicity studies to assess effects of drug candidates on the renal system. ZrP NPs at concentration of upto 1000 μg mL^{-1} don't appear to affect the cell viability of the HEK-293 after 24 h and 72 h incubation times indicating the benign nature of ZrP to human kidneys (Figure V-1). The ZrP nanoplatelets are also found to be nontoxic to the human metastatic breast cancer (MDA-MB-231) cell lines after 24 h, 48 h and almost 96 hrs. of incubation (Figure V-2). This indicates that the ZrP alone does not have any cytotoxic effects on the cells and can be used as a vehicle for drug delivery. Additionally, it has also been demonstrated that ZrP NPs are highly hemocompatible, showing no hemolytic activity towards the human red blood cells (RBCs).[158]

In this study, the in vitro release profiles of doxorubicin loaded ZrP and cisplatin loaded ZrP were investigated. In the case of the anticancer drug Cisplatin (cis-diamminedichloroplatinum(II), cis-$Pt(NH_3)_2Cl_2$), the platinum complex is monitored in the release studies from the nanoparticles and the particle degradation in simulated body fluid (SBF) and artificial lysosomal fluid (ALF).

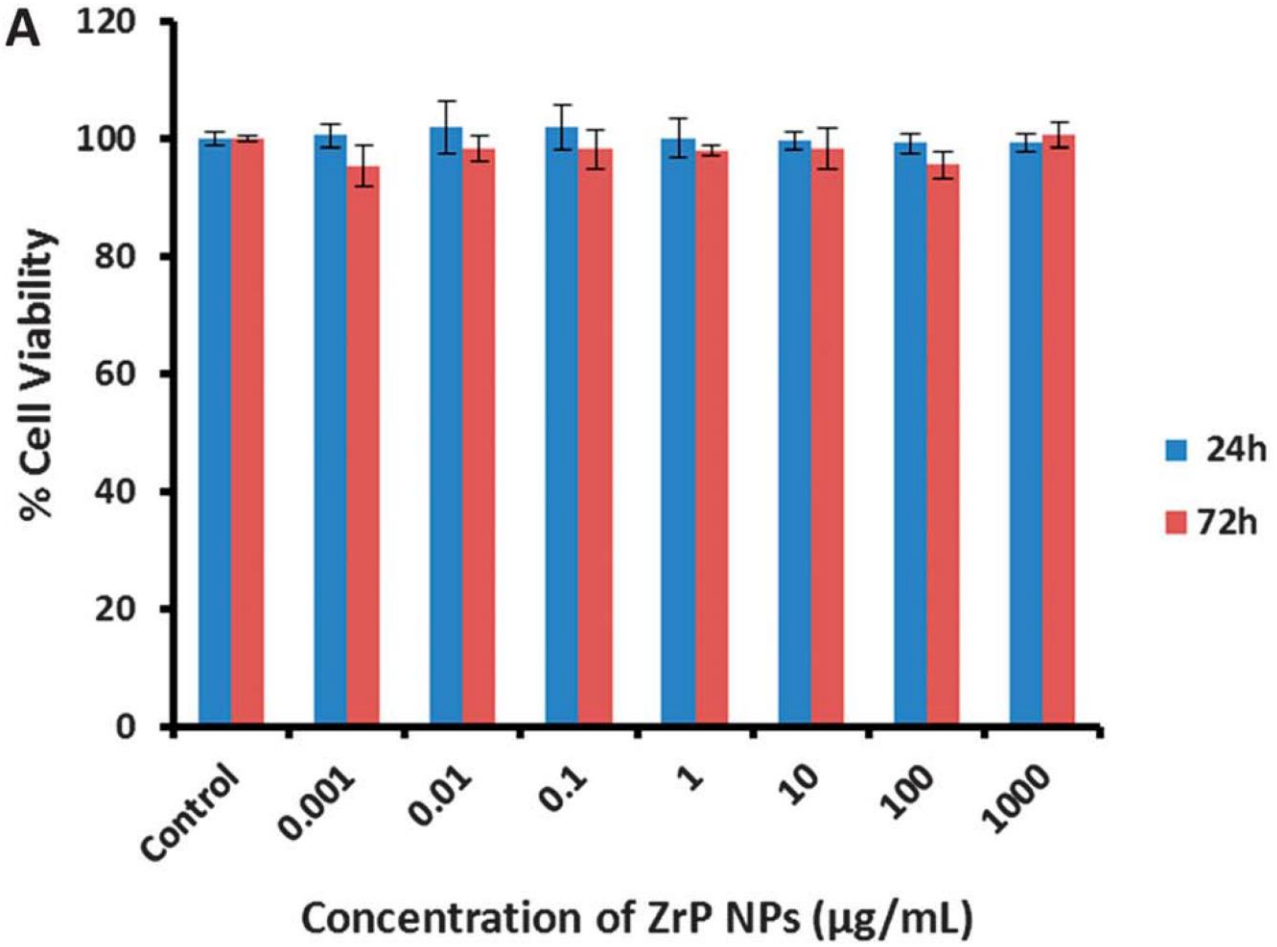

Figure V-1: Cytotoxicity of zirconium nanoplatelets (ZrP NPs) to human embryonic kidney (HEK-293) (Reference 158)

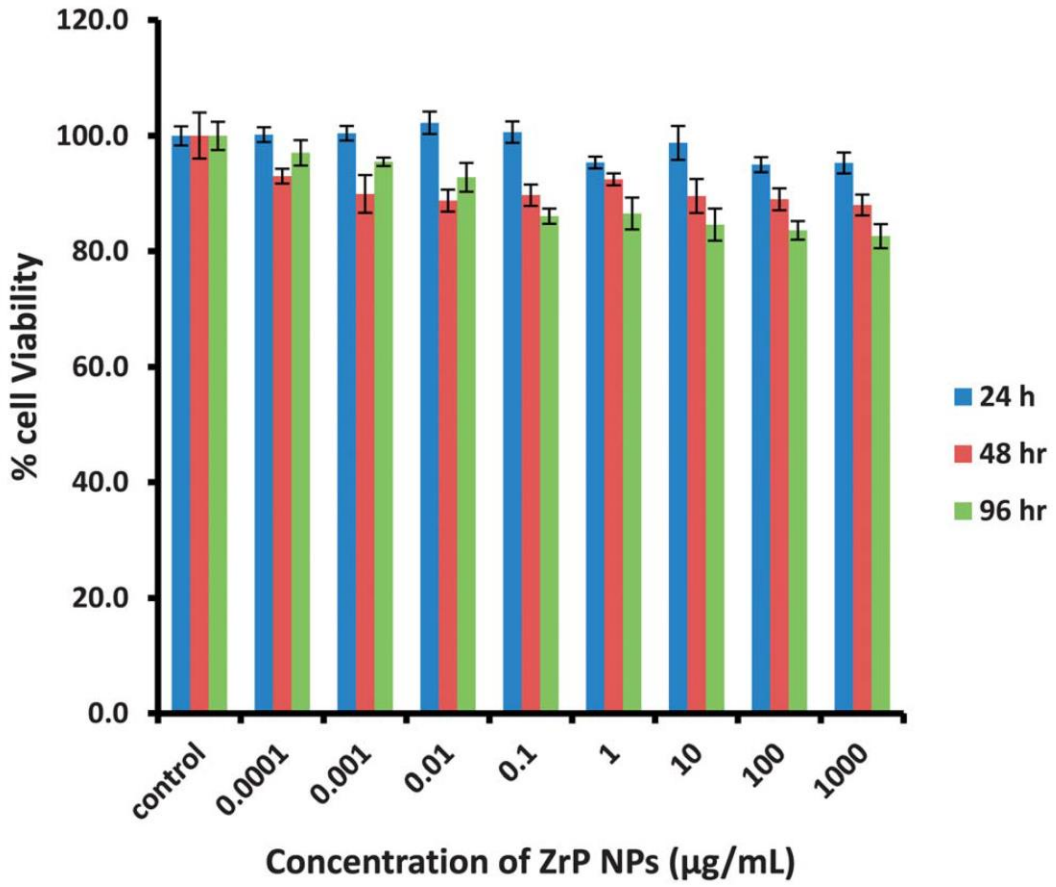

Figure V-2: Cytotoxicity of zirconium phosphate nanoplatelets (ZrP NPs) to human metastatic breast cancer MDA-MB-231 cells after 24 h, 48 h and 96 h of incubation. (Reference 158)

Doxorubicin being confocally active was monitored using fluorescence microscopy to quantify release in a similar fashion. Subsequently the delamination of the ZrP material is also monitored using elemental zirconium quantification over time. Next the cellular uptake mechanisms employed in nanoparticle uptake were also explored using HeLa cells lines.

Experimental Methods

Materials

Zirconium(IV) oxychloride octahydrate ($ZrOCl_2 \cdot 8H_2O$), ethanol, acetone, cis-diamminedichloroplatinum(II) and doxorubicin hydrochloride were obtained from Sigma-Aldrich (St. Louis, MO). Phosphoric acid (H_3PO_4) at 85% (v/v) (ACS grade reagent) was obtained from Fisher. Water was of nanopure quality from a Zyratech reverse osmosis water system (18 MW/cm). Other chemicals and reagents were of analytical grade.

Intercalation Procedure

The intercalation procedure has been described in the previous chapters. In brief, the intercalation was performed by the batch method by adding 50 mL of a solution containing θ-ZrP with the desired quantity of cisplatin or doxorubicin. The loading levels used in the course of this study for the cisplatin loaded drugs were: 1:1 , 1:5 and 1:10 cisplatin:ZrP. For the doxorubicin intercalations doxorubicin at different

concentrations (0.14, 0.25 and 0.35 ratio of DOX to ZrP (DOX:ZrP) w/w) for five days to produce varied loading levels in the desired materials. The intercalation was done in a dark environment at room temperature; monitoring the intercalation procedure by the change in pH in the case of both drugs. When the pH finally stabilized (approximately 5 days later) the suspensions of each material were centrifuged and subsequently filtered using a 0.22 μm Millipore filter membrane.

At this stage the filtered material was divided up into two parts for each of the above samples. The first half was re-suspended in ~50 mL of miliQ water while the second half was dried under vacuum and subsequently pulverized. The powdered material was used for the purposes of characterization while the second part was used for the purposes of cell work and release studies. In terms of the doxorubicin release studies only the 14% and 25 % loading levels (w/w) were concentrated upon to establish the difference in drug release behavior. The highest loading level 1:1 or 35% loading by weight was used for the purposes of the cell mechanism study.

Instrumentation

Most of the characterization for the dried materials were described in detail in the previous chapters. Briefly, some of the techniques are discussed:

X-ray Powder Diffraction Analysis (XRPD)

These experiments were performed using a D8 X-ray diffractometer system (Bruker AXS, Madison, WI) with a copper anode source (Kα,λ = 1.54Å) equipped with a

flat filtered LiF secondary beam monochromator. The divergence receiver and detector silts are all 2mm apart and the scatter slit width is 0.6 mm. The interlayer distances are determined using the Bragg's law for the (002) diffraction plane of the θ-ZrP. The intercalations for each material are compared to the θ-ZrP and α-ZrP to establish a successful reaction.

Transmission Electron Micrography (TEM)

The transmission electron micrographs (TEM) of the samples were acquired using a JEOL 2010 transmission electron microscope at an acceleration voltage of 200 kV. Samples were prepared by dispersing the solids in ethanol with an ultrasonic bath followed by deposition on a formvar/carbon coated copper grid (Ted Pella, Inc., Redding, CA).

Microprobe Analysis

Quantitative compositional analyses were carried out on a four spectrometer Cameca SX50 electron microprobe in the Department of Geology and Geophysics at Texas A&M University. Analyses were run at an accelerating voltage of 15 kV at a beam current of 20 nA. All quantitative work employed wavelength-dispersive spectrometers (WDS). Analyses were carried out after standardization using very well characterized compounds or pure elements. Qualitative analyses (spectra) were obtained with an Imix Princeton Gamma Tech (PGT) energy dispersive system (EDS) using a thin-window detector.

Typical accuracy for major elements (> 10 wt. %) is about =+/- 1 to 2 % of the amount present; the uncertainty at low concentrations would increase as the concentration decreased, with the uncertainty reaching 100% at the lower limit of detection (LLD). The lower limit of detection for most elements under typical conditions would usually be about 0.05 to 0.10 wt. %. Pressed powder samples will have some additional uncertainty based on surface roughness. The main effect of surface roughness will be to reduce analytical totals because of X-ray scatter. However, X-ray scatter is also wavelength dependent, which could result in a few percent change in apparent elemental ratios if the surface is very rough and there are significant differences in wavelength.

X-ray elemental distribution "maps" were obtained at 15 kV and 20 nA. beam current in beam scanning mode. For the 1500x (62 μm) maps, the beam was rastered in a 256 by 256 point grid, with a grid spacing of 0.24 microns and a total acquisition time of 600 seconds. Composite X-ray maps are generated by combining three 8-bit X-ray images into a false color 24-bit RGB image (ImageJ program)

Dynamic Light Scattering (DLS)

The particle size and zeta potential of the ZrP nanoplatelets were determined using a Brookhaven ZetaPALS particle and zeta potential analyzer (Holtsville, NY).

Inductively Coupled Plasma-mass Spectrometry (ICP-MS)

The ICP-MS analyses were performed on a Perkin Elmer NexIon 300 D instrument running in the standard mode with a quadrupole mass spectrometer (1% nitric acid matrix was used to digest the samples).

Microscopy

Imaging was performed on an inverted epifluorescence microscope (Model IX81; Olympus, Center Valley, PA). Images were captured with a Rolera-MGI Plus back-illuminated EMCCD camera (Qimaging, Surrey, BC, Canada). Imaging was performed using bright-field and fluorescence imaging with the RFP filter set (Ex = 560 $\pm$ 20 nm/Em = 630 $\pm$ 35 nm). The excitation light was from a 100 W mercury lamp (Leeds Precision Instruments # L202 Osram) passed through the filter cubes and a 100X objective. The bright-field and fluoresce images were captured with the Slide Book 4.2 software (Olympus).

***In vitro* Drug Release Study**

The *in vitro* drug release profile experiment was performed using the dialysis method. The simulated body fluid (SBF) was prepared according to Kokubo and Takadama.[210] Briefly, NaCl, $NaHCO_3$, KCl, $K_2HPO_4 \cdot H_2O$, $MgCl_2 \cdot 6H_2O$, $CaCl_2 \cdot 2H_2O$, and Na_2SO_4 salts were dissolved in mili Q water and buffered with TRIS (99% Aldrich) and HCl in order to keep pH at 7.4 at 37ºC. Each salt was allowed to dissolve fully prior to the next salt addition. In addition the containers used were cleaned thoroughly with

dilute HCl to ensure no contamination occurred. Artificial lysosomal fluid (ALF) was used to simulate different interstitial conditions in the cellular environment that the nanoparticles may encounter after phagocytosis which is for all essential purposes the cell's "feeding" mechanism. It was prepared by dissolving $MgCl_2$, NaCl, Na_2HPO_4 , Na_2SO_4, $CaCl_2.2H_2O$, sodium citrate, $C_6H_8O_7$, NaOH, glycine, sodium tartrate dehydrate, sodium lactate and sodium pyruvate in miliQ water. [211]

In a typical experiment a suspension of about 0.00067% w/v (g/mL) of the intercalated material (cisPt@ZrP) was exposed with SBF (pH = 7.4) or ALF (pH = 4.5), simulating the same ionic concentration of human environment. The suspension of the intercalated material was agitated using polypropylene vials and placed into an orbital shaker (VWR International, LLC, Suwanee, GA) at 37 ºC and 130 rpm. Aliquots of 5 µL were taken at specified periods of time from the external volume. The aliquots were centrifuged for a period of 1 minute to avoid any possible light scatter. The release of the platinum complex from the layers was monitored by ICP-MS, by determining the Pt concentration in each aliquot. At the same time the concentration of Zr was also monitored by ICP-MS to determine the hydrolysis of the nanoparticles under biological conditions. The release tests were repeated thrice for establishing consistency.

The *in vitro* release behaviors of DOX from DOX:ZrP NPs were also monitored using simulated body fluid (SBF) (pH 7.4) or ALF (pH 4.5). Briefly, ~10 mg of DOX:ZrP NPs at various loading levels were immersed individually in 45 mL of SBF or ALF and sampled at predetermined time intervals. The concentration of DOX in the sample was measured using a DU 800 UV-vis spectrophotometer (Beckman Coulter,

Inc., CA) at a maximum absorbance of 488 nm after centrifugation. The release profile was obtained by plotting the cumulative release (%) against time:

$$\text{Cumulative Release (\%)} = [Pt]_t / [Pt]_o \text{ X } 100$$

$$[DOX]_t / [DOX]_o \text{ X } 100$$

$$[Zr]_t/[Zr]_o \text{ X } 100$$

where $[Pt]_t$, $[DOX]_t$ and $[Zr]_t$ are the concentrations of Pt, Doxorubicin and Zr, respectively, at time *t* and $[Pt]_o$, $[DOX]_o$ and $[Zr]_o$ are the total amount of Pt, Doxorubicin and Zr used in the experiment, respectively. Quantitative determinations of DOX were based on pre-calibration of the spectrometer using standard solutions of DOX in both SBF and ALF. The DOX release test was performed in the darkness. The release tests were repeated 3 times (three independent experiments) and the results are given as average values and standard deviations.

Immunofluorescence/Confocal Microscopy

HeLa cells were seeded on 12-well slides (5 X 10^3 cells/well) and incubated with 10 μg ml^{-1} ,chlorpromazine (CPZ), 1 μg ml^{-1} filipin, or 100 μM amiloride hydrochloride for 1 hr at 37 ºC to examine the effects of a membrane entry inhibitors. This was followed by incubation with 10 μg/mL of 35% w/w DOX-ZrP for 2h. Chlorpromazine, filipin, and amiloride were used to inhibit the clathrin-mediated endocytosis, caveolae-mediated, and macropinocytosis mediated endocytosis respectively. The cells were washed twice with PBS, harvested by scraping, suspended in lysis buffer, and then the

intracellular doxorubicin content was analyzed by fluorescence microscopy. Image acquisition and analysis was done using the Image J® program.

Results and Discussion

The ZrP nanoparticles were characterized using XRPD and TEM to reveal the successful intercalation of each of the drugs. The hexagonal, thin platelet-like shape with homogenous size distribution was monitored in each case. The X-ray diffractograms were discussed in detail in the previous chapter. In the case of the cisplatin intercalated materials the x-ray diffractograms show the formation of a new phase with an interlayer distance of ca. 9.3 Å at all loading levels. The d_{002} plane for the cisplatin intercalated material at 9.3 Å interlayer distance indicates the molecules are oriented with their square planar molecular plane inclined at 45˚ with respect to the ZrP plane.[8] The chloride ligand substitution by phosphate groups of the ZrP layers was further confirmed by microprobe and ICP-MS quantitative compositional analyses. **Table V-1** shows the results of microprobe and ICP-MS quantitative compositional analyses of the intercalation products at all loading levels. The chemical composition of the intercalation products indicates that the chloride concentration in the intercalation products is substantially lower than pristine cisplatin. **Figure V-3** shows the X-ray elemental distribution "mappings" obtained for the 1:1 vs. 5:1 intercalation products. The atomic distribution of Pt, P, and Cl in a 62 x 62 μm^2 section of the surface of the intercalation products reveals a marked difference in the Cl concentrations observed. This is further corroborated by the ICP-MS and microprobe results.

The intercalation of doxorubicin into θ-ZrP was carried out by direct ion-exchange (Scheme 1).The X-ray diffractogram peaks for the DOX loaded ZrP exhibits an interlayer spacing at 20.3Å. This indicates π-π interactions between the DOX molecules and the protonated amine groups between the DOX and the deprotonated phosphate groups of the layers.[158] This plays a crucial role in the packing arrangement within the layers. In the case of the lower loading levels (14% or 25%) it should be noted that there is a mixture of phases, where the peak corresponding to the alpha phase is still present. **Fig. V-4** shows scanning electron microscopy (SEM) and transmission electron microscopy (TEM) images of the DOX:ZrP intercalation product. The images show the characteristic platelet like hexagonal shape of the ZrP nanoparticles. The average particle size of DOX:ZrP nano-platelets is ~150 nm in diameter. The thickness of the particles increased from ca. 12 nm to ca. 32 nm due to the interlayer expansion post intercalation.

In Vitro Drug Release

Drug efficacy of the CisPt:ZrP and DOX:ZrP nanohybrids is strongly associated with the intracellular concentration of CisPt and DOX delivered by ZrP nanocarriers. The in vitro release experiments of DOX from DOX:ZrP nanoparticles and CisPt from CisPt:ZrP nanoparticles were investigated by the dialysis method with SBF (pH 7.4) and ALF (4.5) as a release medium. The SBF had the same ionic concentration of human plasma and ALF has the same ionic concentration as a lysosomal microenvironment. [210, 212] A brief animation scheme of the experimental design is illustrated in Figure V-5**.**

Molar Ratio	Chemical Formula	Pt:Cl ratios
1:10	$Zr(H_{0.99}PO_4)_2(Pt(NH_3)_2)_{0.12}Cl_{0.008}.0.3H_2O$	23:1
1:5	$Zr(H_{0.93}PO_4)_2(Pt(NH_3)_2)_{0.14}Cl_{0.007}.0.3H_2O$	27:1
1:1	$Zr(H_{0.84}PO_4)_2(Pt(NH_3)_2)_{0.318}Cl_{0.010}.0.2H_2O$	31:1
5:1	$Zr(H_{0.86}PO_4)_2(Pt(NH_3)_2)_{0.286}Cl_{0.077}.0.5H_2O$	4:1

Table V-1: Molecular formula determinations for cisPt:ZrP at different loading levels based on microprobe and ICP-MS

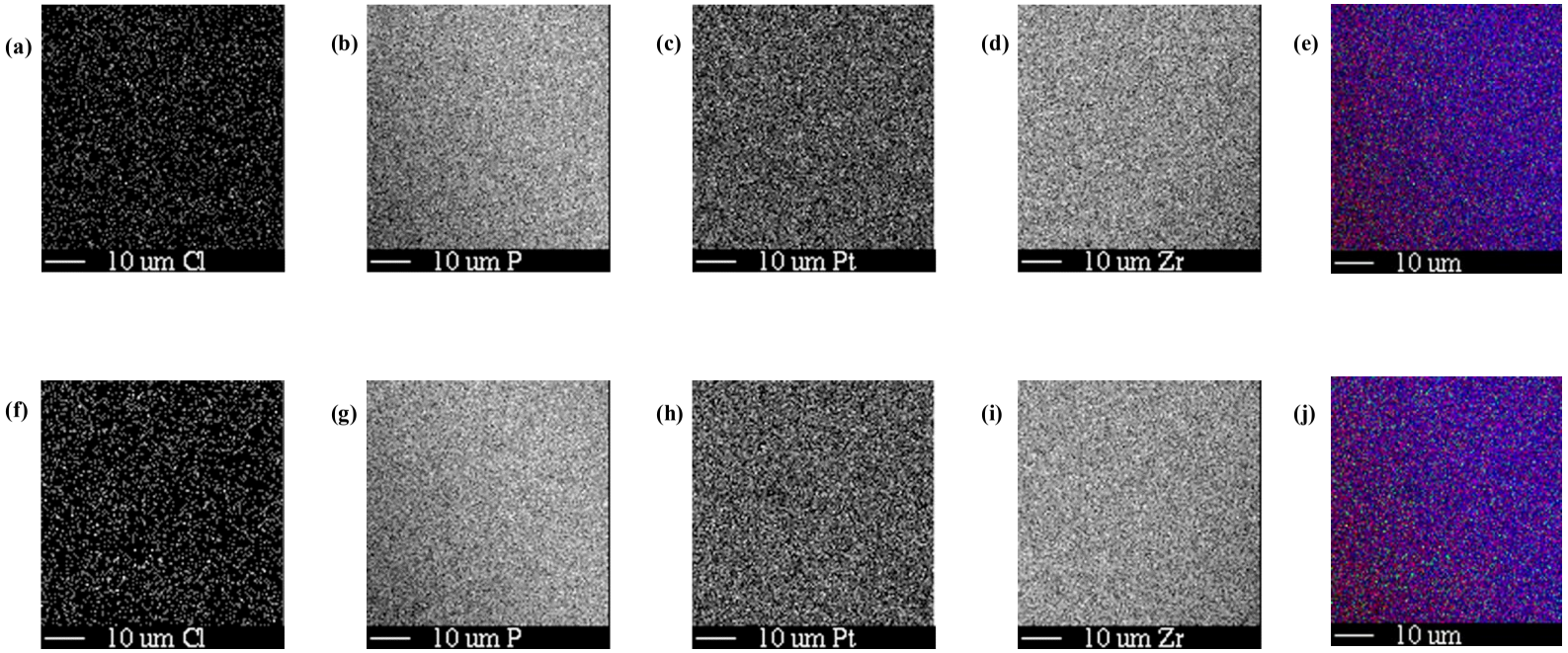

Figure V-3: X-ray elemental distribution maps for cisPt:ZrP for 1:1 (a) through (d) and 1:5 (e) through (i). The microprobe image composites X-ray maps were generated using the program Image J® by combining three 8-bit X-ray images into a false color 24-bit RGB image, where red was selected for Pt, blue for P, and green for Cl.

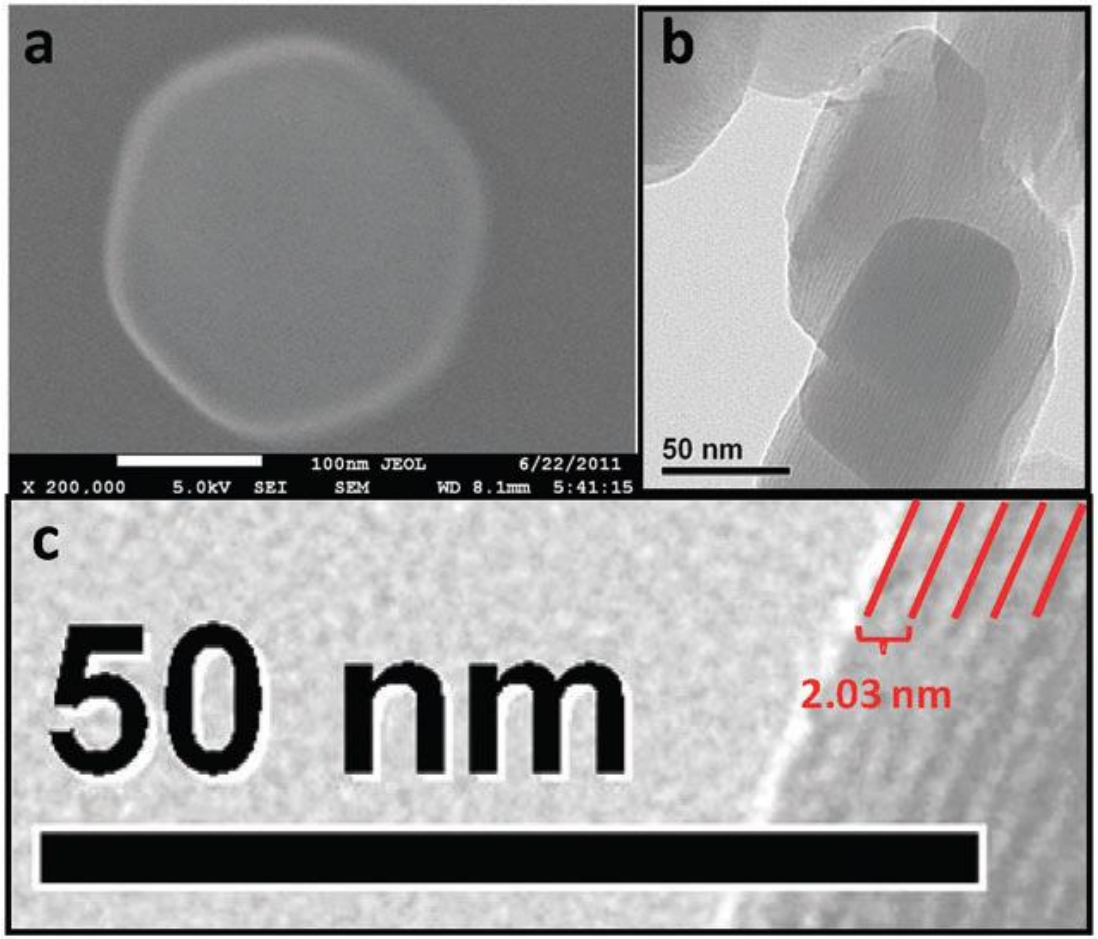

Figure V-4: SEM/TEM images of ZrP; SEM image of an α-ZrP nanoplatelets (a), TEM images of DOX:ZrP nanoplatelets tilted (b), zoom in of the TEM image (b) showing the layers and the interlayer distance (c). (Reference 158)

As shown in **Fig. V-6**, the release of DOX in the first day is roughly about 40% from both 14% and 25% loaded DOX:ZrP nanoparticles in SBF.[158] It is interesting to note that the release of Zr in the SBF environment for all loading levels of DOX:ZrP is negligible and hence a graph for the same has not been included. However in the ALF environment 43% of the DOX was released for the 14% loaded DOX:ZrP material and 15% of the DOX is release for the 25% loaded DOX:ZrP (**Figure V-7**). Simultaneously in the ALF environment at the 24 hour mark about 20% of the Zr for the 25% LDL DOX:ZrP and 25% of the Zr in the 14% LDL DOX:ZrP was released indicating the breakdown of the matrix allowing for the DOX to escape. Over a 10 day experiment period roughly a little under 40% of the ZrP matrix broke down to release the drug in the ALF environment. The drug however, goes through slow release and it took almost another 10 days to get to an 88% release from the 14% and it took about 14 days for the release of 80% DOX 25% loaded material. A slow release mechanism ensures the sustained DOX release for two weeks. Looking at the simultaneous Zr release shows that the delamination of the ZrP is a possible reason for the slow release mechanistically of the DOX. Additionally, ion exchange and drug diffusion may also be responsible. The delamination and break down of the ZrP material makes it an ideal drug delivery matrix. This will enable efficient renal clearance and drug dissemination. Interestingly, the 35% w/w loaded DOX:ZrP showed little to no release in both SBF and ALF (hence not shown in graphs). We hypothesize the tight packing of the DOX within the ZrP layers doesn't allow the solvent diffusion and the slow Zr break down prevents the release of the drug.

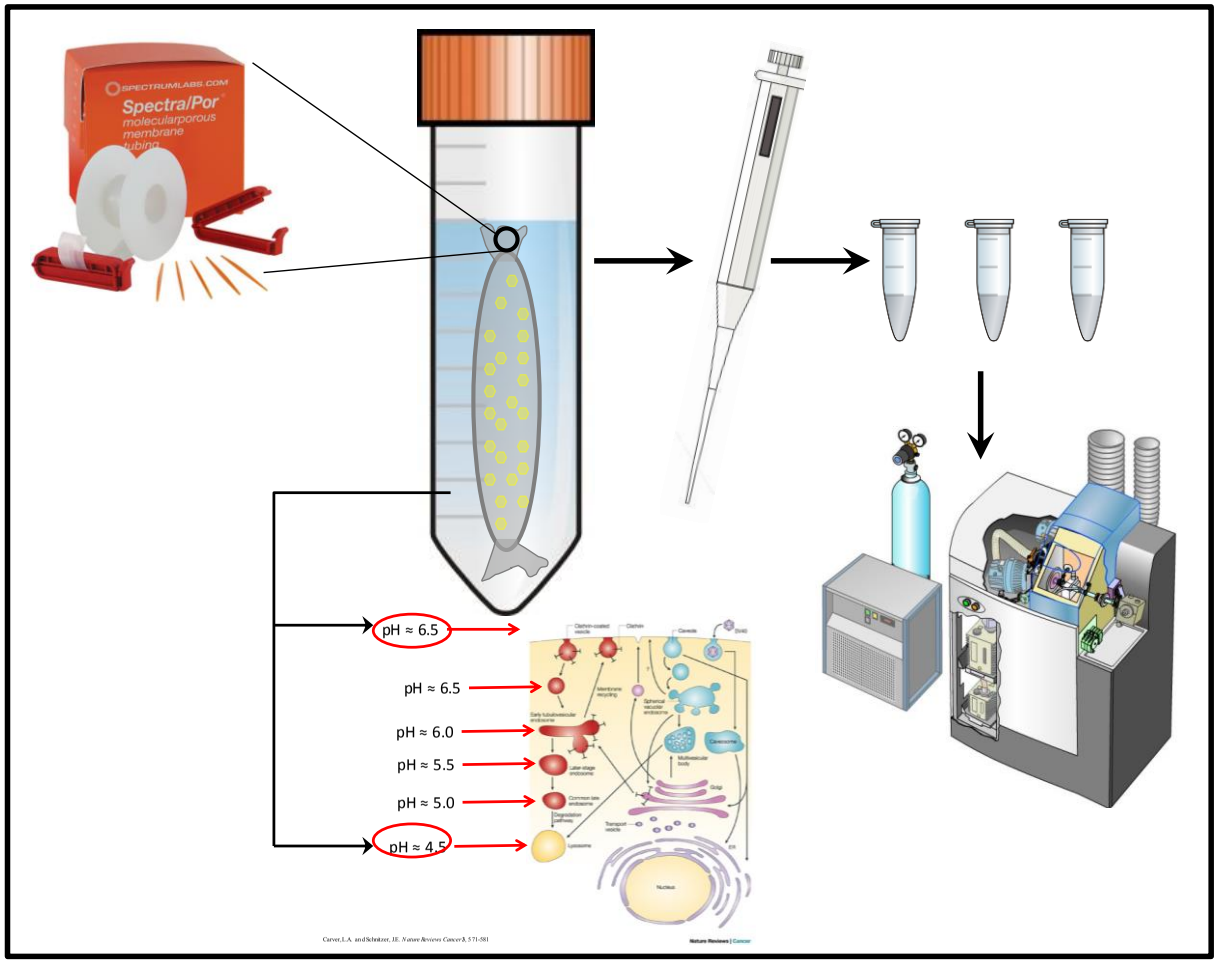

Figure V-5: Schematic of dialysis study setup for drug release experiments. 50 µL samples were taken from the external volume of the Eppendorf tubes. The samples collected are analyzed using ICP-MS.

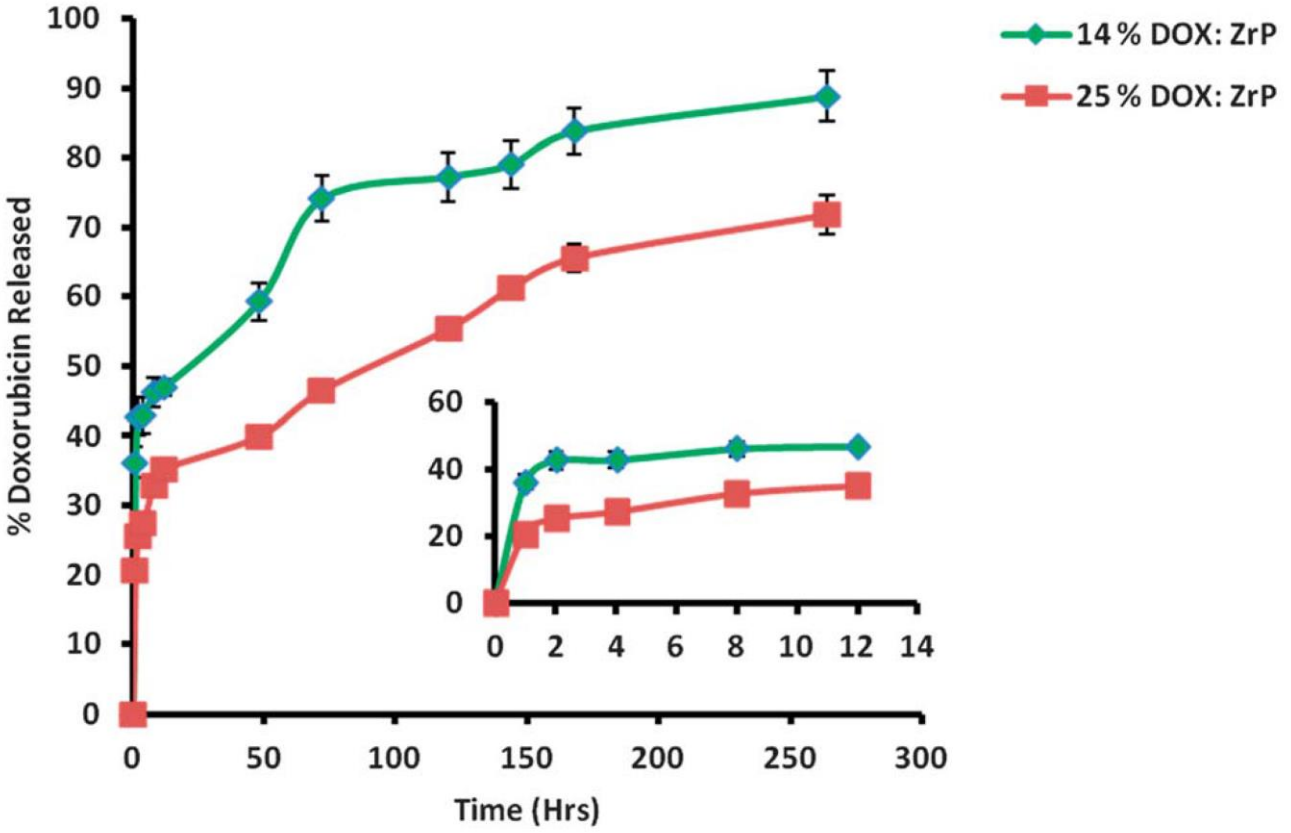

Figure V-6: In vitro release profile of doxorubicin (DOX) from different loading levels of DOX:ZrP nanoparticles Drug release study was performed at 37ºC in simulated body fluid of pH 7.4, under shaking (100 rpm). Mean $\pm$ SD, n = 3. (From reference 158)

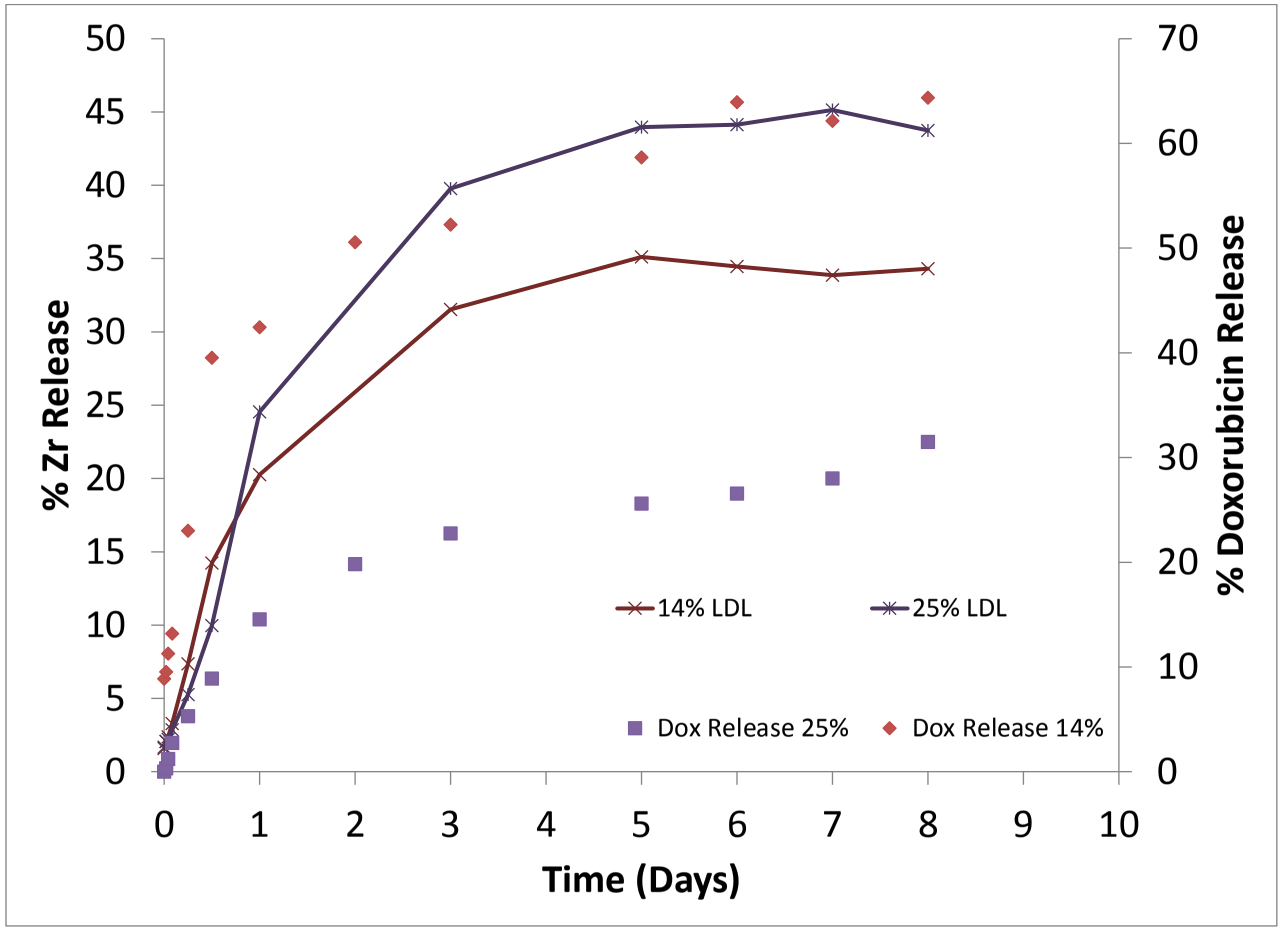

Figure V-7: In vitro release profile of doxorubicin (DOX) and Zr^{91} from different loading levels of DOX:ZrP nanoparticles. Drug release study was performed at 37ºC in artificial lysosomal fluid of pH 4.5

With respect to the DOX:ZrP homogeneity from the previous studies it was established that the 1:1 or 35% w/w material is the most homogenous with a 91% surface homogeneity. We hypothesize that overly homogenous and tightly packed nanoparticles don't afford the best drug release and thus may not be the ideal loading level for the most efficient drug dissemination. This is an important discovery relating to the nature of drug-nanoparticle hybrids. Additionally, it is clear that the ZrP matrix preferentially breaks down in the lower pH ALF environment vs the SBF environment. The overall DOX release in SBF is quite comparable with that of the ALF indicating that diffusion or ion exchange over material degradation and subsequent release drives the DOX-ZrP release mechanism.

For the cisplatin loaded ZrP the release was monitored via ICP-MS by observing the platinum (Pt^{195}) and (Zr^{91}) signals over time (**Figure V-8**). At pH = 7.4 under the SBF condition the Pt release takes place within the first 12 h. It is only between 2% to 3% of the theoretical maximum. The release profile reaches a plateau after the first 12 h that is maintained for several days. The Pt released under these conditions is assigned to the accessible platinum on the surface and edges of the ZrP nanoparticles, not from the Pt intercalated complexes within the ZrP layers. The slow release of cisplatin at pH = 7.4 under SBF conditions is highly desirable in order to avoid the general administration of the drug and the many side effects related to this phenomena. On the other hand, rapid release of the Pt complex from the ZrP galleries at low pH is desirable since it approaches the typical pH of the acidic environment of the tumor endosomes, and lysosomes which was discussed in detail previously.[213, 214]

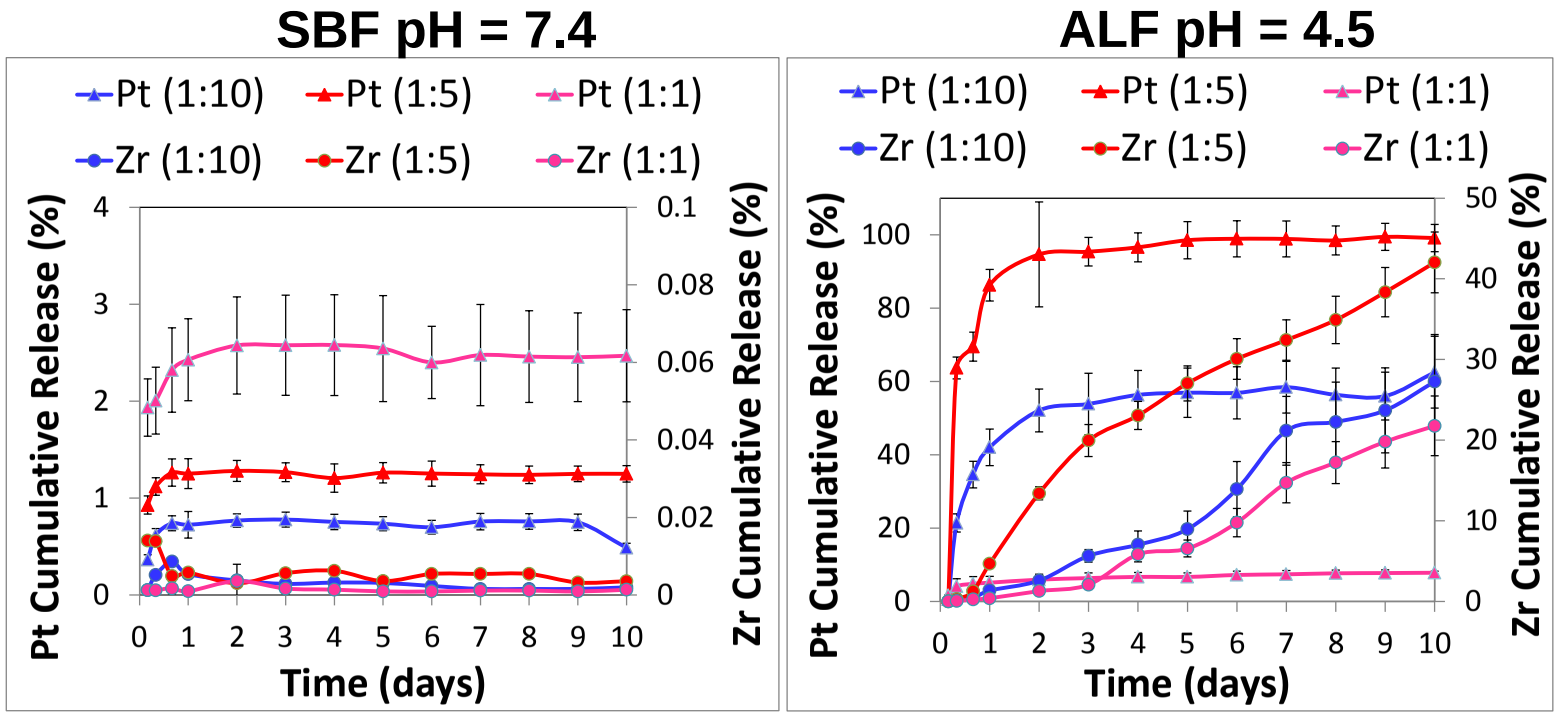

Figure V-8: In-vitro platinum and zirconium release from cisPt:ZrP nanoparticles (1:1, 1:5 & 1:10 molar ratio) in SBF (A) and ALF (B) at pH 7.4 and 4.5 respectively. (Reference 8)

The release profile of the platinum complex from the ZrP nanoparticles under the pH = 4.5 ALF condition shows a much faster release, compared to the release in SBF (pH = 7.4), with almost 50% of release after the first 12 hours for the 1:5 molar ratio. The release is faster for the 1:5 molar ratio sample than for the 1:10 and the 1:1 molar ratios samples. This difference can be explained by taking into account the structure of the cisPt@ZrP nanoparticles for each molar ratio. Furthermore, as previously discussed the material homogeneity for the 1:5 sample is ~54% in comparison with the 1:1 sample which has a much higher sample homogeneity ~94%. The empty galleries for the 1:5 sample allows for much easier solution diffusion in comparison with the 1:1 loaded samples.

The 1:1 molar ratio sample is a fully loaded material, where most of the platinum complexes are covalently bonded to the layers in a cross linked fashion, making the protonation of the phosphate to release the Pt complex and ligand exchange of the platinum complex more difficult due to the steric hindrance of the system. In the case of the cisPt@ZrP 1:10 molar ratio sample, the platinum complex is less hindered, but is more diluted throughout the whole nanoparticle, making the release slower. In the case of the cisPt@ZrP 1:5 molar ratio sample there is a higher concentration of the Pt complex than the 1:10 molar ratio sample but less hindrance than in the 1:1 molar ratio sample because the system has not reached saturation, producing a faster release. The hydrolysis of the Zr atoms from the ZrP layers was also monitored while the release of Pt takes place in the ALF. The release of Zr atoms into the medium is indicative of hydrolysis of the particles, which is important for the clearance of the inorganic

nanoparticles from the body. The hydrolysis of the nanoparticles produced a soluble Zr salt and inorganic phosphate that can be reused in the biological system. **Figure V-8B** shows the release of Zr atoms with time. The release of the Zr is slower in comparison to the release of the Pt from the particle, which implies that the hydrolysis of the platinum complex is faster than to the hydrolysis of the nanoparticles under lysosomal conditions.

The reason for the difference in release profiles for DOX loaded ZrP vs CisPt loaded ZrP can be attributed to the fundamental differences in their intercalation mechanism. While DOX is sequestered in ZrP through direct ion exchange the intercalation mechanism for cisplatin is based on the covalent bonding of cisplatin. The chloride ligand substitution by phosphate groups of the ZrP layers allows for a more stable structure and better bonding.

Recent studies show that burst release profiles of drug-loaded polymeric nanoparticles and liposomes are undesirable due to increased local and systemic toxicity, low drug availability at the tumor site, and consequently a reduced therapeutic effect.[215] Therefore, the slow release profile of cisPt@ZrP may be pharmacologically advantageous by increasing the time of exposure of the tumor cells to the drug. Due to the enhanced permeability and retention effect (EPR) when using ZrP nanoplatelets as carriers, cisplatin will be released mainly into the tumor cells which could result in lower systemic toxicity to the patient.

Uptake Mechanism

Drug efficacy of the DOX-ZrP nanohybrid is strongly associated with the intracellular concentration of DOX delivered by ZrP nanocarriers. To further investigate the possible mechanism responsible for the DOX-ZrP uptake, the uptake modulation after the inhibition of different endocytic pathways was evaluated. There are several possible endocytic pathways for internalizing ZrP nanoparticles, such as clathrin-mediated endocytosis, caveolae-mediated endocytosis, and macropinocytosis-mediated endocytosis (**Figure V-9**).[216] We determined the specific endocytic pathway used by the ZrP nanoparticles for membrane entry by confocal microscopic studies. Since doxorubicin is fluorescent, this particular aspect of the study focuses solely on DOX-ZrP nanoparticles.

HeLa cells were pre-incubated with endocytosis inhibitors for 1 h at 37 ºC followed by treatment with DOX and 35% LDL DOX-ZrP at 10μM concentration for the sake of simplicity for 2 h. The particle sizes of ZrP and DOX:ZrP were measured by transmission electron microscopy (TEM) and dynamic light scattering method. The samples used were constantly agitated to avoid agglomeration. Endocytosis pathways are subdivided into categories based on the size of the molecules being internalized. Chlorpromazine, filipin, and amiloride were used to inhibit the clathrin-mediated endocytosis, caveolae-mediated one, and macropinocytosis, respectively. The amount of intracellular DOX was captured using confocal microscopy and Image J to quantify the images captured. As shown in **Fig. V-10**, the uptake amount of DOX was modulated by shutting down each endocytotic pathway one by one to narrow down which mechanism

is the most actively involved. For the clathrin mediated endocytosis the portals for the endocytic entry of foreign molecules the vesicles are approx. 100 nm in diameter. Caveolae are small (approx. 50 nm in diameter). Macropinocytosis which is a highly conserved endocytic process by which extracellular fluid and its contents are internalized into cells through large, heterogeneous vesicles approximately 0.5–5 μm in diameter known as macropinosomes.[217]

The particle size for the DOX:ZrP materials is approximately 175 $\pm$ 5 nm according to the DLS and TEM analysis. Based solely on size the macropinocytosis endocytotic pathway best fits the need to internalize the DOX:ZrP material. The confocal data is in agreement since the caveolae and clathrin shutdown pathways don't affect the DOX:ZrP uptake. However the macropinocytosis shut down pathway significantly diminishing the nanoparticle uptake just as hypothesized.

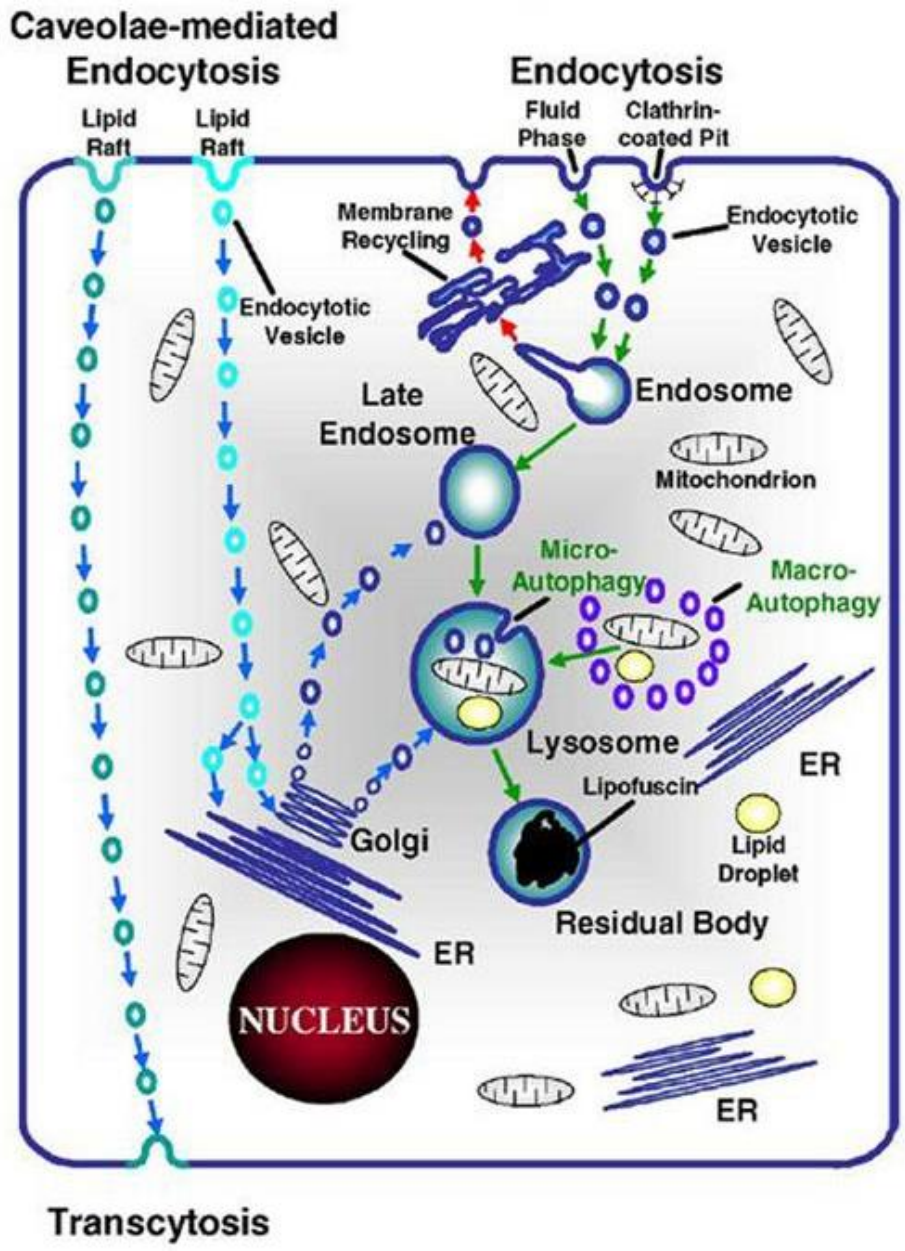

Figure V-9: The various endocytotic pathways that maybe applicable for the uptake of drug loaded nanoparticles. (Reference 216)

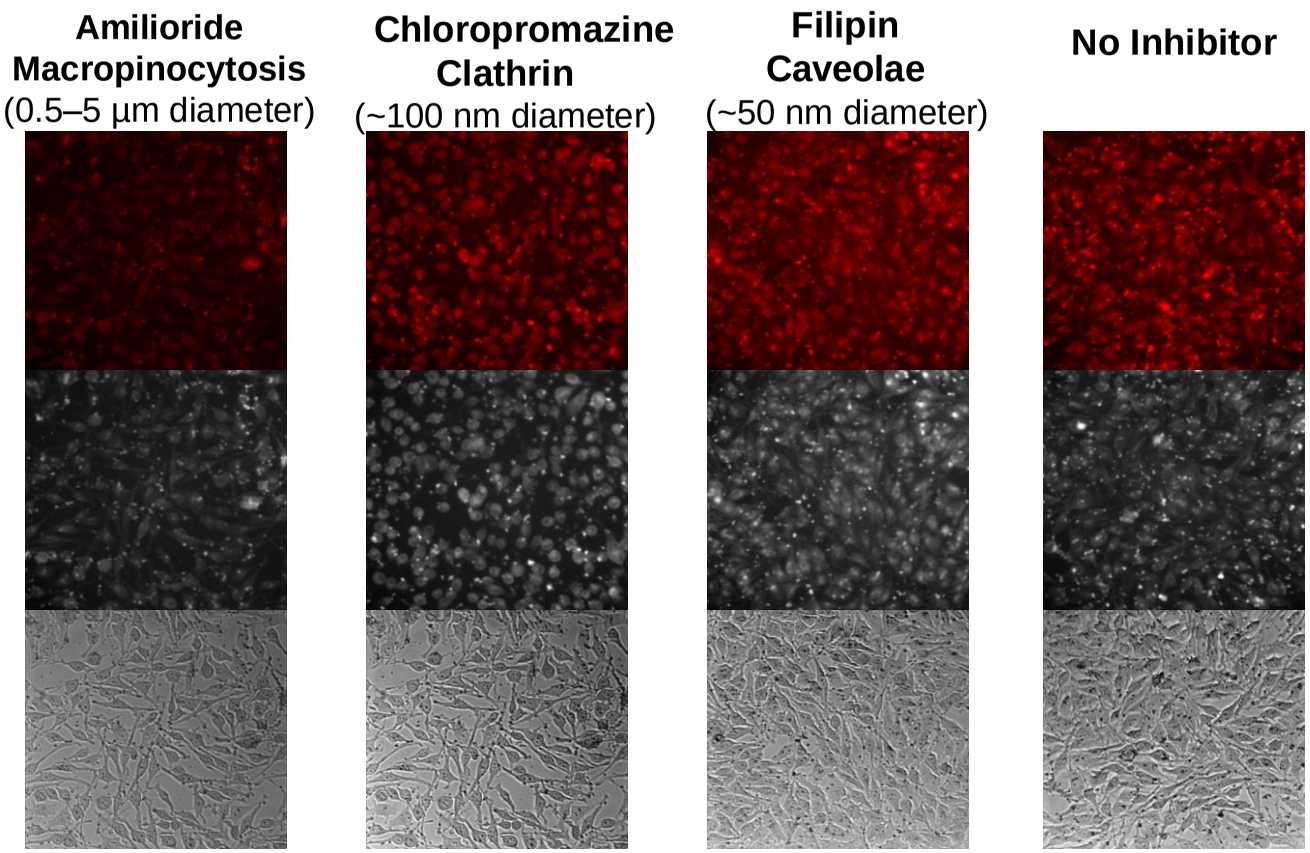

Figure V-10: HeLa cells were pre-incubated with endocytosis inhibitors for 1 h at 37 C followed by treatment with DOX-ZrP for 1 h. CPZ, filipin, and amiloride were used to inhibit the clathrin-mediated endocytosis, caveolae-mediated one, and macropinocytosis, respectively. The top most row of images represent the confocal images showing doxorubicin. The lower images are bright field microscopy images for the same.

Conclusions

The in vitro studies suggest that application of ZrP nanoparticle mediated drug transport as exemplified by DOX:ZrP and cisPt:ZrP, is highly promising for cancer chemotherapy. This chapter discussed the synthesis and characterization of ZrP nanoparticles, and loaded DOX and CisPt in the nanoplatelets. The ZrP nanoparticles are not toxic to normal as well as malignant human cells. The ZrP particles can intercalate high loads of drugs and sustain their release. In the case of CisPt:ZrP samples the *in vitro* release of the Pt(II) complex is observable upon the introduction of a pH stimulus. We also demonstrate that the uptake mechanism of DOX-ZrP in HeLa cells was mediated by the macropinocytosis-mediated endocytic pathway.

CHAPTER VI

CONCLUSIONS AND FUTURE DIRECTIONS

Summary

Drug delivery vehicles represent an important field of research that have tremendous potential to improve upon the therapeutic formulations of several current drugs. The opportunities for advancements in the field are numerous and still being discovered. The work of this dissertation aims to present significant improvements in four specific areas of inorganic layered material drug delivery technology:

1. The surface modification of zirconium phosphate nanoplatelets for custom designed surfaces that can be functionalized for a variety of applications, including but not limited to drug delivery
2. Establishing a novel technique to discover drug:ZrP nanohybrid homogeneity using secondary ion mass spectrometry (SIMS).
3. The delivery of anticancer therapeutics using robust inorganic layered framework, ZrP to establish a direct correlation of anticancer drug-ZrP nanohybrid homogeneity with *in vitro* drug release efficiency
4. The uptake mechanism of DOX:ZrP nanohybrids in HeLa cells was mediated by the macropinocytosis-mediated endocytic pathway to provide insights in identifying their organelle and molecular targets.

The results presented here show significant advancements in the area of inorganic layered frameworks for drug delivery. While polymeric drug delivery agents have been well investigated, the realm of inorganic material drug delivery is still relatively new. Adding to the drug delivery vehicle toolkit available to researchers and clinicians, these techniques can aid in overcoming the difficulties in anticancer therapeutics as well as having a broader impact on the field of drug delivery as a whole. The following sections will reiterate the important conclusions presented by this work and introduce a novel new technique to monitor non fluorescent CisPt:ZrP nanohybrids within cellular milieu without fluorescent tags.

Future Directions

In the past decade significant progress has been made in the imaging of chemical species within intact cells using secondary ion mass spectrometry, including the simultaneous mapping of subcellular elemental and molecular species along with intrinsic membrane-specific cellular markers.[218] The method presented in this chapter discusses the future of specimen preparation and chemical imaging of cell interiors providing the foundation for obtaining 3D molecular maps of small molecule distribution within unstained HeLa cells. Knowledge of the spatial distributions of elements within cells is potentially important for understanding the delivery and release of drug:ZrP nanohybrids. Since fluorescence imaging is restricted to natively fluorescent materials or requires fluorescent tagging, using SIMS based imaging techniques provides unique opportunities for achieving

simultaneous detection of multiple, unlabeled cellular components. This chapter covers some of the challenges in developing sample preparation/preservation protocols that maintain the chemical integrity of the cells. This chapter presents an approach to accomplish the aim of single cell mass spectrometric imaging for specific drug delivery target detection.

The instrumentation used to carry out these experiments is housed at the National Institute of Standards and Technology (NIST; Gaithersburg, Maryland). The instrumentation is described in detail elsewhere.[218] Briefly, the secondary ion mass spectrometer uses a Ga^+ focused ion beam (FIB) to mill flash frozen HeLa cells. The exposed cellular interiors are interrogated by SIMS. The information obtained from each targeted pixel can be used to extract characteristic elemental and molecular ion information for the desired polarity en route to a microchannel plate detector. Element specific maps are generated for individual chemical species. A computational algorithm identifies distinct cellular and molecular fragment localizations. Overlays of these localizations produces detailed molecular maps of molecular chemistries within and around single cells.[218]

Sample Preparation Procedure

Strategy for nanoscale compositional mapping of biological molecules in mammalian cells is illustrated in **Figure VI-1**. HeLa cells are (1) grown on silicon substrates immersed in media, (2) plunge-frozen in liquid ethane, and (3) freeze-dried and gently rinsed with mass spectrometry-grade water. The step-wise

procedure that was developed in conjunction with National Institute of Health (NIH) and NIST is described below.

1. HeLa cells were grown on sterilized silicon wafers. Each silicon substrates is sterilized via the following rinses: 70 % ethanol for 5 minutes, doubly distilled water for 10 minutes, 100 % ethanol for 5 minutes, and HPLC-grade water for 10 minutes.
2. All preps were performed in a process free of contamination from poly(dimethylsiloxane) (PDMS), a common surface contaminant towards which the SIMS analysis are sensitive. After allowing the silicon wafers to air dry (in a tissue culture hood), silicon pieces were cut with a diamond scribe from 5 mm x 5mm pre-diced squares to approximately 2 mm x 2 mm pieces and placed in cell wells.
3. HeLa cells were grown in RPMI media, a general purpose media with a broad range of applications for mammalian cells containing 10 % fetal bovine serum (FBS) overnight. HeLa cells were split and seeded into the wells and allowed to culture overnight.

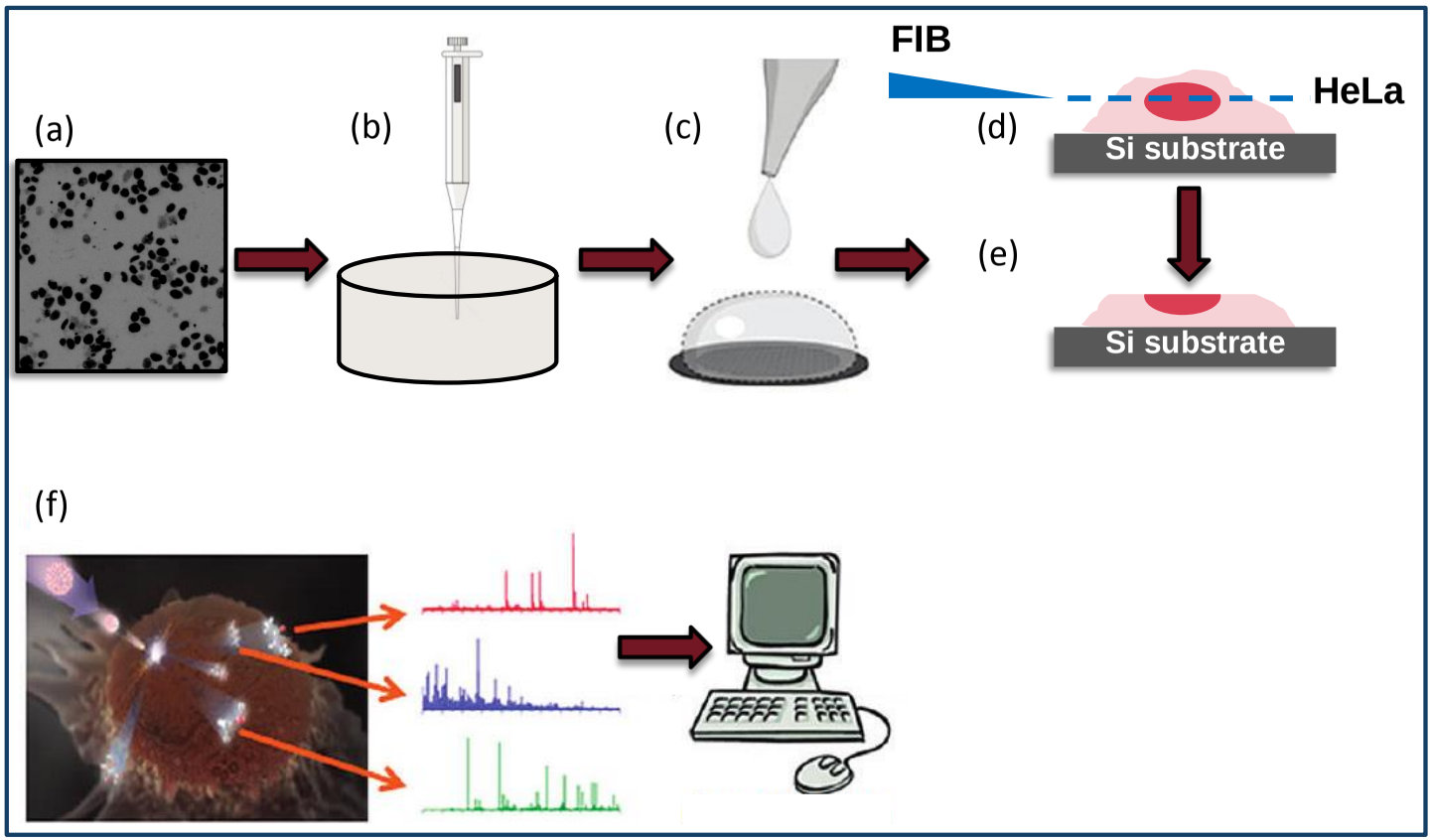

Figure VI-1: Strategy for nanoscale compositional mapping of biological molecules in HeLa cells. They are (a) grown on silicon substrates immersed in media, (b) plunge-frozen in liquid ethane, and (c) freeze-dried and gently rinsed with mass spectrometry-grade water. A tangentially directed focused ion beam (FIB) is (d) used to mill the top of the cells, which (e) exposes the cell interior. (f) Secondary ion mass spectrometry (SIMS) induced by primary ion probes (Modified from reference 218)

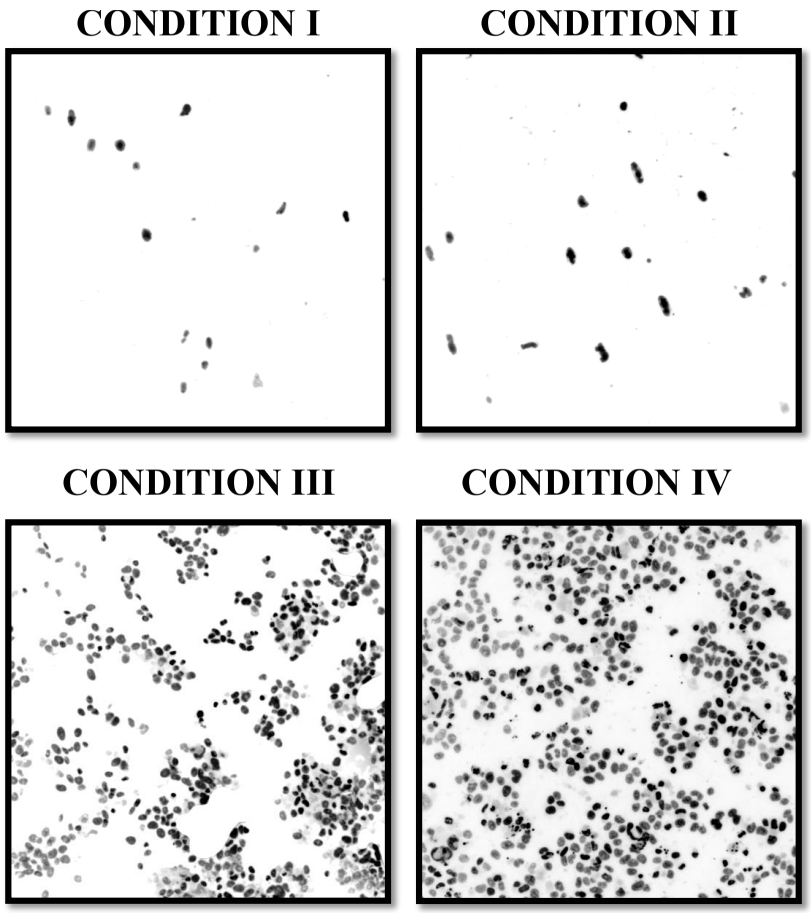

Figure VI-2: Microscopy images of HeLa cells grown on sterilized silicon wafers using different growth conditions. 20 µL cell populated media is dropcast onto each Si wafer for 30 min. **Condition I**: Fresh media droplet used post adherence of cell populated media. **Condition II**: No droplet used post cell adherence **Condition III**: Media with cells and no droplet **Condition IV**: Media with cells with cell populated droplet

4. Each of the wafers had HeLa cells grow onto them at a density of 10^6 cells/ml with roughly ~20uL of the cell solution being used to drop cast onto the wafer for 30 min to allow attachment followed by addition of more cell populated media. Different growth conditions were tested **Figure VI-2.**

5. Once the cells were confluent (2 days post growth) the CisPt:ZrP material was introduced in each cell well at the specified concentration. (**Table VI-1**)

   Six hours post incubation with the drug/sample the cells were washed with phosphate buffer with 10% bovine serum albumin (BSA). This step was done to get rid of various components of cell culture media, so that the background spectra from SIMS would be clean.

6. Post washing the cells were lightly rinsed with Millipore water and the excess liquid wicked away with filer paper before they were quickly plunge frozen in liquid ethane

7. Post plunge freezing they were stored in N_2 dewars until they were freeze dried in a Balzers instrument at 2 X 10^5 Barr for 2 hours at -100°C after which the samples were allowed to revert to STP by slow leaking of the vacuum over time. This was done over roughly 5 hours. The instrumentation used in this process was a Balzers freeze-fracture electron microscope **(Figure VI-3).**

Sample	Concentration
CisPt-ZrP (1:5)	10,000 nM
CisPt-ZrP (1:5)	1000 nM
CisPt-ZrP (1:5)	100 nM
Cisplatin	10,000 nM
Cisplatin	1000 nM
Cisplatin	100 nM
ZrP	1000 nM
ZrP	100 nM
BLANK	N/A

Table VI-1: Incubation concentrations used in each experiment. A 12 cell well was used for the experiment.

8. Resulting freeze-dried cells on silicon pieces were gently rinsed in a small volume of HPLC-grade water for 5 seconds, and the water wicked away with filter paper quickly. This final step removes the majority of salt contamination on the silicon chip while maintaining the membranous structure of the cell.

9. To wash the wafer allow a drop of clean water to touch the surface (not even fall on the surface, just contact it) for a few seconds, then wick away to any chosen side (don't touch the top face) by holding the Si on its side with a pair of tweezers and letting it rest on a whatman filter paper.

10. At this stage the samples are ready for storage and transport since the cells in question are unanimated and vacuum ready.

The preliminary results from the first round of experiments were presented in **Figure VI-4**. The images in **Figure VI-4** depict time-of-flight (TOF)-SIMS compositional maps of several individual unstained HeLa incubated with CisPt:ZrP following plunge-freezing in liquid ethane and lyophilization to remove vitrified water. Both the total ion image (i.e., sum of all elemental and molecular ion intensities obtained in each pixel) and an overlay of the phosphatidylcholine headgroup (m/z 184) from the cell surface and extracellular sodium (m/z 23) are shown in **Figure VI-4 a,&b**. Parts c and d of **Figure VI-4** display the individual ion-specific maps of the drug substrate, ZrP localized with part of the lipid head group (CN^-) and the drug CisPt, respectively.

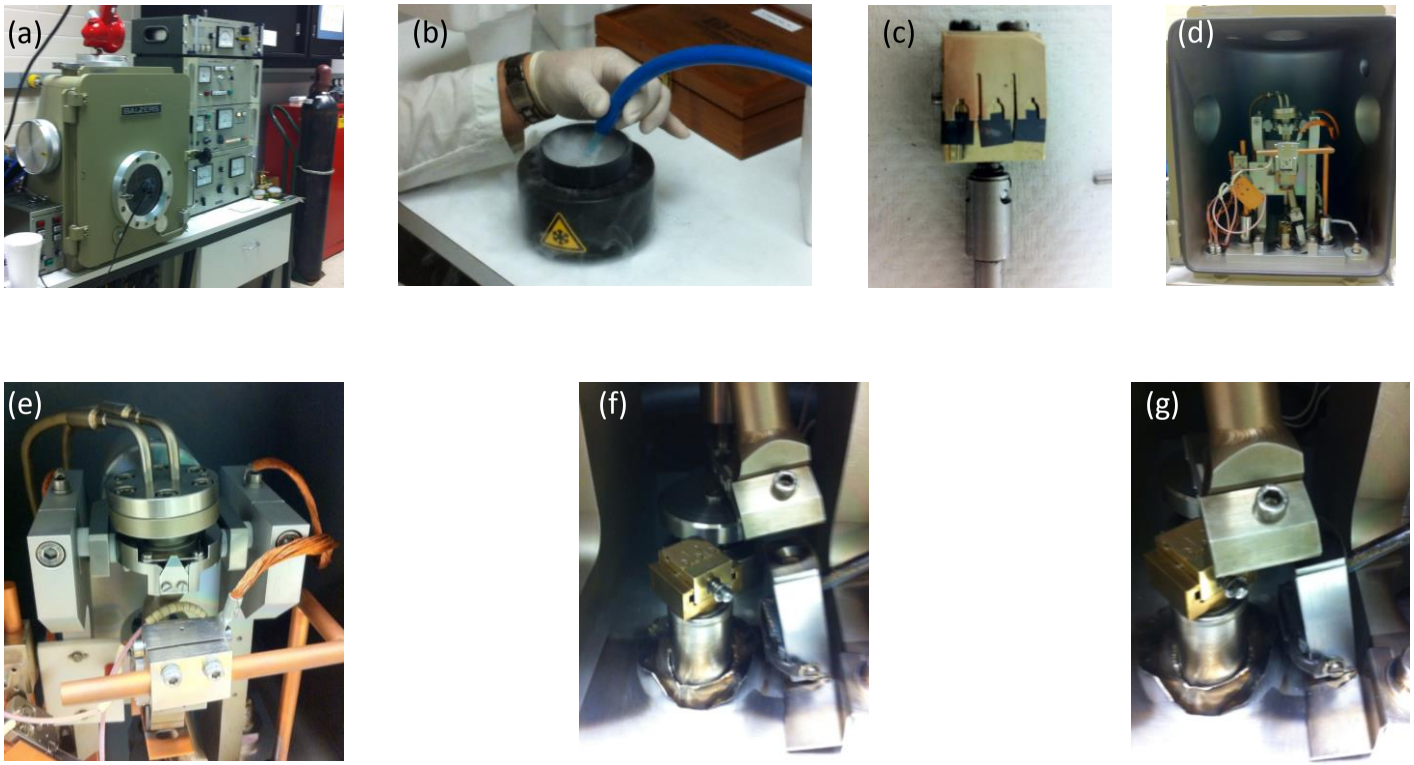

Figure VI-3: Figure: (a) Balzers freeze facture instrument (b) Ethane is liquefied using liquid N_2 in a dewar with a metal receptacle (c) Custom Si wafer holder attached to vacuum introduction rod (d) Inside of the Balzers freeze dryer chamber (e) Thermocouple attached to the metal knife to regulate temperatures (f) Sample holder with metal knife hovering to the side prior to freeze drying (g) The knife is hovered over the sample holder during the dehydration process to create a temperature difference between the sample stage and knife which are maintained at different temperatures under vacuum.

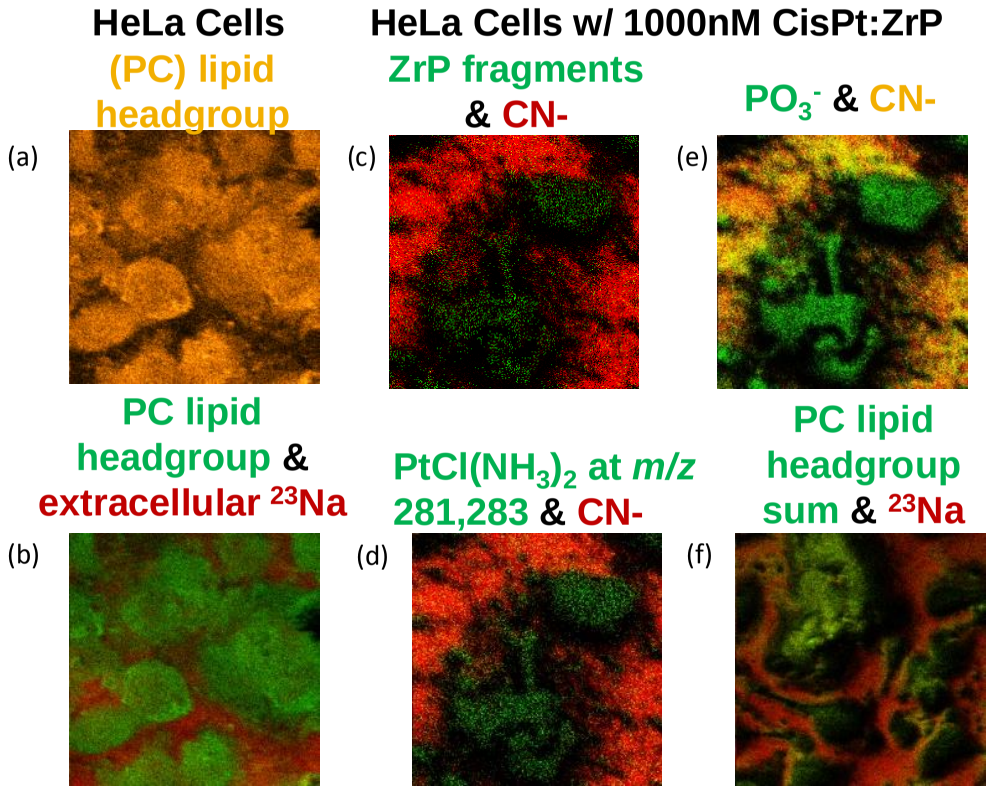

Figure VI-4: Compositional mapping of HeLa cells outer lipid membrane at submicrometer resolution. (a)phosphatidylcholine head group(PC -m/z 184) from the cell surface (b) overlay of the PC head group from the cell surface and extracellular sodium (m/z 23) (c) overlap of administered nanomaterial substrate ZrP & lipid fragments (d) overlay of CisPt & lipid fragments (e) Overlay of phosphate salt from the ZrP substrate and lipid fragments (f) overlap of lipid rafts from cellular rupture and extracellular salt (Na23)

It is interesting to note that the ZrP and CisPt are also localized within the HeLa cells. The colocalization of the lipid signal to the periphery of each cell is indicative of chemically intact membranes. Additionally the observance of sodium on the cell substrate more so than the cell surface serves as verification for the sample preparation process. If the cells rupture during cell preparation, the lipid signal is homogeneous due to the formation of lipid raft like structures across the imaging area and not confined to the cell shapes (**Figure VI-4f**).

Final Remarks

This study lays the basic foundation for sample preparation needs in looking at drug metabolites within single cellular environments. While this study does open up possibilities for several non-fluorescent drugs and metabolites the complexity involved during sample preparation still requires more calibration for consistency. Because of the complexity of the ionic species desorbed from within and around single cells, as well as the difficulty in maintaining the chemical integrity of the cellular targets, care must be taken to have the proper sample preparation, sample analysis conditions that represent the optimum trade-off of spatial resolution and mass resolution.[218] This is an important direction for the future of discoveries in inorganic drug loaded nanomaterials. It will enable better analytical understanding of both the materials that play host for drug delivery as well as elevate the understanding of future delivery systems within cellular milieu. The next step in this work should be the introduction of a mouse model to test the efficacy of the inorganic layered materials in drug delivery applications. While *in-*

vitro work does provide a very useful snapshot of expected immunoresponse, *in vivo* work will take this novel research to the next level.

REFERENCES

1. Kaschak, D. M.; Johnson, S. A.; Hooks, D. E.; Kim, H.-N.; Ward, M. D.; Mallouk, T. E. *Journal of the American Chemical Society* **1998,** 120, (42), 10887-10894.

2. McCreery, R. L. *Chemistry of Materials* **2004,** 16, (23), 4477-4496.

3. Díaz, A.; Mosby, B. M.; Bakhmutov, V. I.; Martí, A. A.; Batteas, J. D.; Clearfield, A. *Chem Mater* **2013,** 25, (5), 723-728.

4. Adams, D. M.; Brus, L.; Chidsey, C. E. D.; Creager, S.; Creutz, C.; Kagan, C. R.; Kamat, P. V.; Lieberman, M.; Lindsay, S.; Marcus, R. A.; Metzger, R. M.; Michel-Beyerle, M. E.; Miller, J. R.; Newton, M. D.; Rolison, D. R.; Sankey, O.; Schanze, K. S.; Yardley, J.; Zhu, X. *The Journal of Physical Chemistry B* **2003,** 107, (28), 6668-6697.

5. Chechik, V.; Crooks, R. M.; Stirling, C. J. M. *Advanced Materials* **2000,** 12, (16), 1161-1171.

6. Gooding, J. J. *Electroanalysis* **2008,** 20, (6), 573-582.

7. Gooding, J. J.; Mearns, F.; Yang, W.; Liu, J. *Electroanalysis* **2003,** 15, (2), 81-96.

8. Diaz, A.; Gonzalez, M. L.; Perez, R. J.; David, A.; Mukherjee, A.; Baez, A.; Clearfield, A.; Colon, J. L. *Nanoscale* **2013**.

9. Diaz, A. Structural Characterization of Bioactive Species Intercalated into Zirconium Phosphate for Drug Delivery Applications. Dissertation, University of Puerto Rico, San Juan 2010.

10. Díaz, A.; David, A.; Pérez, R.; González, M. L.; Báez, A.; Wark, S. E.; Zhang, P.; Clearfield, A.; Colón, J. L. *Biomacromolecules* **2010,** 11, (9), 2465-2470.

11. Diaz, A.; Saxena, V.; Gonzalez, J.; David, A.; Casanas, B.; Carpenter, C.; Batteas, J. D.; Colon, J. L.; Clearfield, A.; Delwar Hussain, M. *Chem Commun* **2012,** 48, (12), 1754-1756.

12. Vilan, A.; Yaffe, O.; Biller, A.; Salomon, A.; Kahn, A.; Cahen, D. *Advanced Materials* **2010,** 22, (2), 140-159.

13. Har-Lavan, R.; Ron, I.; Thieblemont, F.; Cahen, D. *Appl Phys Lett* **2009,** 94, (4).

14. Willner, I. *Science* **2002,** 298, (5602), 2407-2408.

15. Flood, A. H.; Ramirez, R. J. A.; Deng, W.-Q.; Muller, R. P.; Goddard III, W. A.; Stoddart, J. F. *Australian Journal of Chemistry* **2004,** 57, (4), 301-322.

16. Liu, C.-j.; Burghaus, U.; Besenbacher, F.; Wang, Z. L. *ACS Nano* **2010,** 4, (10), 5517-5526.

17. Rao, C. N. R.; Biswas, K. *Annu Rev Anal Chem* **2009,** 2, 435-462.

18. Clearfield, A.; Stynes, J. A. *Journal of Inorganic & Nuclear Chemistry* **1964,** 26, (1), 117-129.

19. Rivera, E. J.; Barbosa, C.; Torres, R.; Rivera, H.; Fachini, E. R.; Green, T. W.; Connick, W. B.; Colón, J. L. *Inorganic Chemistry* **2012,** 51, (5), 2777-2784.

20. Santiago-Berríos, M. E. B.; Declet-Flores, C.; David, A.; Borrero, S.; Vélez, M. M.; Díaz-Díaz, A.; Guadalupe, A. R.; Colón, J. L. *Langmuir* **2012,** 28, (9), 4447-4452.

21. Shi, S.; Liu, Q.; Zhang, X.; Hall, R. *RSC Advances* **2013,** 3, (22), 8254-8260.

22. Kijima, T. *Bulletin of the Chemical Society of Japan* **1982,** 55, (9), 3031-3032.

23. Clearfield, A.; Smith, G. D. *Inorganic Chemistry* **1969,** 8, (3), 431-436.

24. Clearfield, A.; Pack, S. P.; Troup, J. M. *Journal of Inorganic & Nuclear Chemistry* **1977,** 39, (8), 1437-1442.

25. G. Alberti, S. A., U. Costantino, P. Galli, M.A. Massucci, R. Platania, E. Torracca, 2 ed.; Magyar, Budapest, 1969; Vol. I, p P.1.

26. Clearfie.A; Duax, W. L. *Acta Crystall B-Stru* **1969,** B 25, 2658-&.

27. Clearfield, A. *Prog Cryst Growth Ch* **1991,** 21, 1-28.

28. Marti, A. A.; Rivera, N.; Soto, K.; Maldonado, L.; Colon, J. L. *Dalton Transactions* **2007**, (17), 1713-1718.

29. Martı´, A. A.; Paralitici, G.; Maldonado, L.; Colón, J. L. *Inorganica Chimica Acta* **2007,** 360, (5), 1535-1542.

30. Sun, L.; Boo, W. J.; Sue, H.-J.; Clearfield, A. *New Journal of Chemistry* **2007,** 31, (1), 39-43.

31. Pica, M.; Donnadio, A.; Capitani, D.; Vivani, R.; Troni, E.; Casciola, M. *Inorganic Chemistry* **2011,** 50, (22), 11623-11630.

32. Jacobson, A. J.; Nazar, L. F., Intercalation Chemistry. In *Encyclopedia of Inorganic and Bioinorganic Chemistry*, John Wiley & Sons, Ltd: 2011.

33. Alberti, G.; Costantino, U. *Journal of Molecular Catalysis* **1984,** 27, (1–2), 235-250.

34. Backov, R.; Bonnet, B.; Jones, D. J.; Roziere, J. *Chemistry of Materials* **1997,** 9, (8), 1812-1818.

35. Clearfield, A., *Inorganic Ion Exchange Materials. A* Boca Raton, 1982.

36. Rudolf, P. R.; Clearfield, A. *Inorganic Chemistry* **1989,** 28, (9), 1706-1710.

37. Poojary, D. M.; Clearfield, A. *Inorganic Chemistry* **1994,** 33, (17), 3685-3688.

38. Clearfield, A.; Duax, W. L.; Medina, A. S.; Smith, G. D.; Thomas, J. R. *The Journal of Physical Chemistry* **1969,** 73, (10), 3424-3430.

39. Clearfield, A. C., U., , *Layered Metal Phosphates and their Intercalation Chemistry. In Comprehensive Supramolecular Chemistry*. I ed.; Pergamon: New York, 1996; Vol. 7.

40. Martí, A. A.; Colón, J. L. *Inorganic Chemistry* **2003,** 42, (9), 2830-2832.

41. Sun, L. Y.; Boo, W. J.; Browning, R. L.; Sue, H. J.; Clearfield, A. *Chemistry of Materials* **2005,** 17, (23), 5606-5609.

42. Wang, H.; Liu, W.; Yao, W.; Zhang, K.; Zhong, J.; Chen, R. *Applied Surface Science* **2013,** 268, (0), 179-187.

43. Tindwa, R. M.; Ellis, D. K.; Peng, G.-Z.; Clearfield, A. *Journal of the Chemical Society, Faraday Transactions 1: Physical Chemistry in Condensed Phases* **1985,** 81, (2), 545-552.

44. Johnson, J. W. *Journal of the Chemical Society, Chemical Communications* **1980**, (6), 263-265.

45. Santiago, M. E. B.; Declet-Flores, C.; Díaz, A.; Vélez, M. M.; Bosques, M. Z.; Sanakis, Y.; Colón, J. L. *Langmuir* **2007,** 23, (14), 7810-7817.

46. Danjo, M.; Mizuguchi, Y.; Yagita, Y.; Kakiguchi, K.; Yanagida, T.; Tsuhako, M. *Bulletin of the Chemical Society of Japan* **1997,** 70, (12), 3011-3015.

47. Li, B.; He, J.; G. Evans, D.; Duan, X. *Applied Clay Science* **2004,** 27, (3–4), 199-207.

48. del Arco, M.; Gutiérrez, S.; Martín, C.; Rives, V.; Rocha, J. *Journal of Solid State Chemistry* **2004,** 177, (11), 3954-3962.

49. Rives, V.; del Arco, M.; Martín, C. *Journal of Controlled Release* **2010** 169, (1–2), 28-39.

50. Choy, J.-H.; Kwak, S.-Y.; Jeong, Y.-J.; Park, J.-S. *Angewandte Chemie International Edition* **2000,** 39, (22), 4041-4045.

51. Caraglia, M.; De Rosa, G.; Salzano, G.; Santini, D.; Lamberti, M.; Sperlongano, P.; Lombardi, A.; Abbruzzese, A.; Addeo, R. *Current Cancer Drug Targets* **2012,** 12, (3), 186-196.

52. Peer, D.; Karp, J. M.; Hong, S.; FaroKHzad, O. C.; Margalit, R.; Langer, R. *Nature Nanotechnology* **2007,** 2, (12), 751-760.

53. Ferrari, M. *Nat Rev Cancer* **2005,** 5, (3), 161-171.

54. Kjellstrand, C.; Borges, H.; Pru, C.; Gardner, D.; Fink, D. *T Am Soc Art Int Org* **1981,** 27, 24-30.

55. Schroede.Ha; Nason, A. P. *Clin Chem* **1971,** 17, (6), 461-465.

56. Aramouni, P.; Zebouni, E.; Tashkandi, E.; Dib, S.; Salameh, Z.; Almas, K. *J Contemp Dent Pract* **2008,** 9, (7), 41-8.

57. Chang, P. P.; Henegbarth, E. A.; Lang, L. A. *J Prosthet Dent* **2007,** 97, (6), 321-30.

58. Vigolo, P.; Fonzi, F. *J Prosthodont* **2008,** 17, (8), 621-6.

59. Uludag, B.; Sahin, V.; Ozturk, O. *Int J Prosthodont* **2008,** 21, (6), 509-10.

60. Tsukamoto, R.; Chen, S.; Asano, T.; Ogino, M.; Shoji, H.; Nakamura, T.; Clarke, I. C. *Acta Orthop* **2006,** 77, (3), 505-11.

61. Lappalainen, R.; Santavirta, S. S. *Clin Orthop Relat Res* **2005**, (430), 72-9.

62. Garvin, K. L.; Hartman, C. W.; Mangla, J.; Murdoch, N.; Martell, J. M. *Clin Orthop Relat Res* **2009,** 467, (1), 141-5.

63. Schadel, A.; Thun, G.; Stork, L.; Metzler, R. *ORL J Otorhinolaryngol Relat Spec* **1993,** 55, (4), 216-21.

64. Murisasco, A.; Baz, M.; Boobes, Y.; Bertocchio, P.; el Mehdi, M.; Durand, C.; Reynier, J. P.; Ragon, A. *Clin Nephrol* **1986,** 26 Suppl 1, S53-7.

65. Shaldon, S.; Beau, M. C.; Claret, G.; Deschodt, G.; Mion, H.; Oules, R.; Ramperez, P.; Mion, C. *Artif Organs* **1978,** 2, (4), 343-7.

66. Shapiro, W. B.; Schilb, T. P.; Porush, J. G. *Clin Nephrol* **1986,** 26 Suppl 1, S47-52.

67. Hansen, S. *Nephrol News Issues* **2006,** 20, (1), 43, 45.

68. Blumenkrantz, M. J.; Gordon, A.; Roberts, M.; Lewin, A. J.; Pecker, E. A.; Moran, J. K.; Coburn, J. W.; Maxwell, M. H. *Artif Organs* **1979,** 3, (3), 230-6.

69. Ronco, C.; Davenport, A.; Gura, V. *Nefrologia* **2011,** 31, (1), 9-16.

70. Davenport, A.; Gura, V.; Ronco, C.; Beizai, M.; Ezon, C.; Rambod, E. *Lancet* **2007,** 370, (9604), 2005-10.

71. Lee, D. B.; Roberts, M. *Clin Exp Nephrol* **2008,** 12, (3), 171-80.

72. Lee, D. B. N.; Roberts, M.; Bluchel, C. G.; Odell, R. A. *Asaio J* **2010,** 56, (6), 550-556.

73. Bringley, J. F.; Liebert, N. B. *Journal of Dispersion Science and Technology* **2003,** 24, (3-4), 589-605.

74. Decuzzi, P.; Lee, S.; Bhushan, B.; Ferrari, M. *Ann Biomed Eng* **2005,** 33, (2), 179-90.

75. Decuzzi, P.; Gentile, F.; Granaldi, A.; Curcio, A.; Causa, F.; Indolfi, C.; Netti, P.; Ferrari, M. *Int J Nanomedicine* **2007,** 2, (4), 689-96.

76. Ferrari, M. *Small* **2008,** 4, (1), 20-5.

77. Sanhai, W. R.; Sakamoto, J. H.; Canady, R.; Ferrari, M. *Nature Nanotechnology* **2008,** 3, (5), 242-4.

78. Tannock, I. F.; Rotin, D. *Cancer Research* **1989,** 49, (16), 4373-84.

79. Estrella, V.; Chen, T.; Lloyd, M.; Wojtkowiak, J.; Cornnell, H. H.; Ibrahim-Hashim, A.; Bailey, K.; Balagurunathan, Y.; Rothberg, J. M.; Sloane, B. F.; Johnson, J.; Gatenby, R. A.; Gillies, R. J. *Cancer Research* **2013,** 73, (5), 1524-35.

80. Bisht, S.; Maitra, A. *Wiley Interdisciplinary Reviews: Nanomedicine and Nanobiotechnology* **2009,** 1, (4), 415-425.

81. Stöckle, R. M.; Suh, Y. D.; Deckert, V.; Zenobi, R. *Chemical Physics Letters* **2000,** 318, (1–3), 131-136.

82. Group, E. A., Evans Analytical Group Sunnyvalle, CA, 2011.

83. Hainfeld, J. F. *Science* **1987,** 236, (4800), 450-3.

84. He, H.; Xie, C.; Ren, J. *Analytical Chemistry* **2008,** 80, (15), 5951-7.

85. Lee, C. Y.; Gong, P.; Harbers, G. M.; Grainger, D. W.; Castner, D. G.; Gamble, L. J. *Analytical Chemistry* **2006,** 78, (10), 3316-25.

86. May, C. J.; Canavan, H. E.; Castner, D. G. *Analytical Chemistry* **2004,** 76, (4), 1114-22.

87. Whetten, R. L.; Khoury, J. T.; Alvarez, M. M.; Murthy, S.; Vezmar, I.; Wang, Z. L.; Stephens, P. W.; Cleveland, C. L.; Luedtke, W. D.; Landman, U. *Advanced Materials* **1996,** 8, (5), 428-433.

88. Jimenez, V. L.; Georganopoulou, D. G.; White, R. J.; Harper, A. S.; Mills, A. J.; Lee, D.; Murray, R. W. *Langmuir* **2004,** 20, (16), 6864-70.

89. Belu, A. M.; Davies, M. C.; Newton, J. M.; Patel, N. *Anal Chem* **2000,** 72, (22), 5625-5638.

90. John, C. M.; Odom, R. W.; Salvati, L.; Annapragada, A.; Fu Lu, M. Y. *Analytical Chemistry* **1995,** 67, (21), 3871-8.

91. Belu, A. M.; Graham, D. J.; Castner, D. G. *Biomaterials* **2003,** 24, (21), 3635-3653.

92. Mahoney, C. M.; Roberson, S. V.; Gillen, G. *Analytical Chemistry* **2004,** 76, (11), 3199-3207.

93. Mahoney, C. M.; Yu, J.; Fahey, A.; Gardella Jr, J. A. *Applied Surface Science* **2006,** 252, (19), 6609-6614.

94. Grenha, A.; Seijo, B.; Serra, C.; Remuñán-López, C. *Biomacromolecules* **2007,** 8, (7), 2072-2079.

95. Ieva, E.; Trapani, A.; Cioffi, N.; Ditaranto, N.; Monopoli, A.; Sabbatini, L. *Analytical and Bioanalytical Chemistry* **2009,** 393, (1), 207-215.

96. Prestidge, C. A.; Barnes, T. J.; Skinner, W. *Journal of Pharmacy and Pharmacology* **2007,** 59, (2), 251-259.

97. Imbesi, P. M.; Gohad, N. V.; Eller, M. J.; Orihuela, B.; Rittschof, D.; Schweikert, E. A.; Mount, A. S.; Wooley, K. L. *ACS Nano* **2012,** 6, (2), 1503-1512.

98. Van Stipdonk, M. J.; Schweikert, E. A.; Park, M. A. *Journal of Mass Spectrometry* **1997,** 32, (11), 1151-1161.

99. Van Stipdonk, M. J.; Justes, D. R.; Force, C. M.; Schweikert, E. A. *Analytical Chemistry* **2000,** 72, (11), 2468-74.

100. Benninghoven, A. *Angewandte Chemie International Edition in English* **1994,** 33, (10), 1023-1043.

101. Peterson, R. E.; Tyler, B. J. *Atmospheric Environment* **2002,** 36, (39–40), 6041-6049.

102. Winograd, N. *Analytical Chemistry* **2005,** 77, (7), 142 A-149 A.

103. Li, Z.; Verkhoturov, S. V.; Schweikert, E. A. *Anal Chem* **2006,** 78, (21), 7410-6.

104. Pinnick, V.; Rajagopalachary, S.; Verkhoturov, S. V.; Kaledin, L.; Schweikert, E. A. *Analytical Chemistry* **2008**.

105. Rol, P. K.; Fluit, J. M.; Kistemaker, J. *Physica* **1960,** 26, (11), 1000-1008.

106. Grønlund, F.; Moore, W. J. *The Journal of Chemical Physics* **1960,** 32, (5), 1540-1545.

107. Appelhans, A. D.; Delmore, J. E. *Analytical Chemistry* **1989,** 61, (10), 1087-1093.

108. Blain, M. G.; Della-Negra, S.; Joret, H.; Le Beyec, Y.; Schweikert, E. A. *Phys Rev Lett* **1989,** 63, (15), 1625-1628.

109. Schweikert, E. A.; van Stipdonk, M. J.; Harris, R. D. *Rapid Communications in Mass Spectrometry* **1996,** 10, (15), 1987-1991.

110. Wong, S. C. C.; Hill, R.; Blenkinsopp, P.; Lockyer, N. P.; Weibel, D. E.; Vickerman, J. C. *Applied Surface Science* **2003,** 203–204, (0), 219-222.

111. Weibel, D.; Wong, S.; Lockyer, N.; Blenkinsopp, P.; Hill, R.; Vickerman, J. C. *Analytical Chemistry* **2003,** 75, (7), 1754-64.

112. Zheng, L.; Wucher, A.; Winograd, N. *J Am Soc Mass Spectrom* **2008,** 19, (1), 96-102.

113. Cheng, J.; Wucher, A.; Winograd, N. *The Journal of Physical Chemistry B* **2006,** 110, (16), 8329-8336.

114. Verkhoturov, S. V.; Rickman, R. D.; Guillemier, C.; Hager, G. J.; Locklear, J. E.; Schweikert, E. A. *Appl Surf Sci* **2006,** 252, (19), 6490-6493.

115. Locklear, J. E.; Guillermier, C.; Verkhoturov, S. V.; Schweikert, E. A. *Appl Surf Sci* **2006,** 252, (19), 6624-6627.

116. Tempez, A.; Schultz, J. A.; Della-Negra, S.; Depauw, J.; Jacquet, D.; Novikov, A.; Lebeyec, Y.; Pautrat, M.; Caroff, M.; Ugarov, M.; Bensaoula, H.; Gonin, M.; Fuhrer, K.; Woods, A. *Rapid Commun Mass Spectrom* **2004,** 18, (4), 371-6.

117. Bitensky, I. S.; Parilis, E. S. *Nuclear Instruments and Methods in Physics Research Section B: Beam Interactions with Materials and Atoms* **1987,** 21, (1–4), 26-36.

118. Pinnick, V. T.; Verkhoturov, S. V.; Kaledin, L.; Bisrat, Y.; Schweikert, E. A. *Anal Chem* **2009,** 81, (18), 7527-7531.

119. Guillermier, C.; Della-Negra, S.; Schweikert, E. A.; Dunlop, A.; Rizza, G. *International Journal of Mass Spectrometry* **2008,** 275, (1–3), 86-90.

120. Fernandez-Lima, F. A.; Post, J.; DeBord, J. D.; Eller, M. J.; Verkhoturov, S. V.; Della-Negra, S.; Woods, A. S.; Schweikert, E. A. *Analytical Chemistry* **2011,** 83, (22), 8448-8453.

121. Fernandez-Lima, F. A.; Eller, M. J.; DeBord, J. D.; Verkhoturov, S. V.; Della-Negra, S.; Schweikert, E. A. *Nuclear Instruments and Methods in Physics Research Section B: Beam Interactions with Materials and Atoms* **2012,** 273, (0), 270-273.

122. Goacher, R. E.; Gardella Jr, J. A. *Applied Surface Science* **2010,** 256, (7), 2044-2051.

123. Knoll, G. F., Radiation Detection and Measurement. 2nd ed. ed.; Wiley: New York, 1989.

124. Park, M. A.; Gibson, K. A.; Quinones, K.; Schweikert, M. A. *Science* **1990,** 248, (4958), 988-990.

125. Della-Negra, S.; Le Beyec, Y. *Analytical Chemistry* **1985,** 57, (11), 2035-2040.

126. Rajagopalachary, S.; Verkhoturov, S. V.; Schweikert, E. A. *Analytical Chemistry* **2009,** 81, (3), 1089-94.

127. Rajagopalachary, S.; Verkhoturov, S. V.; Schweikert, E. A. *Nano Lett* **2008,** 8, (4), 1076-1080.

128. Pinnick, V. T.; Verkhoturov, S. V.; Kaledin, L.; Bisrat, Y.; Schweikert, E. A. *Anal Chem* **2009,** 81, (18), 7527-31.

129. Fernandez-Lima, F. A.; Eller, M. J.; Verkhoturov, S. V.; Della-Negra, S.; Schweikert, E. A. *Journal of Physical Chemistry Letters* **2010,** 1, (24), 3510-3513.

130. Eller, M. J.; Verkhoturov, S. V.; Della-Negra, S.; Schweikert, E. A. *Journal of Physical Chemistry C* **2010,** 114, (40), 17191-17196.

131. Verkhoturov, S. V.; Eller, M. J.; Rickman, R. D.; Della-Negra, S.; Schweikert, E. A. *Journal of Physical Chemistry C* **2010,** 114, (12), 5637-5644.

132. Davies, M. C.; Wilding, I. R.; Short, R. D.; Khan, M. A.; Watts, J. F.; Melia, C. D. *International Journal of Pharmaceutics* **1989,** 57, (3), 183-187.

133. Davies, M. C.; Short, R. D.; Khan, M. A.; Watts, J. F.; Brown, A.; Eccles, A. J.; Humphrey, P.; Vickerman, J. C.; Vert, M. *Surface and Interface Analysis* **1989,** 14, (3), 115-120.

134. Scholes, P. D.; Coombes, A. G. A.; Illum, L.; Davis, S. S.; Watts, J. F.; Ustariz, C.; Vert, M.; Davies, M. C. *Journal of Controlled Release* **1999,** 59, (3), 261-278.

135. Ogaki, R.; Shard, A. G.; Li, S.; Vert, M.; Luk, S.; Alexander, M. R.; Gilmore, I. S.; Davies, M. C. *Surface and Interface Analysis* **2008,** 40, (8), 1168-1175.

136. Quirk, R. A.; Briggs, D.; Davies, M. C.; Tendler, S. J. B.; Shakesheff, K. M. *Surface and Interface Analysis* **2001,** 31, (1), 46-50.

137. Locklear, J. E. Dissertation, Texas A&M University, College Station, 2006.

138. Li, Z. Characterization of surface ad layered films with cluster secondary ion mass spectrometry. Texas A&M University College Station , Texas 2007.

139. Chen, L.-J. Characterization andquantification of biological Surfaces using cluster TOF-SIMS witht the event-by-event bombardment/detection mode. PhD., Texas A&M University, College Station, Texas, 2012.

140. Hager, G. J. Secondary Ion Emission from Single Massive Gold Culster Impacts. PhD, Texas A&M University College Station, 2007.

141. Rickman, R. D. Secondary Ion Emission From "Super-Efficient" Events: Prospects for Surface Mass Spectrometry PhD, Texas A&M University College Station, 2004.

142. Pinnick, V. T. Nano-Domain Analysis Via Massive Cluster Secodary Ion Mss Spectrometry In The Event-By-Event Mode. PhD, Texas A&M University, College Station, 2009.

143. Ladislas Wiza, J. *Nuclear Instruments and Methods* 162, (1–3), 587-601.

144. Cox, B. D.; Park, M. A.; Kaercher, R. G.; Schweikert, E. A. *Anal Chem* **1992,** 64, (8), 843-847.

145. Gooding, J. J.; Ciampi, S. *Chemical Society Reviews* **2011,** 40, (5), 2704-2718.

146. Caruso, F. *Advanced Materials* **2001,** 13, (1), 11-22.

147. Ulman, A. *Chemical Reviews* **1996,** 96, (4), 1533-1554.

148. Sun, L. Y.; O'Reilly, J. Y.; Kong, D. Y.; Su, J. Y.; Boo, W. J.; Sue, H. J.; Clearfield, A. *J. Colloid. Interf. Sci.* **2009,** 333, (2), 503-509.

149. Ortiz-Avila, C. Y.; Clearfield, A. *J Chem Soc Dalton* **1989**, (8), 1617-1623.

150. Ortiz-Avila, C. Y.; Clearfield, A. *Inorganic Chemistry* **1985,** 24, (12), 1773-1778.

151. Casciola, M.; Capitani, D.; Donnadio, A.; Munari, G.; Pica, M. *Inorganic Chemistry* **2010,** 49, (7), 3329-3336.

152. Santiago, M. B.; Velez, M. M.; Borrero, S.; Diaz, A.; Casillas, C. A.; Hofmann, C.; Guadalupe, A. R.; Colon, J. L. *Electroanalysis* **2006,** 18, (6), 559-572.

153. Vaivars, G.; Mokrani, T.; Hendricks, N.; Linkov, V. *J Solid State Electrochem* **2004,** 8, (11), 882-885.

154. Casciola, M.; Bagnasco, G.; Donnadio, A.; Micoli, L.; Pica, M.; Sganappa, M.; Turco, M. *Fuel Cells* **2009,** 9, (4), 394-400.

155. Colon, J. L.; Thakur, D. S.; Yang, C. Y.; Clearfield, A.; Martin, C. R. *Journal of Catalysis* **1990,** 124, (1), 148-159.

156. Mejia, A. F.; Diaz, A.; Pullela, S.; Chang, Y.-W.; Simonetty, M.; Carpenter, C.; Batteas, J. D.; Mannan, M. S.; Clearfield, A.; Cheng, Z. *Soft Matter* **2012,** 8, (40), 10245-10253.

157. Diaz, A.; David, A.; Perez, R.; Gonzalez, M. L.; Baez, A.; Wark, S. E.; Zhang, P.; Clearfield, A.; Colon, J. L. *Biomacromolecules* **2010,** 11, (9), 2465-2470.

158. Saxena, V.; Diaz, A.; Clearfield, A.; Batteas, J. D.; Hussain, M. D. *Nanoscale* **2013,** 5, (6), 2328-2336.

159. Liz-Marzán, L. M.; Giersig, M.; Mulvaney, P. *Langmuir* **1996,** 12, (18), 4329-4335.

160. Ohmori, M.; Matijević, E. *J Colloid Interf Sci* **1993,** 160, (2), 288-292.

161. Alberti, G.; Costantino, U.; Környei, J.; Giovagnotti, M. L. L. *Reactive Polymers, Ion Exchangers, Sorbents* **1985,** 4, (1), 1-10.

162. Alberti, G.; Casciola, M.; Costantino, U.; Levi, G.; Ricciardi, G. *Journal of Inorganic and Nuclear Chemistry* **1978,** 40, (3), 533-537.

163. Kijima, T. *Bulletin of the Chemical Society of Japan* **1982,** 55, (9), 3031-3032.

164. Verkhoturov, S. V.; Eller, M. J.; Rickman, R. D.; Della-Negra, S.; Schweikert, E. A. *The Journal of Physical Chemistry C* **2009,** 114, (12), 5637-5644.

165. Horsley, S. E.; Nowell, D. V.; Stewart, D. T. *Spectrochimica Acta Part A: Molecular Spectroscopy* **1974,** 30, (2), 535-541.

166. Krisanangkura, P.; Packard, A. M.; Burgher, J.; Blum, F. D. *Journal of Polymer Science Part B: Polymer Physics* **2010,** 48, (17), 1911-1918.

167. Chen, L.-J.; Seo, J. H.; Eller, M. J.; Verkhoturov, S. V.; Shah, S. S.; Revzin, A.; Schweikert, E. A. *Analytical Chemistry* **2011,** 83, (18), 7173-7178.

168. Clearfield, A.; Tindwa, R. M. *Journal of Inorganic and Nuclear Chemistry* **1979,** 41, (6), 871-878.

169. Troup, J. M.; Clearfield, A. *Inorg. Chem.* **1977,** 16, (12), 3311-3314.

170. Auerbach, S. M.; Carrado, K. A.; Dutta., P. K., *Handbook of Layered Materials*. Marcel Dekker Inc: Basel, 2004; Vol. 52.

171. D az, A. n.; David, A.; P rez, R.; Gonz lez, M. L.; B ez, A.; Wark, S. E.; Zhang, P.; Clearfield, A.; Col n, . L. *Biomacromolecules* **2010,** 11, (9), 2465-2470.

172. Alberti, G.; Costantino, U. *J Mol Catal* **1984,** 27, (1-2), 235-250.

173. Clearfield, A.; Costantino, U., Layered Metal Phosphates and their Intercalation Chemistry. In *Comprehensive Supramolecular Chemistry*, 1 ed.; Alberti, G.; Bein, T., Eds. Pergamon: New York, 1996; Vol. 7, pp 107-149.

174. Clearfield, A.; Tindwa, R. M. *J Inorg Nucl Chem* **1979,** *41*, (6), 871-878.

175. Ferragina, C.; Di Rocco, R.; Giannoccaro, P.; Patrono, P.; Petrilli, L. *J. Incl. Phenom. Macrocycl. Chem.* **2009,** 63, 1-9.

176. Santiago, M. B.; Velez, M. M.; Borrero, S.; Díaz, A.; Casillas, C.; Hofmann, C.; Guadalupe, A. R.; Colón, J. L. *Electroanalysis* **2005,** *18*, (6), 559-572

177. Santiago, M. E. B.; Declet-Flores, C.; Díaz, A.; Vélez, M. M.; Bosques, M. Z.; Sanakis, Y.; Colón, J. L. *Langmuir* **2007,** 23, (14), 7810-7817.

178. Kaschak, D. M.; Johnson, S. A.; Hooks, D. E.; Kim, H. N.; Ward, M. D.; Mallouk, T. E. *J. Am. Chem. Soc.* **1998,** 120, 10887-10894.

179. Clearfield, A.; Berman, J. R. *J. Inorg. Nucl. Chem.* **1981,** 43, (9), 2141-2142.

180. Sun, L.; Boo, W. J.; Sue, H.-J.; Clearfield, A. *New J Chem* **2007,** 31, 39 - 43.

181. Chusuei, C. C.; Goodman, D. W.; Van Stipdonk, M. J.; Justes, D. R.; Schweikert, E. A. *Anal. Chem.* **1998,** 71, (1), 149-153.

182. Mahoney, C. M.; Yu, J.; Gardella, J. A. *Analytical Chemistry* **2005,** 77, (11), 3570-3578.

183. Fang, J.; Nakamura, H.; Maeda, H. *Adv Drug Deliv Rev* **2011,** 63, (3), 136-51.

184. Maeda, H. *Bioconjugate chemistry* **2010,** 21, (5), 797-802.

185. Ghosh, S.; Sharma, A.; Talukder, G. *Biological trace element research* **1992,** 35, (3), 247-71.

186. Clearfie.A; Duax, W. L.; Medina, A. S.; Smith, G. D.; Thomas, J. R. *J Phys Chem-Us* **1969,** 73, (10), 3424-&.

187. Rudolf, P. R.; Clearfield, A. *Inorganic Chemistry* **1989,** 28, (9), 1706-1710.

188. Clearfield, A.; Ortizavila, C. Y. *Acs Sym Ser* **1992,** 499, 178-193.

189. D az, A.; P rez, R.; David, A.; Gonz lez, M. L.; B ez, A.; Kinninbrugh, T.; Zhang, P.; Clearfield, A.; Col n, . L. *Submitted to Angewandte Chemie-International Edition in English* **2011**.

190. Choy, J.-H.; Kwak, S.-Y.; Jeong, Y.-J.; Park, J.-S. *Angew. Chem. Int. Ed.* **2000,** 39, (22), 4041-4045.

191. Masarudin, M. J.; Yusoff, K.; Rahim, R. A.; Hussein, M. Z. *Nanotechnology* **2009,** 20, (4), 045602.

192. Lee, J.-W.; Gardella, J. A. *Analytical Chemistry* **2003,** 75, (13), 2950-2958.

193. Verkhoturov, S. V.; Eller, M. J.; Della-Negra, S.; Rickman, R. D.; Locklear, J. E.; Schweikert, E. A. *Surface and Interface Analysis* **2011,** 43, (1-2), 49-52.

194. Li, Z.; Verkhoturov, S. V.; Locklear, J. E.; Schweikert, E. A. *International Journal of Mass Spectrometry* **2008,** 269, (1-2), 112-117.

195. Rickman, R. D.; Verkhoturov, S. V.; Hager, G. J.; Schweikert, E. A. *Int J Mass Spectrom* **2005,** 245, (1-3), 48-52.

196. Chen, L. J.; Seo, J. H.; Eller, M. J.; Verkhoturov, S. V.; Shah, S. S.; Revzin, A.; Schweikert, E. A. *Analytical Chemistry* **2011,** 83, (18), 7173-7178.

197. Curini, M.; Rosati, O.; Costantino, U. *Curr. Org. Chem.* **2004,** 8, (7), 591-606.

198. Yang, C. Y.; Clearfield, A. *React Polym* **1987,** 5, (1), 13-21.

199. Rapôso, C. M. d. O.; Eon, J. G. *Materials Research* **2002,** 5, 421-426.

200. Choi, S.-J.; Oh, J.-M.; Choy, J.-H. *J Phys Chem Solids* **2008,** 69, (5–6), 1528-1532.

201. Oh, J.-M.; Choi, S.-J.; Kim, S.-T.; Choy, J.-H. *Bioconjugate chemistry* **2006,** 17, (6), 1411-1417.

202. Choi, S.-J.; Oh, J.-M.; Choy, J.-H. *Journal of Materials Chemistry* **2008,** 18, (6), 615-620.

203. Park, J. H.; Gu, L.; von Maltzahn, G.; Ruoslahti, E.; Bhatia, S. N.; Sailor, M. J. *Nature materials* **2009,** 8, (4), 331-6.

204. Dhar, S.; Daniel, W. L.; Giljohann, D. A.; Mirkin, C. A.; Lippard, S. J. *J Am Chem Soc* **2009,** 131, (41), 14652-3.

205. Yu, T.; Greish, K.; McGill, L. D.; Ray, A.; Ghandehari, H. *ACS Nano* **2012,** 6, (3), 2289-301.

206. Slowing, II; Wu, C. W.; Vivero-Escoto, J. L.; Lin, V. S. *Small* **2009,** 5, (1), 57-62.

207. Choy, J. H.; Jung, J. S.; Oh, J. M.; Park, M.; Jeong, J.; Kang, Y. K.; Han, O. J. *Biomaterials* **2004,** 25, (15), 3059-64.

208. Berry, C. C. *Journal of Materials Chemistry* **2005,** 15, (5), 543-547.

209. Xing, X.; He, X.; Peng, J.; Wang, K.; Tan, W. *J Nanosci Nanotechnol* **2005,** 5, (10), 1688-93.

210. Kokubo, T.; Takadama, H. *Biomaterials* **2006,** 27, (15), 2907-2915.

211. Marques, M. R. C.; Loebenberg, R.; Almukainzi, M. *Dissolution Technologies* **2011,** 18, (3), 15-28.

212. Prokopowicz, M.; Żegliński, .; Gandhi, A.; Sawicki, W.; Tofail, S. A. M. *Colloids and Surfaces B: Biointerfaces* **2012,** 93, (0), 249-259.

213. Dhar, S.; Kolishetti, N.; Lippard, S. J.; Farokhzad, O. C. *Proceedings of the National Academy of Sciences* **2011,** 108, (5), 1850-1855.

214. Brewer, A. K. *Pharmacology, biochemistry, and behavior* **1984,** 21 Suppl 1, 1-5.

215. Sun, Q.; Radosz, M.; Shen, Y. *Journal of controlled release* **2012,** 164, (2), 156-69.

216. Kanpur, I. http://www.iitk.ac.in/infocell/iitk/newhtml/story/Story%20of%20the%20Week-%20Sept2009_%20Ashok%20BSBE_files/image006.jpg (1/17/2014),

217. Commisso, C.; Davidson, S.; Soydaner Azeloglu, R.; Parker, S.; Kamphorst, J.; Hackett, S.; Grabocka, E.; Nofal, M.; Drebin, J.; Thompson, C.; Rabinowitz, J.; Metallo, C.; Vander Heiden, M.; Bar Sagi, D. *Nature* **2013,** 497, (7451), 633-7.

218. Szakal, C.; Narayan, K.; Fu, J.; Lefman, J.; Subramaniam, S. *Analytical Chemistry* **2011,** 83, (4), 1207-1213.